CANCER CELL MIGRATION AND DECISION-MAKING IN PHYSIOLOGICALLY RELEVANT CONFINING MICROENVIRONMENTS

by
Alexandros Afthinos

A dissertation submitted to Johns Hopkins University in conformity with the requirements for the degree of Doctor of Philosophy

Baltimore, Maryland
September 2018

ABSTRACT

In metastasis, cancer cells break away from a primary tumor and travel through the blood or lymph system to distant parts of the body forming new secondary metastatic tumors. Metastatic disease is responsible for ~90% of cancer-related deaths. Cell migration is central to the metastatic cascade and recent technological advances have elucidated the importance of cancer migration through confining open tracks around the cell body. Thus, extensive study and characterization of confined cell migration is critical for the development of future cancer treatments.

Following an introduction to the *in vitro* devices used in confined migration and the mechanisms of cell locomotion that they have revealed, we present a novel tool, a hydrogel encapsulated microchannel array (HEMICA), used for studying cell migration in physiologically relevant microenvironments. HEMICA is made out of accessible, inexpensive materials based on established techniques and emulates a set of physical properties found in native tissue. HEMICA can be used for live-cell imaging, confocal imaging, immunofluorescence, Foster Resonance Energy Transfer (FRET), actin flow measurements, chemotactic gradient studies, apicobasal stiffness anisotropy studies and 3D Traction Force Microscopy. In addition, it can create microenvironments that support collective and single cell-file migration. Subsequently, we use HEMICA to characterize MDA-MB-231 adenocarcinoma cell migration through various confining and non-confining microchannels, and compare confined migration characteristics in stiff versus soft substrates. We observe the impact of substrate stiffness on the morphodynamic changes of cells, and distinguish the role of confinement in accentuating cell polarization and diminishing changes in cell spreading. We demonstrate the dependence of contact

guidance to substrate stiffness and via 3D TFM we showcase that the increase of substrate stiffness leads to higher traction forces in confinement. Furthermore, we affirm that MDA-MB-231 confined migration in soft substrates is dependent on myosin IIA (MIIA), phosphorylated myosin light chain (pMLC), actin, integrins and adhesions, and juxtapose the osmotic engine effects of sodium hydrogen exchanger 1 (NHE1) observed in stiff substrates with its function in more physiologically relevant ones. Finally, we correlate MIIA-based contractility to the polarization of pMLC, NHE1 and actin flow.

We next use microfabrication techniques to create microenvironments of varying hydraulic resistance and analyze the decision-making process of MDA-MB-231 and HT1080 fibrosarcoma cells. We confirm that hydraulic resistance dictates decision-making in confinement, characterize the decision-making process based on the persistent growth of a leading protrusion of a cell at a channel intersection, showcase the effects of actin nucleation on decision-making time, and identify MIIA and transient receptor potential melastatin-7 (TRPM7) as the main mechanosensors of hydraulic resistance in confinement. We then establish the relationship between hydraulic resistance, actin and myosin and build a theoretical framework for confined cell decision-making. Overall our results elucidate the importance of the physical microenvironment in regulating cell migration.

Advisor: Dr. Konstantinos Konstantopoulos

ACKNOWLEDGMENTS

Through the course of my dissertation I met and collaborated with many people who allowed me to mature as a person and a scientist. First, I would like to thank my research advisor, Dr. Konstantinos Konstantopoulos, for his leadership and mentorship. He was the one who believed in my abilities and gave me the opportunity to contribute to his team's efforts in understanding cancer metastasis. I want to thank him for his patience and support through my endeavor of creating a novel tool for studying migration in physiologically relevant microenvironments, and acknowledge his dedication in fostering collegiality and collaboration within the lab. The opportunity to be his teaching assistant in Transport Phenomena I and a mentor to students has been invaluable. I have learned to listen carefully, understand the individual needs, strengths and weaknesses of others, and adapt my guiding techniques in order to benefit them. His trust on me being the lab administrator, and the experience of handling purchases and providing technical assistance, have given me insight into the inner workings of the university, the departments and the laboratories, and have taught me to be organized while also acting ethically and responsibly. I couldn't thank him more for everything he has done for me. Second, I would like to thank my thesis committee, Dr. Stavroula Sofou, Dr. Honggang Cui, Dr. Yun Chen and Dr. Kalina Hristova, for their time and input.

I would like to thank my colleagues in the Konstantopoulos lab, both past and present: Dr. Colin Paul, Dr. Kimberly Stroka, Dr. Daniel Shea, Dr. Luthur Cheung, Dr. Wei-Chien Hung, Dr. Bryan Grabias, Dr. Jack Chen, Dr. Phrabha Raman, Bin Sheng Wong, Emily Wisniewski, Robert Law, Runchen Zhao, Christopher Yankaskas, Soontorn Tuntithavornwat, Kaustav Bera, Yuqi Zhang, Christina Hum, Se Jong Lee and Tian Zhu.

Among my colleagues and collaborators, I would like to specifically thank Dr. Panagiotis Mistriotis who not only had a great impact in my development as a researcher, but also stood by me through the good times and the bad, and became a friend I can trust, a friend for life. In addition, I want to thank my collaborator and friend Dr. Carlos Pardo Pastor for sharing with me long scientific and philosophical coffee walks around campus, and stimulating my creativity and scientific curiosity. I also want to thank Dr. Sean Sun, Dr. Yun Chen and Dr. Yizeng Li for our collaborations and inspiring conversations.

Thank you to the incredibly helpful staff of the Chemical & Biomolecular Engineering Department and Institute of Nanobiotechnology: Ellie Boettinger-Heasley, Kierra Suggs, Carla Dodd, Beth Rannie, Lucy Raybon and Caroline Qualls.

Special thanks to the women of my life, Louise Mariani and Tatiahna Rivera-Rodriguez, who endured my long working nights and weekends, and served as my bright guiding stars.

Last but not least, I want to thank my parents Spyro and Christina. None of this would have been possible without their support, their guidance and their love. They are self-made, they have overcome challenges in life with integrity and moral rectitude, and they have bared with living away from their only son for years. They are my true heroes and I wish one day to be half as strong, empathetic and compassionate as they are.

DEDICATION

To my parents Spyro and Christina

who supported me in my journey of

personal completeness and intellectual curiosity.

TABLE OF CONTENTS

LIST OF FIGURES

Chapter 1

INTRODUCTION

Metastasis is the most common cause of cancer related deaths (Mehlen and Puisieux 2006). The metastatic cascade involves migration of cancer cells away from a primary tumor, intravasation into the blood vessels or the lymphatic system, travel to distant sites in the body, successful attachment and extravasation to secondary tissues, and formation of secondary metastatic foci (Wirtz, Konstantopoulos et al. 2011). This process is highly inefficient since very few cancer cells which access the main circulation give rise to secondary tumors. However, patients with cancer micrometastases do not show long term responses to medical treatments (Qian, Deng et al. 2009). The clinical failure to treat metastatic disease reveals our poor understanding of the mechanisms involved in the metastatic cascade which is governed by the interactions between cancer cells and the microenvironments they encounter (Discher, Janmey et al. 2005).

Scientist have recreated various environments with which cells interact in vitro and have controlled their biochemical composition, stiffness, porosity and dimensionality in order to study their specific effects on cell migration, invasion, differentiation, proliferation and apoptosis (Saha, Keung et al. 2008, Kloxin, Kasko et al. 2009, Murphy and O'Brien 2010, Petrie and Yamada 2012, Wen, Vincent et al. 2014). Moving from 2D to 3D migration studies, revealed molecules and processes which play central roles on cell motility. One such family of molecules are matrix metalloproteases (MMPs). MMPs are produced by cells in 3D in order to degrade the extracellular matrix (ECM) and open migration channels

for metastasis (Turk 2006). Two main categories of MMP inhibitors were synthesized (hydroxamates and non-hydroxamates) (Abbenante and Fairlie 2005) in order to abrogate cancer cell migration, but failed clinical trials due to either adverse side effects or no major clinical benefit. Henceforth, studies which attempted to explain the failure of MMP inhibitors led the way to greater innovation and contributed significantly to our current understanding of cell migration. Cells under MMP inhibition were shown to adapt towards an amoeboid movement which can support non-proteolytic migration (Friedl and Wolf 2003) and intravital microscopy proved the existence of open confining tracks created by various anatomical structures or cells, which are used during cancer cell migration (Alexander, Koehl et al. 2008, Friedl and Alexander 2011, Weigelin, Bakker et al. 2012). Thus the study of migration in confining channels is critical for the development of efficient cancer treatments.

In this dissertation, we review the devices that have attempted to bridge the gap between *in vivo* and *in vitro* experiments, explain the characteristics of confined cell migration, analyze the principle of hydraulic resistance and its effect on confined cell migration, and review the function of ion channels which have been proven to be critical in cell locomotion. In addition, we present a novel hydrogel-based microfluidic device (HEMICA) which overcomes the hurdles faced by other in vitro assays, we use this tool for studying cell migration in microenvironments of physiological stiffness and finally, through our study of confined cell migration decision-making in branched channel intersections, reveal the cytoskeletal and membrane proteins which are affected by hydraulic resistance and analyze their role in decision-making.

We conclude by discussing translational applications of microfluidic assays, including HEMICA, and their benefit to cancer research.

Bioengineering Methods for Migration Studies

Although *in vivo* studies have been crucial in proving the significance of *in vitro* findings regarding cell migration, their cost and complexity renders them cumbersome and inefficient in providing mechanistic insight. Instead, mimicking different properties of the ECM *in vitro* allows for carefully designed controlled experiments, in which the interactions of cells with their microenvironment can be clearly deciphered. As cells migrate through our body, they encounter environments of various dimensions, chemical and biophysical properties. Altering the dimensionality of the ECM led to the production of two dimensional (2D) (Tse and Engler 2011), one dimensional (1D) (Chang, Guo et al. 2013) and three dimensional (3D) (Petrie, Gavara et al. 2012) substrates. The composition of the ECM inspired the creation of scaffolds using chitosan (Hong, Song et al. 2007), alginate-co-gelatin (Yeo, Geng et al. 2007), styrenated gelatin (Hoshikawa, Nakayama et al. 2006), hyaluronic acid (Yeh, Ling et al. 2006), chondroitin sulfate (Li, Williams et al. 2004), PEGylated fibrinogen (Almany and Seliktar 2005), elastin-like polypeptides (McHale, Setton et al. 2005), poly(ethylene glycol) (Rice and Anseth 2007), polyfumarate (Wang, Williams et al. 2005), poly(6-aminohexyl propylene phosphate)-acrylate (Li, Wang et al. 2006) and collagen (Xu, Molnar et al. 2009). Substrate porosity (Murphy and O'Brien 2010), protein fiber thickness (Christopherson, Song et al. 2009) and fiber alignment (Chew, Mi et al. 2008) have been extensively investigated as they affect cell migration. Based on the mode of cell migration *in vivo*, several proteolytically (Webb,

Nguyen et al. 2000) and non-proteolytically cleaved (Pathak and Kumar 2012) scaffolds were created with various ranges of stiffness and functionalized protein concentrations.

PDMS-based Devices for Confined Migration Studies

By using sophisticated microfabrication techniques, precise topographical microenvironments of fixed aspect ratios have been created (Balzer, Tong et al. 2012). The majority of microfabricated devices used for the study of cell migration in confinement, are composed of polydimethylsiloxane (PDMS), which is a stiff, optically transparent material, allowing oxygen diffusion (Duffy, McDonald et al. 1998, Sackmann, Fulton et al. 2014). These devices are produced by micromolding PDMS from a patterned silicon wafer (Heuze, Collin et al. 2011). Microchannels are positioned adjacent to cell seeding areas and allow for real-time imaging of confined cell migration (Irimia, Charras et al. 2007). The microchannels can be coated with various ECM proteins (Irimia and Toner 2009) and support studies with chemical (Breckenridge, Egelhoff et al. 2010), osmotic (Stroka, Jiang et al. 2014) and voltage gradients (Huang, Samorajski et al. 2013).

By varying the channel dimensions, Irimia and colleagues showed that MDA-MB-231 cell speed varies biphasically with cross-sectional area (Irimia and Toner 2009). The use of an FBS chemotactic gradient in a PDMS-based microfluidic device with channels of width 3, 6, 10, 20 and 50 μm, and height 10 μm indicated that HOS cell speed was dependent on width, with higher migration speeds at larger widths and greater cell entrance to the microchannels with a steeper gradient (Tong, Balzer et al. 2012). Comparison between tumorigenic metastatic and non-metastatic cells showed an increased likelihood that tumorigenic metastatic cells would enter and exit the microchannels. A series of

osmotic shocks in conjunction with pharmacological actin depolymerization, revealed a new mechanism of confined cell migration which is based on water flux (Stroka, Jiang et al. 2014). NIH 3T3 fibroblasts, with the application of an electric field across a microchannel array, showed a change in their preferential alignment as compared to the electric field lines. While in unconfined environments they aligned perpendicularly to the field and migrated toward the cathode, in confinement they oriented parallel to the field and migrated along the microchannels (Huang, Samorajski et al. 2013). This suggested that the topographical cue presented by the microchannels is stronger than the electric field one in terms of cell alignment.

Hydrogel-based Devices for Confined Migration Studies

Hydrogels have been widely used in cell migration studies since their intrinsic properties mimic native tissues. They are composed of a matrix of macromolecules with a high water content and they can reach a wide range of stiffnesses. In addition, their water retention offers a suitable drug diffusion pathway and they are biocompatible (Ganji, Vasheghani-Farahani et al. 2010).

Recent advances in two-photon laser scanning (TPLS) photolithography, have allowed the fabrication of 3D micropatterns of biomolecules in PEG hydrogels (Hahn, Miller et al. 2006). The technique takes advantages of the simultaneous absorption of focused photons to achieve two-photon excitation in microscale focal volumes (Denk, Strickler et al. 1990). As such, encapsulated fibroblasts were able to proteolytically degrade

the poly(ethylene glycol) diacrylate (PEGDA) hydrogel and follow the path of the micropatterned Arg-Gly-Asp-Ser-Lys (RGDSK) adhesive ligand (Lee, Moon et al. 2008).

However, tuning and controlling the properties of PEG hydrogels via the photoinitated chain polymerization of (meth)acrylated PEG precursors results in gel heterogeneities and nonidealities which influence the material properties and affect cell morphology (Bryant, Anseth et al. 2004). Several reports have presented a novel way of gel cross-linking via the copper(I)-catalyzed [3+2] cycloaddition reaction (Click chemistry) between the azides and terminal acetyle moieties (Malkoch, Vestberg et al. 2006, Ossipov and Hilborn 2006, Crescenzi, Cornelio et al. 2007). PEG hydrogels formed via this Click chemistry resulted in highly cross-linked gels with ideal structures and dramatically improved mechanical properties. Hydrogels based on Click chemistry have been patterned with RGDSC thus forming a biochemical gradient with the potential of guiding cell migration (Polizzotti, Fairbanks et al. 2008).

Evidence by Kloxin and colleages has shown that the physical properties of hydrogels can be tuned temporally and spacially with light (Kloxin, Kasko et al. 2009). They utilized the photodegradable functionality of a nitrobenzyl ether-derived moiety which was attached to PEG-bis-amine and thus synthesized photodegradable PEG-based hydrogels. Subsequently, they encapsulated fibroblasts, used a single (405 nm) or two-photon (740) LSM to degrade a portion of the gel and observed migration into the photodegraded channel. Overall, hydrogels have paved the way for a deeper understanding of the way materials influence live cell functions.

Mechanisms of Confined Migration

Mounting evidence suggests that confined micro-channels do not only offer "paths of least resistance" for tumor cell migration (Provenzano, Eliceiri et al. 2006), but rather impose a mechanical load on the cells, that initiates an intracellular cascade of signaling events (Hung, Chen et al. 2013) which alters the migration mechanisms (Hung, Chen et al. 2013, Hung, Yang et al. 2016) and induces differential gene expression (Le Berre, Aubertin et al. 2012). Thus, during in vivo migration cancer cells may alter their phenotype to accommodate for changes in the architecture of the local microenvironment.

Although our understanding on cell motility in confinement is still in its early stages, recent studies suggest that locomotion through confined microenvironment represents a unique type of migration that is mechanistically distinct from typical unconfined 2D migration. While 2D migration requires fan-like protrusions (lamellipodial) to move the plasma membrane forward (Pollard and Borisy 2003, Provenzano, Eliceiri et al. 2006, Friedl and Alexander 2011), confined migration relies on the interplay of cell adhesion and actomyosin contractility. Under conditions of confinement and low adhesion, cells preferentially use an amoeboid type of migration (Liu, Le Berre et al. 2015) with a rounded cell morphology, membrane blebs, diffuse distribution of cell adhesion proteins, and a dependence on actomyosin contractility. On the other hand, under conditions of confinement and high adhesion, cells use either a lobopodial-based migration with high contractility in a linear elastic matrix, non-polarized cortactin, PIP_3, Rac1 and Cdc42 or pseudopodial based migration with polarized PIP_3, Rac1 and Cdc42 at the leading edge (Petrie, Gavara et al. 2012, Petrie, Koo et al. 2014). Notably, activation of the contractile machinery is also sufficient to induce amoeboid based migration even in the presence of

cell adhesion (Sahai and Marshall 2003, Wolf, Mazo et al. 2003). Interestingly, the Konstantopoulos lab has recently discovered a novel mechanism of confined migration that relies on water permeation coupled with dispensable actomyosin contractility (Stroka, Jiang et al. 2014). Thus, cell intrinsic properties in conjunction with the heterogeneity of the tissue microenvironment enable tumor cells to adopt a wide repertoire of migration modes in confinement.

Confinement-Induced Cell Signaling and Gene Expression

Currently it is unclear how cells sense and adapt to the confined microenvironment. Preliminary studies suggest that cells sense confinement via stretch activated channels and/or components of the cytoskeleton and nuclear matrix. The Konstantopoulos lab demonstrated that confinement sensing is mediated by an elevation of intracellular calcium levels via the stretch-activated cation channel Piezo. Increase in calcium leads to a phosphodiesterase 1 (PDE1)-dependent suppression of protein kinase A (PKA) activity which acts in conjunction with myosin II to regulate cell migration (Hung, Yang et al. 2016). Along these lines, the nucleus can also serve as a mechanosensor in confinement. Nuclear compression results into nuclear rupture, DNA damage, and release of proinflammatory eicosanoids (Denais, Gilbert et al. 2016, Enyedi, Jelcic et al. 2016, Raab 2016). Interestingly, vertical confinement also leads to differential expression of genes involved in inflammation, DNA damage, stress response, and membrane synthesis (Le Berre, Aubertin et al. 2012).

Hydraulic Resistance in Confined Migration

The Reynolds number (Re) indicates the relative importance of inertial to viscous forces (Re = ρ x V x L / μ, where ρ (kg m^{-3}) is the density of the liquid, L (m) is a characteristic length of the system, such as the height of the channels, μ (kg $m^{-1}\ s^{-1}$) is the viscosity of the liquid and V (m s^{-1}) is the linear velocity of the liquid through the channel). Liquid flow through microfluidic channels usually occurs at low Re. When an object such as a bubble or a cell with an assumed water impermeable membrane attempts to move through a microchannel, it has to push the entire column of liquid which lies ahead. As such it has to overcome the fluidic resistance R (kg $m^{-4}\ s^{-1}$) that the liquid imposes on the object. Q ($m^3\ s^{-1}$) is the volumetric flow rate of the liquid between two points in a channel and ΔP (kg $m^{-1}\ s^{-2}$) is the pressure difference between these two points. The volumetric flow rate and the pressure difference are proportional and the constant of proportionality is the fluidic resistance. As such:

$$\Delta P = Q\ R$$

The laminar flow of a single liquid phase through a rectangular channel where L (m) is the length of the channel, W (m) the width, H (m) the height and α a dimensionless parameter that depends on aspect ratio (W / H), is described by:

$$\Delta P = \frac{\alpha\ \mu\ Q\ L}{W\ H^3}$$

$$\alpha\ = 12\ \left[1 - \frac{192H}{\pi^5 W}\tanh\left(\frac{\pi W}{2H}\right)\right]^{-1}$$

The pressure difference relation is proven accurate to within 0.26% for rectangular channels with $W / H < 1$ independently of the presence or absence of surfactants (within a tested range) (Fuerstman, Lai et al. 2007).

As cells move through microchannel cavities in the body, which are filled with blood, interstitial or cerebrospinal fluid, compensating for the fluidic/hydraulic resistance imposed by these liquids becomes critical. When cells are subjected to decisional choices within the intersections of confining microchannels, the hydraulic pressure has to be physically balanced and then overcome for migration to persist (Sims, Karp et al. 1992, Lammermann and Sixt 2009). The lipid bilayer is slightly permeable to water and cells contain aquaporins that increase their water permeability based on osmosis (Agre and Kozono 2003, Verkman 2005). In addition, cells can intake water through pinocytosis (Danielsen and Hansen 2016). Although these mechanisms will decrease the value of the apparent hydraulic resistance that cells encounter, it has been shown that neutrophil-like HL-60 cells respond to channel intersections of asymmetric hydraulic resistances by choosing the path of lowest resistance (Harrison V. Prentice-Motta 2013). In addition, MDA-MB-231 cells that make decisions in intersections of cell-scaled versus subnucleus-scaled channels have a higher probability in entering the cell-scaled ones (Mak and Erickson 2014). Since the length of the channels in the study by Mak and colleagues were similar, the decreased cross-sectional area of the subnucleus-scaled path indicated that cells choosing that path would have to overcome a greater local resistance.

Ions and Ion Channels in Cell Migration

The metastatic cascade is defined by the ability of tumor cells to migrate. Without the ability of tumor cells to move, there would be no metastatic disease. Carcinoma cells that have lost their epithelial polarization during epithelial to mesenchymal transition (EMT), move away from the epithelial layer (Thiery and Sleeman 2006) while carbonic anhydrase (CAIX), pH regulating transport proteins such as NHE1, AE2, MCTs and aquaporins relocate to the cell front (Svastova, Witarski et al. 2012).

For cell migration to occur, actin polymerization is initiated at the cell leading edge while depolymerization at the rear of lamellipodia. Several proteins are involved in binding to the actin monomers, severing actin filaments and branching existing ones or nucleating the formation of new ones. Actin filaments bind to myosin and thus generate forces which are transmitted via focal adhesions to the ECM (Le Clainche and Carlier 2008). Both cytoskeletal and adhesion dynamics are regulated by ionic mechanisms and as a result they depend on ion channel proteins. Not only do ion channels regulate ion homeostasis, but they are also pH or Ca^{2+} sensitive themselves. In addition, Ca^{2+} and H^{+} concentrations are coupled and thus cannot change independently (Swietach, Youm et al. 2013).

Cofilin is a protein that creates new sites of actin filament assembly by severing actin filaments and producing free barbed ends. By its function, it facilitates actin polymerization and membrane protrusion at the cell front or the tip of invasive structures and promotes cell migration and invasion (Wang, Eddy et al. 2007). Cofilin, however, needs to be activated by the local intracellular alkalization in the lamellipodium which is regulated by the sodium hydrogen exchanger NHE1 (Lagana, Vadnais et al. 2000, Stock, Mueller et al. 2007). Gelsolin is another actin-binding protein which is involved in actin

assembly/disassembly yet it is activated by local acidification (Lagarrigue, Ternent et al. 2003). As such, local intracellular acidification or alkalization, which is regulated by NHE1, is responsible for fundamental cytoskeletal changes required for cancer migration (Srivastava, Barreiro et al. 2008). Taking into consideration the upregulation of NHE1 in multiple tumors (Reshkin, Bellizzi et al. 2000, Chiang, Chou et al. 2008), its function is unequivocally critical.

Intracellular calcium concentration has a great impact on cytoskeletal dynamics, since Ca^{2+} interacts with numerous proteins which are involved in cell contraction and adhesion. Myosin II (Betapudi, Rai et al. 2010), myosin light chain kinase (Tsai and Meyer 2012), calpain (Campbell and Davies 2012), calcium/calmodulin-dependent protein kinase II (Cuddapah and Sontheimer 2010) and focal adhesion kinase (Giannone, Ronde et al. 2002) are influenced by Ca^{2+}. Apart from the front-rear Ca^{2+} gradient that is established in cells (Hahn, Debiasio et al. 1992), there are local transient Ca^{2+} signals which promote focal adhesion disassembly or regulate the direction of migration (Giannone, Ronde et al. 2004, Wei, Wang et al. 2009, Tsai and Meyer 2012).

Calcium sensitive α-actinin inhibits actin bundling at the lamellipodia when calcium levels increase. As myosin II is calcium activated, Ca^{2+} regulates the contractile force that causes retraction of the rear of migrating cells (Eddy, Pierini et al. 2000). Ablation of TRPC6 channels, which control Ca^{2+} influx, impairs chemotaxis of murine neutrophils. TRPM7 mediated Ca^{2+} flickers at the front of a cell direct the migration of fibroblasts towards platelet-derived growth factor (PDGF). The function of the TRPC1 channel, which regulates calcium influx, and the $K_{Ca}3.1$ channel, which is activated by Ca^{2+} and regulates K^{+} influx, is critical for tumor cell chemotaxis (Sciaccaluga, Fioretti

et al. 2010, Bomben, Turner et al. 2011, Fabian, Fortmann et al. 2011, Cuddapah, Turner et al. 2013).

Cell migration is a process that involves repetitive extension of the front and retraction of the rear. Stretching of the cell membrane causes mechanosensitive or stretch activated ion channels, such as the ones that belong to the TRPC, TRPV and TRPM families, to open leading to an elevated intracellular Ca^{2+} concentration which either happens simultaneously or follows the retraction of the rear (Lee, Ishihara et al. 1999, Espinosa-Tanguma, O'Neil et al. 2011). This process also requires extensive volume regulation. By activating K^+ and Cl^- channels, cells release KCl and water, and thus decrease their volume (regulatory volume decrease, RVD), and by activating Na^+ K^+2Cl^-cotransport, Na^+/H^+ exchange, and non-selective cation channels cells uptake KCl and water and increase their volume (regulatory volume increase, RVI) (Schwab, Fabian et al. 2012). Many ion channels and transporters which regulate cell volume changes are also part of the cellular migration machinery. Notable examples are $K_{Ca}3.1$ (Cruse, Duffy et al. 2006), $K_v1.3$ (Matheu, Beeton et al. 2008), TRP channels (Waning, Vriens et al. 2007, Wei, Wang et al. 2009), NHE1 (Hayashi, Aharonovitz et al. 2008, Stroka, Jiang et al. 2014), NKCC1 (Haas and Sontheimer 2010) and aquaporins (Papadopoulos, Saadoun et al. 2008).

Chapter 2

HEMICA: HYDROGEL ENCAPSULATED MICROCHANNEL ARRAY IN CANCER METASTASIS

2.1 Introduction

The stiffness of the extracellular matrix (ECM) and the interaction between cells and the microarchitecture of their local microenvironment are critical for many processes including proliferation, migration, and differentiation. As the human body consists of a plethora of microenvironments, cells adapt and respond to each environment differently. Glioblastoma multiforme (GBM) cells (Ulrich, de Juan Pardo et al. 2009) and lung fibroblasts (Mih, Marinkovic et al. 2012) increase their proliferation with increase in ECM stiffness, while adult neural stem-cells show an optimum in proliferation on stiffnesses that resemble native brain tissue (Saha, Keung et al. 2008). Prostate carcinoma cells show a biphasic dependence between speed and Matrigel stiffness (Zaman, Trapani et al. 2006), aggressive breast cancer cells migrate with varying protrusion and cell body translation dynamics based on the concentration and the thickness of collagen gels (Carey, Kraning-Rush et al. 2012), and polymorphonuclear leukocytes migrate more efficiently through larger pore sizes within ECM gels (Kuntz and Saltzman 1997). Finally, substrate stiffness regulates the osteogenic or adipogenic differentiation of human adipose-derived stromal cells and marrow-derived mesenchymal stromal cells irrespective of hydrogel porosity, protein linker density or protein tethering (Wen, Vincent et al. 2014).

Over the years researchers have been trying to replicate different properties of the ECM in order to perform highly controlled experiments in-vitro. The dimensionality of the ECM resulted in the production of 2D (Tse and Engler 2011), 1D (Chang, Guo et al. 2013) and 3D (Petrie, Gavara et al. 2012) substrates, and the intrinsic properties of the ECM inspired models using various proteins (Seliktar 2012), substrate porosities (Murphy and O'Brien 2010), protein fiber thicknesses (Christopherson, Song et al. 2009) and alignments (Chew, Mi et al. 2008). The behavior of cells in-vivo, inspired the creation of substrates that are proteolytically cleaved (e.g. collagen, Matrigel) (Gaggioli, Hooper et al. 2007) and others that aren't (e.g Polyacrylamide) (Pathak and Kumar 2012), with various ranges of stiffness and protein concentrations. The importance of in-vitro systems that mimic the ECM is unequivocal since they have allowed us to decouple parameters of the ECM and study their effects on cells, leading to novel pharmacological targets and the increase of our understanding of complex cell behaviors.

An important mechanism of cell migration involves the cleavage and reorganization of protein fibers in the ECM (proteolytic migration). As cells migrate through interstitial tissues, they either break down their surrounding matrix (Friedl and Wolf 2009) or follow pre-established open paths (Alexander, Koehl et al. 2008). These paths/microchannels are either created by other migratory cells or they inherently exist in the perivascular, perineural, perilymphatic, perimuscular, fat tissue, bone cavity and brain milieus (Friedl and Alexander 2011). As such, cells don't have to do much remodeling of the ECM and the microchannels maintain the same dimensions before and after cell migration (Weigelin, Bakker et al. 2012). Based on the size of the cells and the dimensions

of these microchannels, migratory cells can be fully or partially confined by these microenvironments.

There are two major systems that attempt to emulate these microtopographies in-vitro. The first one uses soft lithography techniques to create a negative microchannel mold on which Polydimethylsioxane (PDMS) is cured (Tong, Balzer et al. 2012). After curing, PDMS is lifted off the mold and the microchannel design remains imprinted on its lower surface. Subsequently, the PDMS is bonded to a glass surface with or without a layer of PDMS and coated with the desired ECM protein. This system, allows for flexibility in the microchannel design; the heights, lengths and widths of the microchannels can be accurately designed, and the materials and equipment used are fairly inexpensive. On top of that, live-microscopy experiments can be performed, immunostaining is feasible (though cumbersome depending on the microchannel design) and chemotactic or osmotic gradients are easy to establish. Furthermore, this system allows for micropillar printing which enables the study of traction forces (Raman, Paul et al. 2013). The major disadvantage of this tool is that PDMS mixed with its curing reagent at a ratio which is easy to work with is not physiologically relevant. Larger PDMS/curing reagent ratios can produce more compliant substrates but channel imprinting and the maintenance of channel dimensions upon bonding of the upper PDMS layer to the bottom glass/PDMS becomes a challenge. In addition, PDMS is not permeable to water or small molecules and thus does not accurately represent living tissues. Finally, cell adhesion and spreading is possible on PDMS without covalently attaching or tethering ligands, due to the increased hydrophobicity and the fouling properties of its surface, which complicates the dependence of cell mechanics to the ECM protein involved.

The second model for confined migration involves photodegradable poly(ethylene glycol)-based (PEG) hydrogels (Kloxin, Kasko et al. 2009). Synthesis of an o-nitrobenzylether-based photodegradable monomer coupled to primary amines generates a photodegradable cross-linker and synthesis of fibronectin-derived peptide RGDS creates photodegradable tethers. As a result, through photodegradation, the stiffness and the presentation of ligands to cells within a 3D or 2D PEG-based hydrogel can be manipulated in-situ creating dynamic environments. Furthermore, microchannels and patterns of various sizes can be introduced in the hydrogel by fully degrading it. This model is advantageous since we can observe dynamic processes in real time. Stiffness and tethering gradients along the cell axis can be generated and immunostaining is possible even if it requires the production of cryosections of the 3D matrix. In addition, it allows for the generation of round microchannels which are more physiologically relevant. However, this model allows for relatively low cell throughput, requires expensive two photon irradiations sources for precise z-direction degradation of the gel and cannot accommodate stiffnesses larger than ~40kPa. The aspect ratio of the features is limited and the photolabile monomer concentration as well as the intensity, wavelength and time of irradiation have to be optimized per experiment. Moreover, the light sensitivity of different cell lines and the possible use of low-wavelength UV light for irradiation require the assessment of cell viability and function.

While these models allow for the generation of microchannels of various dimensions in 3D, they have attributes which are either non-physiologically relevant or too complicated and costly. The creation of a simple, low cost, high throughput and physiologically relevant system that allows for a multitude of uses and post-migration

studies was imperative, and for this reason we created HEMICA, the Hydrogel Encapsulated Micro-Channel Array. We used soft lithography techniques to create a mold of microchannels of prescribed dimensions and features of high aspect ratios, and we imprinted those channels in a polyacrylamide (PA) hydrogel of physiologically relevant stiffness. Subsequently, we created a flat PA gel with the same or different stiffness than the gel with the imprinted design and bonded the two gels together. The existence of primary amines on both gels allowed us to use commercially available NHS-esters as ligands, which helped adhere the top and the bottom gels to each other and also expand this method of gel-to-gel adherence to other ECM-based protein gels. As a result, the microchannel array got encapsulated within the gel surfaces and by using Sulfo-SANPH and following established protocols we coated the microchannels with the desired ECM protein for cell adhesion.

With this system, we are able to generate features of various widths and heights (minimum W x H: 3 x 3 μm) with no apparent limit on the length. We also created physiological stiffness isotropic and apicobasally anisotropic channels as well as chemotactic gradients. Using HEMICAs, we studied 2D, partially confined and fully confined migration within the same system as well as collective and single cell file migration all with high throughput. We embedded nano-beads on the gels and performed traction force microscopy in 3D as well as immunostaining, Forster Resonance Energy Transfer (FRET) and actin flow measurements with ease.

Through our experiments with different physiological stiffness HEMICAs and breast cancer MDA-MB-231 cells, we observe a biphasic relationship between stiffness and migration speed in various levels of confinement, and a biphasic relation between

speed and confinement in various stiffnesses. We observe the impact of stiffness on the morphodynamic changes of cells and distinguish the role of confinement in accentuating cell aspect ratio and diminishing changes in cell spreading. In addition, we demonstrate the dependence of contact guidance to substrate stiffness in which low stiffness regimes decrease cell guidance. We showcase the impact of chemotactic gradients in confined cell migration and highlight the importance of the apicolateral walls of a microchannel in anisotropic HEMICAs. We use squamous cell carcinoma A431 cells, generate channels where cells migrate collectively and demonstrate how the decrease in channel dimensions leads to single cell-files. Furthermore, we use 3D Traction Force Microscopy (TFM) and show that the increase of stiffness leads to higher traction forces in confinement. We then contrast our findings from MDA-MB-231 migration in physiological stiffness confinement to the pre-existing knowledge in the field, which is established primarily through PDMS-based devices. Our experiments affirm that breast cancer cell migration in HEMICA is based on MIIA, pMLC, actin, integrins and adhesions, while previously proven functions of ion channels such as Sodium-Hydrogen Exchanger NHE1 may be altered. Finally, we show how MIIA contractility correlates with pMLC, NHE1 and actin flow polarization. As such, key parameters of confined migration regain central roles in substrates of physiological stiffness and the balance between cytoskeletal and membranous elements becomes essential.

2.2 Materials and Methods

2.2.1 HEMICA fabrication and usage. An array of parallel feature (channels) with a fixed channel length and height (L = 200 μm, H = 10 μm) and widths of either 3, 6, 10, 15, 20

μm (multichannel design) or only 3 μm (confined migration design) were fabricated via soft lithography as previously described (Balzer, Tong et al. 2012, Hung, Chen et al. 2013, Paul, Shea et al. 2016). To general channels for cell seeding and cell entry a secondary layer of features with height 30 μm and width 400 μm was overlaid. In order to facilitate the generation of inlets and outlets via biopsy punching the HEMICA gels, we overlaid a tertiary layer containing inlet and outlet circular features (H = 100 μm) connected to channels leading towards the secondary layer. The dimension of the features were verified via a profilometer. After the wafers were fabricated, they were cut using a diamond cutter and used as molds for the polyacrylamide gels. Acrylamide (A) (Bio-Rad, 40%) with N,N-Methylene bisacrylamide (B) (Bio-Rad, 2%) were mixed with distilled water to final concentrations of 8% A/0.1% B, 8% A/0.2% B and 8% A/0.6% B corresponding to PA gels of elastic moduli 12, 26 and 46 kPa respectively. For traction force microscopy experiments, a small volume of the distilled water component was replaced with 0.2 μm fluorescent beads (FluoSpheres, Invitrogen) resulting in 0.1% solids in the acrylamide mix. The solutions were then degassed for 25 minutes. 10% ammonium persulfate (Bio-Rad) and 0.4% TEMED (Bio-Rad) were used as initiators of polymerization. Glass coverslips (Fisher Scientific, 22X40 mm) were activated with glutaraldehyde as previously described (Dembo and Wang 1999). 60 μL-100 μL of the final polyacrylamide solutions were placed on top of the coverslip and flattened with an additional non-activated coverslip. 1mL of the mix was placed on top of the lithography produced wafers containing the microchannel designs and covered with another non-activated coverslip. The solutions were allowed to polymerize for 50 minutes and were peeled off of the surfaces, thus generating one flat gel attached to the activated coverslip (flat-gel) and one gel with the microchannel design

imprinted on its lower surface (design-gel). The gels were allowed to swell between 1 and 3 days (depending on the stiffness) in PBS -/- at 37 °C. Inlet and outlet holes were punched, the gels were lightly air-blown and finally sandwiched using 15 μL of 50 mg/mL bis(sulfosuccinimidyl)suberate (BS3, ThermoFisher Scientific) as an adhesive. For Traction Force Macroscopy (TFM) experiments 150 mg/ml BS3 was used. Binding between the two gels lasted for 1 hour. The assembled HEMICA was lightly glued (glass side down) on 60 mm petri dishes to prevent sliding. For confocal experiments custom-made 60 mm petri dishes with an opening in the center were created and HEMICAs were glued on them in order to present an exposed glass center surface for the laser. Subsequently HEMICA was submerged in PBS -/- for 10 minutes in order to rehydrate. After removal of the PBS, the microchannels surfaces were treated with 0.5 mg/mL sulfosuccinimidyl 6-(4'-azido-2'-nitrophenylamino)hexanoate (Sulfo-SANPAH, Thermo Fisher Scientific) as described by (Dembo et al., 1999). HEMICA was then submerged in 20 μg/mL collagen type I (Collagen I Rat Protein, Tail, Thermo Fisher Scientific) overnight at 37 °C for functionalization. The next day the channels were washed with PBS -/- right before cell seeding. For the chemotactic gradient experiments, HEMICAs were submerged in DMEM 1X (Gibco), 1% penicillin/streptomycin (P/S) (10,000 U/mL, Gibco) for 2 hours before cell seeding. After cell seeding, the top wells were filed with DMEM 1X, 10% heat inactivated fetal bovine serum (FBS) (Gibco) and 1% P/S, while the bottom ones with DEMEM 1X, 1% P/S. For the fluorescein isothiocyanate-dextran (FITC-Dextran) experiments, the top wells were filled with 1 mg/mL FITC-Dextran (Millipore Sigma) dissolved in PBS while the bottom wells contained only PBS.

2.2.2 PDMS device fabrication. An array of parallel features (channels) with a fixed channel length, height and width (L = 200 μm, H = 10 μm, W = 3 μm) was fabricated via soft lithography similarly to the fabrication of the HEMICA wafer. To generate channels for cell seeding and cell entry as well as inlet/outlet features, a secondary layer with height 50 μm and width 400 μm was overlaid. The dimensions of the features were verified via a profilometer. The wafers were used as molds for the generation of the PDMS devices as previously described (Balzer, Tong et al. 2012).

2.2.3 Cell culture. Human MDA-MB-231 adenocarcinoma cells (NCI-PBCF-HTB26, PS-ON Bioresource Core Facility at ATCC) and A-431 epidermoid carcinoma cells (CRL-1555, ATCC) were cultured in Dulbecco's Modified Eagle Medium (DMEM) containing 4.5 g/L glucose, L-glutamine and sodium pyruvate (Gibco), supplemented with 10% heat inactivated fetal bovine serum (Gibco) and 1% penicillin/Streptomycin (10,000 U/mL, Gibco). Cells were grown in an incubator at 37 °C and 5% CO_2, passaged every 2-4 days for a maximum of 20 passages.

2.2.4 Pharmacological inhibitors. For the experiments involving pharmacological inhibition, cells were treated with the following agents and their corresponding vehicle controls: blebbistatin (5 or 50 μM) (Sigma Aldrich), latrunculin A (2 μM) (Sigma Aldrich). For experiments involving latrunculin A, cells were allowed to enter the confining micro-channels before pharmacological inhibition was applied. Combined drug inhibition experiments were performed by using blebbistatin first (in order to reduce contractility and

emulate the effects of soft substrates) and after cell entry into the micro-channels the combination of blebbistatin and latrunculin A was used.

2.2.5 Cloning, lentivirus production, transduction. Target sequences were subcloned in pLVTHM (gift from Didier Trono, Addgene, Cambridge, MA, plasmid #12247) using restriction enzymes MluI and ClaI or in pLKO.1 (gift from Bob Weinberg, Addgene, Cambridge, MA, plasmid #8453) using restriction enzymes AgeI and EcoRI. The following target sequences were used:

Scramble Control sh1 (GCACTACCAGAGCTAACTCAGATAGTACT)

Human MYH9 (ACGGAGATGGAGGACCTTATG)

Human MYH10 (GGATCGCTACTATTCAGGA)

Human integrin β1 (TGCCTACTTCTGCACGATGT)

Human NHE1 sh2 (GACAAGCTCAACCGGTTTAAT)

Human NHE1 sh7 (CCAATCTTAGTTTCTAACCAA)

Human AQP5 sh1 (CCATCATCAAAGGCACGTATG)

Human AQP5 sh3 (ACGCGCTCAACAACAACACAA)

The lentiviral shRNA targeting human integrin β1 was generously given by the Wirtz Lab (Johns Hopkins University) (He, Chen et al. 2016). pLenti.PGK.LifeAct-GFP.W was a gift from Rusty Lansford (Addgene plasmid # 51010), pTriExRhoA2G was a gift from Olivier Pertz (Addgene plasmid # 40176), psPAX2 was a gift from Didier Trono (Addgene plasmid # 12260), pMD2.G was a gift from Didier Trono (Addgene plasmid # 12259).

For lentivirus production, 293T/17 cells were co-transfected with psPAX2, pMD2.G and the lentiviral plasmid. Lentivirus was harvested 48 h post transfection and was centrifuged at 50,000 g for 2 h, 4 °C. Cells were transduced with media containing the lentiviral particles for 24 h.

For transient transfections, 60-80% confluent MDA-MB-231 cells were transfected using Lipofectamine 3000 (Thermo Fisher Scientific) based on manufacturer's recommendations.

2.2.6 Cell seeding. Cells were detached from culture dishes using 0.05% trypsin-EDTA (Gibco), centrifuged at 300 g for 5 min and resuspended in DMEM 1X, 10% heat inactivated FBS, 1% penicillin/streptomycin to a concentration of 5 x 10^6 cells/mL. For the chemotactic gradient experiments cells were resuspended in DMEM 1X, 1% P/S. Of the cell suspension 10 – 20 μL were added to the inlet of the devices thus generating a pressure driven flow. In PDMS devices, once the flow was equilibrated, cells were allowed to adhere and spread outside of the micro-channel entrances at 37 °C and 5% CO_2 for at least 30 minutes. Subsequently the inlet/outlet wells were filled with 100 μL media. In HEMICA devices, the flow was equilibrated and cells were allowed to adhere and spread at 37 °C and 5% CO_2 for 30 minutes after submersion of the device to 10 mL of media.

2.2.7 Live cell imaging. Cells were imaged every 20 minutes for 5-18 h on an inverted Nikon Eclipse Ti microscope (Nikon, Tokyo, Japan) with automated controls (NIS-Elements, Nikon) and a 10x/0.45 numerical Ph1 objective using time-lapse microscopy. A stage top incubator (Okolab, Pozzuoli, Italy, or Takai Hit, Shizuoka-hen, Japan) maintained

the right temperature and CO_2. For epifluorescence imaging, DAPI, FITC, TRITC or mCherry filters were used with a 40x air Ph2 objective.

2.2.8 Cell migration tracking and analysis. Live cell videos were analyzed via ImageJ (National Institute of Health, Bethesda, Maryland). The MTrackJ plugin (Meijering, Dzyubachyk et al. 2012) was used for cell path tracking. The cell tracks were recorded from the time of complete entry into the microchannel until contact with the exit was made. Cell speed, persistence and velocity was calculated based on a custom-made MATLAB script (MathWorks, Natick MA).

2.2.9 Immunofluorescence. Cells were fixed with 4% paraformaldehyde (Affymetrix, Inc.), permeabilized in 0.1% Triton X-100 (Sigma) and blocked in 5% bovine serum albumin and 5% goat serum. The following primary antibodies were used overnight at 4 °C to stain cells: anti-pMLC (1:50, phospho-myosin light chain 2 (Ser 19), Cell Signaling), anti-NHE1 (1:50, NHE-1 (B-12), Santa Cruz Biotechnology, Inc.). Alexa Fluor 488 phalloidin (1:100, Invitrogen) was used for actin visualization and Hoechst (1:2500, Invitrogen) for the nucleus, for 1 h at room temperature. Corresponding secondary antibodies were purchased from Invitrogen.

2.2.10 Immunofluorescence image line profiles. Images were imported in ImageJ and lines spanning the entire length of the cells were manually traced through the cell center. Line profile measurements of pixel intensity were calculated on ImageJ. Normalization of

the cell length to the maximum cell length was performed in Microsoft Excel and plots were created via GraphPad Prism 6 and 7.

2.2.11 Confocal imaging. Cells were imaged with a Nikon A1 confocal microscope (Nikon, Tokyo, Japan) using 60/63x oil objective with a 1.4 numerical aperture and a resolution of 1024x1024 pixels. The lasers used for imaging were either 405-nm, 488-nm, 567-nm or 640-nm.

2.2.12 Actin flow measurements and quantification. - LifeAct-GFP MDA-MB-231 cells were seeded in the microfluidic devices as described above. A z plane just above the basal surface was selected. Cells in the microchannels were imaged using a Nikon A1 Confocal microscope (Nikon, Tokyo, Japan) with a 488-nm laser and a 60x oil objective at a resolution of 1024x1024 pixels every 2-4 sec for 5 min. Actin flow quantification and visualization was performed via the Particle Image Velocimetry tool for Matlab (PIVlab) (Thielicke and Stamhuis, 2014). For selected experiments, the length of the cells was normalized to their maximum length, 5% of the length incremental bins were created and actin flow velocities were averaged over n >= 19.

2.2.13 TFM measurements. Devices and cells were imaged with a Nikon A1 confocal microscope (Nikon, Tokyo, Japan) using a 60x oil objective with a 1.4 numerical aperture and a 1024x1024 pixel resolutions. 0.2 μm z-stacks were performed over the entire HEMICA before the cells were seeded in order to capture the original positions of the fluorescent beads. After cells were seeded, 0.2 μm z-stacks were performed every 5 min

for 30 min. The z-stack of each position with cells inside the channels was registered to the z-stack of the same position of the channel without the cells, and bead displacements from their original (no cell) position were calculated over time using a custom made MATLAB code. Based on the bead displacements and the stiffness of the gels, we calculated the deformation gradient, the Cauchy finite strain tensor, the Lagrangian finite strain, the Cauchy-Green deformation tensor, the infinitesimal volume change and finally the Cauchy stress tensor which gave us values for shear and normal traction forces.

2.2.14 FRET. Transiently transfected MDA-MB-231 cells expressing the RhoA2G biosensor were imaged for CFP (ex: 430/24, em: 470/24), YFP (ex: 500/20, em: 535/30) and FRET (ex: 430/24, em: 535/30). The Nikon Elements software (Nikon, Tokyo, Japan) was used for background subtraction and outlining of the cell boundary by tracing the YFP image (Hung, Chen et al. 2013). The mean pixel ratio of FRET over CFP is reported.

2.2.15 Western Blotting. Western blots were performed as previously described (Wang, Zhu et al. 2012, Chen, Hung et al. 2013) using NuPage 4-12% gels. Primary antibodies used include: anti-MIIA antibody (rabbit) (Sigma Aldrich M8064, 1:1000), anti-MIIB antibody (rabbit) (Cell Signaling 3404S, 1:1000), anti-integrin β1 antibody (mouse) (Abcam, anti-integrin beta 1 antibody (12G10), ab30394, 5 μg/mL), anti-NHE1 antibody (mouse) (Santa Cruz Biotechnology, NHE-1 (B-12), SC-515950, 1:200), anti-β-actin (Purified Mouse Anti-Actin Ab-5, BD Biosciences 612656, 1:10,000), anti-GAPDH (rabbit) (Cell Signaling, GAPDH (14C10), #2118, 1:1000).

Secondary antibodies used include: anti-mouse IgG, HRP-linked antibody (Cell Signaling 7076S, 1:2000), anti-rabbit IgG, HRP-linked antibody (Cell Signaling 7074S, 1:2000), donkey anti-goat IgG-HRP (Santa Cruz biosciences, SC-2020, 1:2000).

2.2.16 Focal adhesion quantification. 0.2 μm z-stacks of MDA-MB-231 paxillin-GFP cells were taken for the entire height of the microchannel. Common background subtraction for all z-stacks of every cell was performed using NIS-Elements (Nikon), followed by pixel smoothing (2x), linear background subtraction using a constant (100), detection of regional maxima (2x), and thresholding (50-4095). Basal, apical and lateral surfaces were separated from the z-stacks and the identified adhesions of each stack were 3D reconstructed for the lateral surfaces. Mean area, length and number of adhesions were calculated for the 2D (apical and basal) surfaces while surface area, major axis of a fitted ellipse and number were calculated for the lateral surfaces. Adhesions with a maximum feret value less than 0.25 μm and greater than 10 μm were excluded.

2.2.17 Contact guidance quantification. Analyzed cell tracks (MtrackJ plugin in ImageJ) of live cell videos were used with a custom MATLAB script. The known position of the lateral channel walls and channel center line were used to identify jumps (the number of times a cell crossed the channel center line along its path) and the percentage of cell locations over time which lay in a ROI 7 μm away from the lateral channel walls.

2.2.18 Swelling ratio measurements. PA gels of 12, 26 and ~50 kPa stiffness, and volume 100 μL and 1 mL were generated as described earlier. Gels were allowed to swell in PBS

-/- at 37 °C and their weight (Ws) was measured daily. When the swelling period ended, the same gels were allowed to dry in open air and their weight was measured at time points 0, 2, 4, 6, 8 and 24 h. Subsequently, the gels were lyophilized and their dry weight was measured (Wd). Their swelling ratio was calculated based on the formula: swelling (%) = ((Ws – Wd) / Wd) x 100.

2.2.19 Stiffness (stress vs strain) measurements. Gels were cut with 6 mm biopsy punches to create samples of similar dimensions. A rheometer was used to apply mechanical compressive loads to the gels up to a recorded strain of ~10%. Stress vs strain curves were generated and the Young's modulus of the samples was calculated based on the formula: $E = \sigma / \varepsilon$ (Young's modulus = stress / strain).

2.2.20 Morphological measurements. Live cell videos were imported in ImageJ. The perimeter of the cells was manually traced in every frame for the duration of their migration through the channels. Cells which were dividing or interfering with other cells were excluded. Measurements of aspect ratio, circularity, area variance, circularity variance, roundness, max ferret diameter, solidity and solidity variance were generated via a custom made MATLAB script.

2.2.21 Statistical Analysis. Data represent the mean ± SD or S.E.M. from >= 2 independent experiments for each condition. 2-way ANOVA, one-way ANOVA followed by Kruskal-Wallis test and Mann-Whitney (non-parametric) test were used to determine

significance as appropriate. Statistical significance was identified as $p < 0.05$. Analysis was performed using GraphPad Prism 6 and 7.

2.3 Results

2.3.1 Fabrication of the Hydrogel Encapsulated Microchannel Array (HEMICA). To study cell migration in an environment where ECM stiffness and channel size are independent of one another, we used photolithography techniques as well as polyacrylamide (PA) gels, whose stiffness can be highly regulated to stay within physiological levels. First, we microfabriacated migration channels on a silicon wafer and then used the wafer as a mold upon which we polymerized PA (Fig. 2-1.Ai). As a result, the microchannel design was imprinted on the lower surface of the gel (design-gel). Second, we activated coverslips and polymerized a thin (~60-100 μm) flat layer of PA (flat-gel) with the same or different stiffness than the design-gel (Fig. 2-1.Aii). Both the flat-gel and the design-gel were allowed to reach their maximum swelling in PBS at 37 °C. The volume of PA, the stiffness and the temperature in which the gels are kept are important factors in determining the time needed to reach their maximum uptake of PBS (Park and Hoffman 1992). In addition, based on the stiffness of the gels we observed different final gel volume maxima (Fig. 2-1.B), with the stiffer gels reaching a lower swelling ratio than the softer ones. Furthermore, since the flat-gels contained a smaller volume of liquid, they dried much faster than the design-gels, which indicated that the time gels stayed outside of a hydrating liquid had to be minimized. Once the gels were swollen, we air-blew the excess PBS from the surfaces of the gels, punched inlet/outlet holes on the design-gel and spread BS3 on the surface of the flat-gel (Fig. 2-1.Aiii). Subsequently, we

placed the design-gel on top of the flat-gel and allowed them to adhere. BS3, as an NHS-ester and at a slightly basic pH, formed a monolayer of amide bonds with the primary amines of the PA gels (Fig. 2-2.A). As a result, we bonded two gel surfaces together, encapsulated the microchannels in-between the gels and created a device in which either all four walls of microchannels were made out of the same material and presented the same physiologically relevant stiffness (isotropic gels) or the flat-gel had a different stiffness than the top design-gel (anisotropic gels) (Fig. 2-1.C, Fig. 2-2.B). Furthermore, we were able to imprint a microchannel array which allowed us to study cell migration under various degrees of confinement, with or without chemical or osmotic gradients. Finally, in order to adhere cells on the device we used sulfosuccinimidyl 6-(4'-azido-2'-nitrophenylamino)hexanoate (Sulfo-SANPAH) to coat the encapsulated microchannels with the desired ECM protein (Fig. 2-1.Aiv). Once, the cells were seeded, we submerged the device in media in order to create an environment with no flow, no gradients and preserve the volume of the flat-gel, thus avoiding loss of gel-to-gel adhesion due to unequal shrinkage of the design-gel and the flat-gel. In our attempt to mimic healthy to cancerous breast tissue stiffness (Krouskop, Wheeler et al. 1998, Engler, Sen et al. 2006, Golatta, Schweitzer-Martin et al. 2013), we fabricated HEMICAs of 12, 26 and ~50kPa Young's modulus (low, intermediate and high stiffness), and confirmed the stiffness using a rheometer (Fig. 2-1.D).

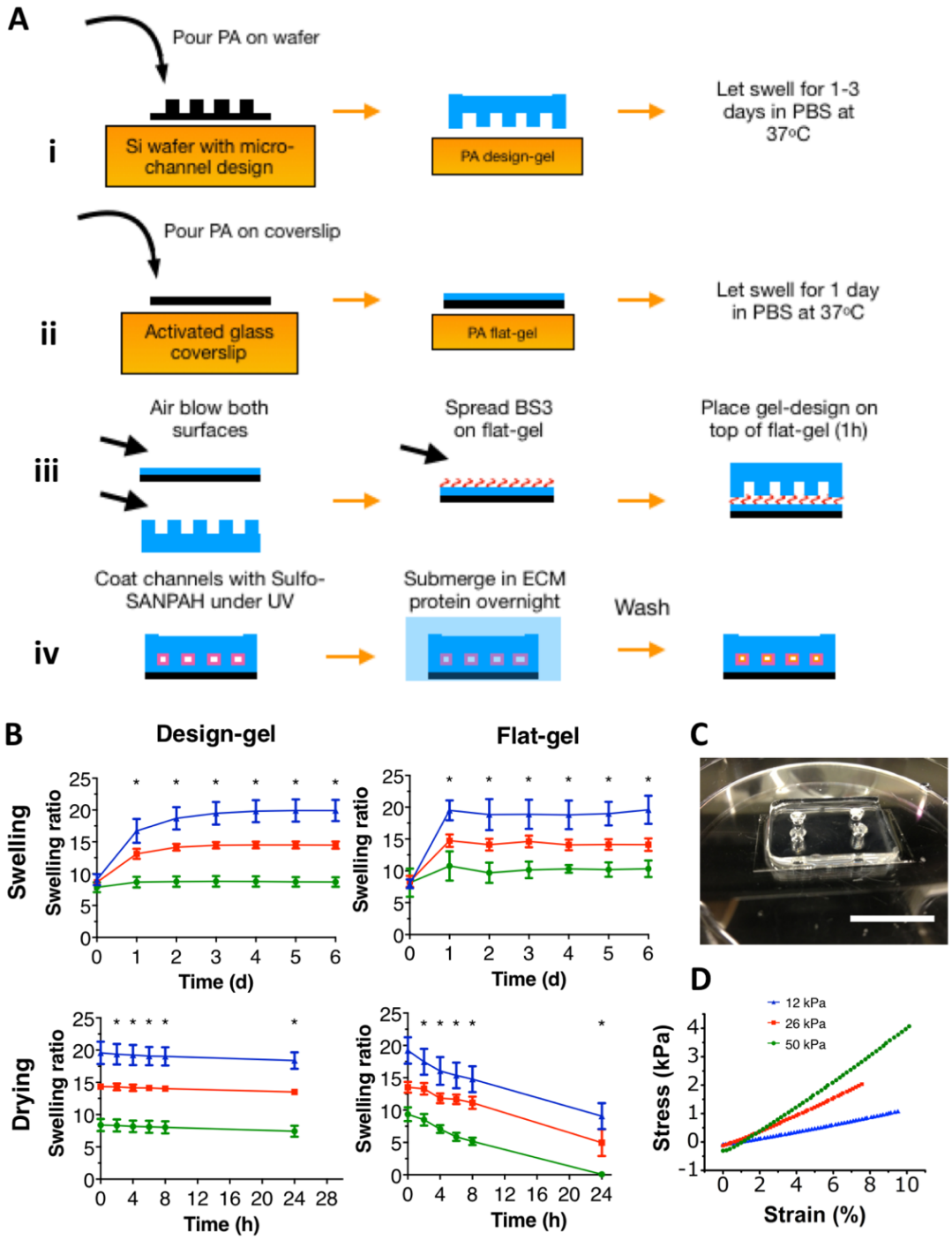

Figure 2-1. HEMICA fabrication and characterization. (**A**) Schematic representation of the production of polyacrylamide (PA) gels with microfluidic tracks, assembly of

HEMICA and ECM protein coating. (**B**) Swelling ratios of the design-gel (1 mL of PA mix) and the flat-gel (100 μL of PA mix). The weight of the gels for swelling in PBS at 37 °C was measured daily, while the weight of the gels drying in open air was measured at 0, 2, 4, 6, 8 and 24 hours after reaching their maximum swelling (3 gels for each stiffness). Dry weight was measured after lyophilization. (**C**) Picture of assembled HEMICA (dimensions of coverslip: W x L = 22 x 40 mm; white bar represents 15 mm). (**D**) Representative stress-strain curves from rheological measurements for calculation of gel stiffness (n = 2 independent experiments, 3 gels of 100 μL PA mix for each stiffness). Data represent the mean ± SD. * $p < 0.05$ relative to each of the other two stiffnesses for the same time point, 2-way ANOVA was performed.

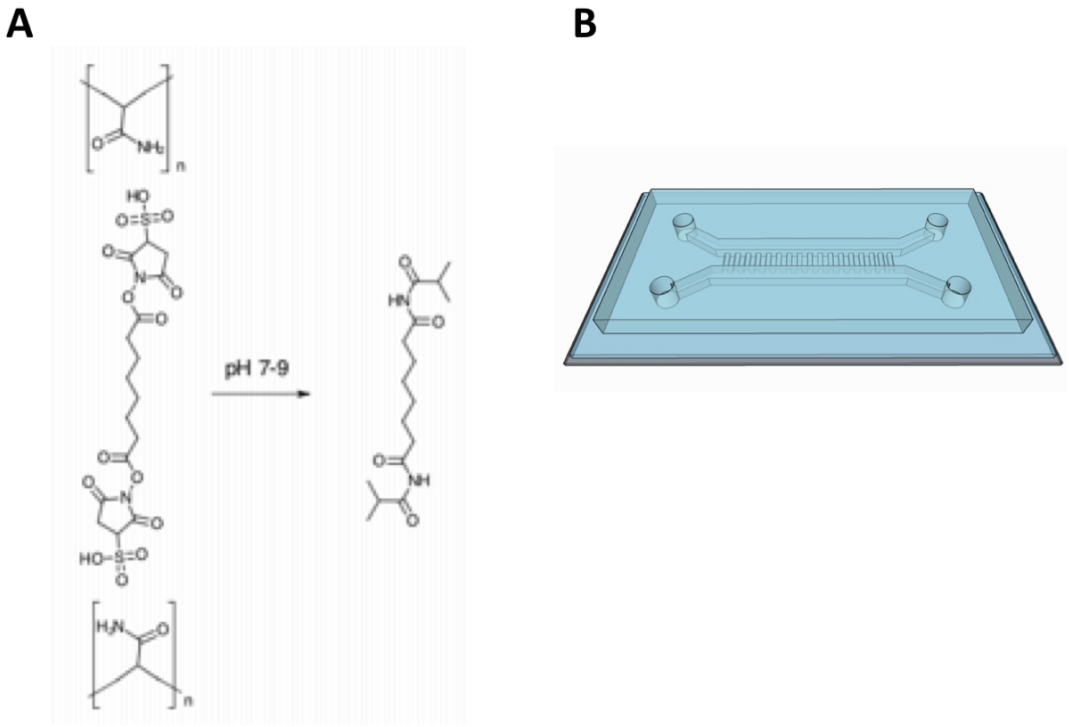

Figure 2-2. Chemical reaction responsible for production of HEMICA and HEMICA design. (**A**) Schematic representation of amide bond formation reaction between the primary amines of the top and bottom (design-gel and flat-gel) and the NHS-ester ligand bis(sulfosuccinimidyl)suberate (BS3). (**B**) Sketch of HEMICA design.

2.3.2 HEMICA Reveals the Biphasic Relationship Between Cell Speed and Degree of Confinement or Matrix Stiffness, the Induction of Cell Morphodynamic Changes and the Stiffness Regulated Contact Guidance. In order to decipher the relationship between cell speed, degree of confinement and matrix stiffness, we used MDA-MB-231 human breast cancer cells in collagen I coated HEMICAs of low, intermediate and high stiffness, and created a microchannel array containing channels of constant height and length (H = 10 μm, L = 200 μm), yet with variable widths. In this way, we were able to investigate the speeds as well as morphological cell responses in a range of microenvironments spanning from high confinement (W = 3 μm) to no confinement (W = 50 μm). Irrespective of the stiffness, we observed that speed varied biphasically with channel width, reaching a single optimum around W = 10 μm (Fig. 2-4.A). In addition, for every channel width, speed varied biphasically with substrate stiffness, showing a single optimum at intermediate stiffness, which lies on the cusp between healthy and cancerous breast tissue (Fig. 2-3.A). Cell persistence or chemotactic index increased monotonically with stiffness, showing higher values at higher stiffness, especially for widths larger than 10μm, which cells recognize as a 2D-like environment (Fig. 2-3.B). Intermediate and high stiffness increased cell polarization in confinement (W = 3, 6 μm), as seen from aspect ratio measurements (Fig. 2-3.C). Reversely, cell circularity and roundness was higher in low stiffness throughout all channel widths, suggesting reduced cell-matrix adhesions (Fig. 2-3.D, Fig. 2-4.B). While the maximum feret diameter, which represents the largest point to point distance within a cell for the duration of its migration, was relatively equal through most channel widths and stiffnesses, solidity, which is a variable indicating how protrusive a cell is, showed consistently lower values on intermediate stiffness gels regardless of the degree

of confinement (Fig. 2-4.D). On the other hand, the variance of solidity was greater in the confining widths at intermediate stiffness, with the biggest differences in the 10 μm width channels (Fig. 2-4.E). Cells, at this particular optimum of stiffness and confinement, moved faster and more dynamically, as they kept varying their small protrusions in order to attain high speeds. Moreover, we observed that the variance of the area and circularity of the cells increased in low stiffness almost through all channel widths, as cells implemented drastic morphodynamic changes in the process of achieving an optimum mode of migration at low adhesion environments (Fig. 2-3.E, F).

The large widths of our microchannel array allowed cells to move in a 2D-like environment yet also presented a special topography at the intersection between two channel walls. Cells can sense the existence of both bottom and side walls, and migrate preferentially along one side of the microchannel (contact guidance) (Paul, Shea et al. 2016). Through HEMICA, we could observe how substrate stiffness influences contact guidance. Based on the number of times cells crossed the center-line of the channel (jumps) and the probability of following a path within the central region of the channel, we showed that low stiffness regimes reduce contact guidance (Fig. 2-3.G, H).

To sum up, HEMICA allowed us to observe a biphasic behavior in cell speed through various degrees of confinement and stiffness, and categorize cell behavior in low and high stiffness regimes, where low stiffness induces great morphodynamic changes, less contact guidance and invokes rounder cells, while higher stiffness increases cell persistence and polarization. Confinement, accentuates traits such as cell polarization/aspect ratio, while it attenuates others such as drastic changes in cell area.

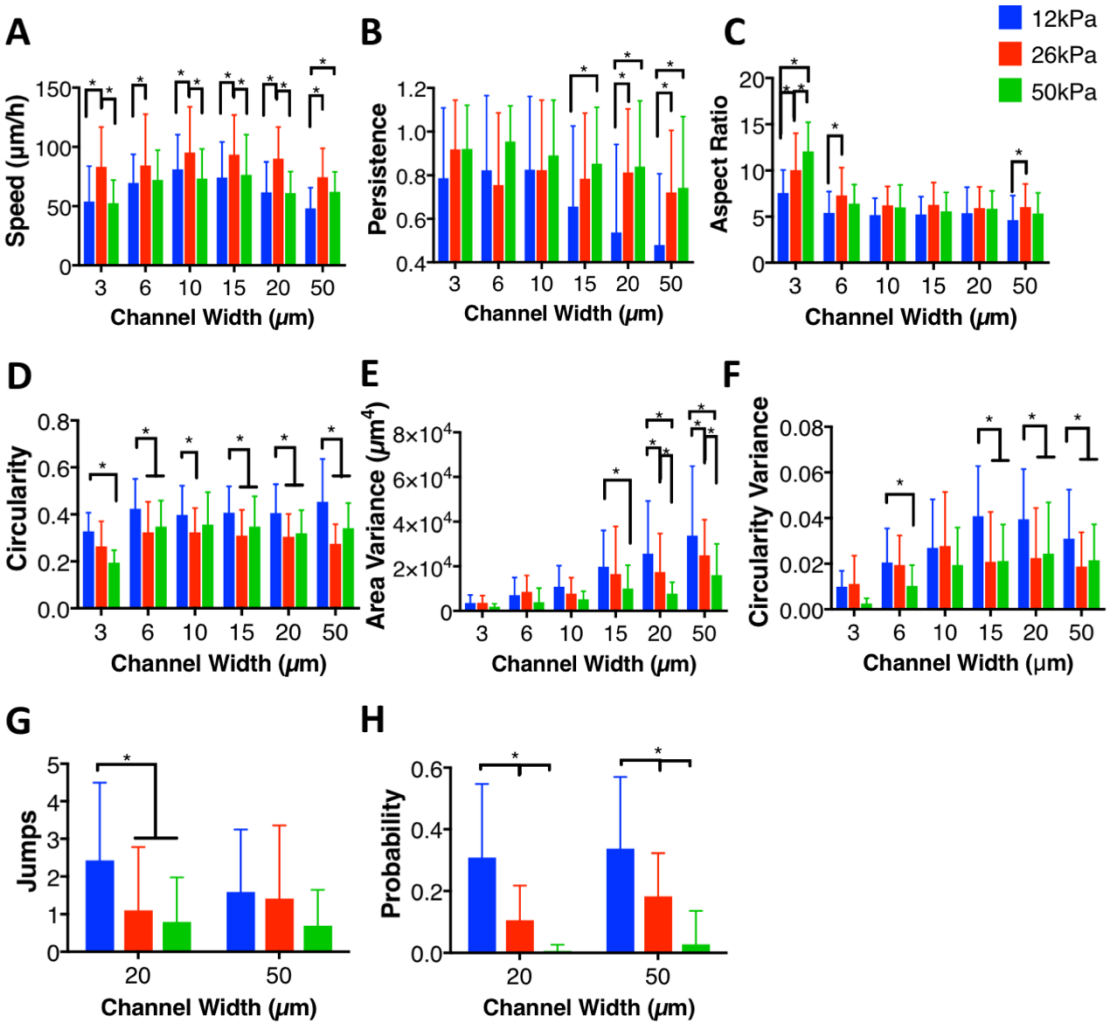

Figure 2-3. Physiological stiffnesses affect cell speed, induce morphodynamic changes and regulate contact guidance. (**A**) Migration speed, (**B**) Persistence of MDA-MB-231 cells in 12, 26 and 50kPa HEMICAs across channels of fixed height and length (H = 10 μm, L = 200 μm) with width spanning from 3 μm to 50 μm (n >= 23, pulled from 6 independent experiments). (**C**) Aspect ratio, (**D**) Circularity, (**E**) Area variance, (**F**) Circularity variance of MDA-MB-231 cells in 12, 26 and 50kPa HEMICAs across channels of fixed height and length (H = 10 μm, L = 200 μm) with width spanning from 3 μm to 50

μm (n >= 23, pulled from 6 independent experiments). (**G**) Average number of jumps (number of times cells crossed the center line of a microchannel) of MDA-MB-231 cells in 12, 26 and 50kPa HEMICAs across channels of fixed height and length (H = 10 μm, L = 200 μm), and large widths (20 and 50 μm) (n >= 39, pulled from 6 independent experiments). (**H**) Average probability of MDA-MB-231 cells migrating along the central portion of a microchannel, 7 μm away from the lateral channel walls in 12, 26 and 50kPa HEMICAs across channels of fixed height and length (H = 10 μm, L = 200 μm), and large widths (20 and 50 μm) (n>=39, pulled from 6 independent experiments). Data represent the mean ± SD. * $p < 0.05$ relative to the other stiffnesses for the same channel width, 2-way ANOVA was performed.

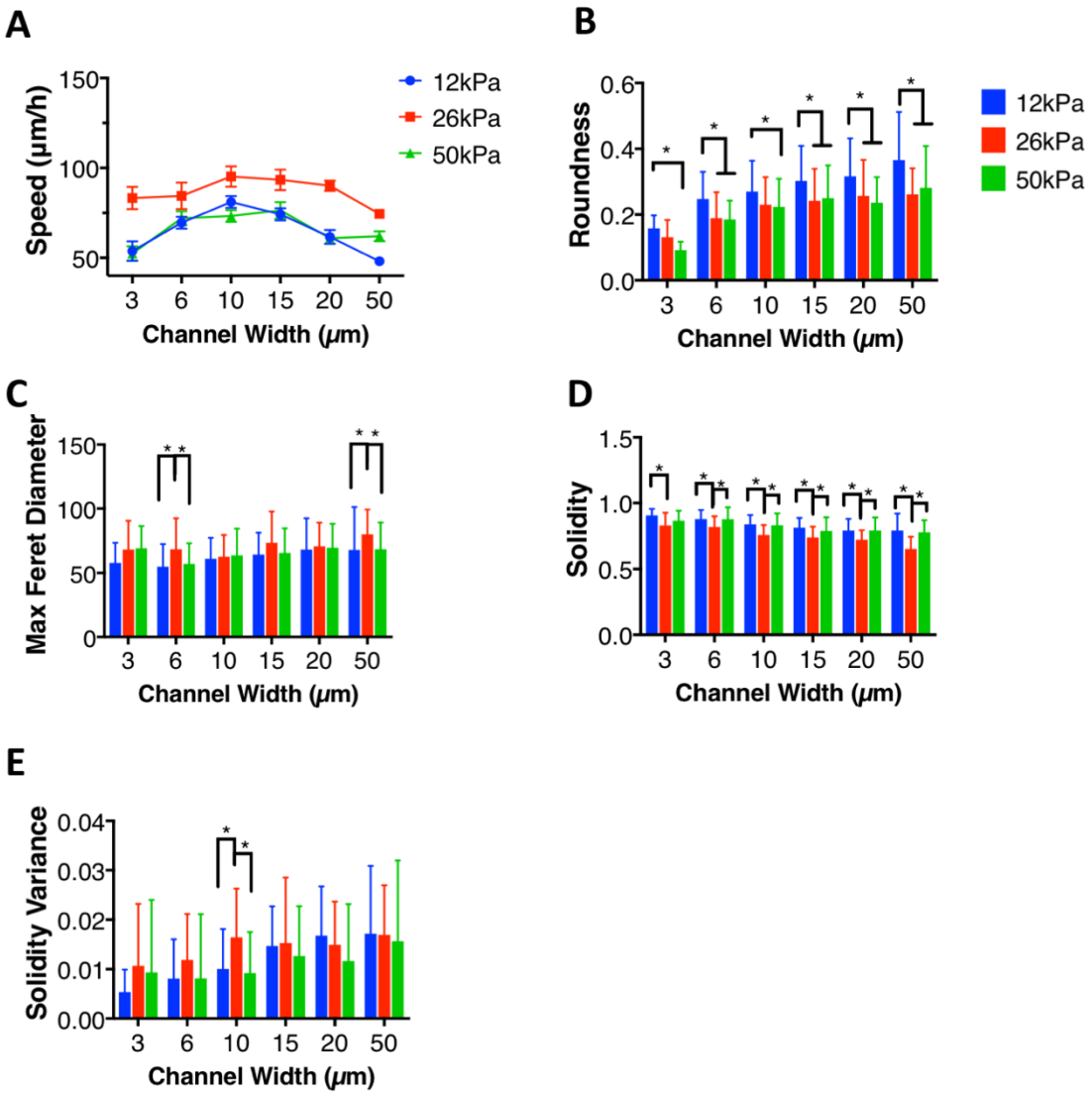

Figure 2-4. Speed measurements and morphological analysis in HEMICA. (**A**) Migration speed of MDA-MB-231 cells in 12, 26 and 50kPa HEMICAs across channels of fixed height and length (H = 10 μm, L = 200 μm) with width spanning from 3 μm to 50 μm (n >= 23, pulled from 6 independent experiments). Data represent the mean ± S.E.M. (**B**) Roundness, (**C**) Maximum Feret Diameter, (**D**) Solidity, (**E**) Solidity variance of MDA-MB-231 cells in 12, 26 and 50kPa HEMICAs, across channels of fixed height and length

(H = 10 μm, L = 200 μm) with width spanning from 3 μm to 50 μm (n >= 23, pulled from 6 independent experiments). Data represent the mean ± SD. * $p < 0.05$ relative to the other stiffnesses for the same channel width, 2-way ANOVA was performed.

2.3.3 HEMICA Generates Anisotropic Environments, Allows Experiments with Chemotactic Gradients, Supports the Use of TFM and Helps Monitor Collective and Single Cell-file Migration. The distinct HEMICA assembly process which involves bonding an upper design-gel containing three of the micro-channel walls to a lower flat-gel that provides the base of the channels allowed us to create microenvironments of varying stiffness between the top/side and the bottom. Thus, we could emulate tissue topographies where the basal cell surface lies on the stiffer basement membrane or on muscle fibers and the rest of the cell is in contact with softer surrounding connective tissue. Knowing that confined migration in intermediate stiffness gels was faster than in low stiffness ones, we performed experiments in which the design-gel (that provided the apical and lateral surfaces of a microchannel) and the flat-gel (that provided the basal surface of a microchannel) were mixed and matched. This resulted in 4 different HEMICAs with the following apicolateral to basal stiffness of microchannel combinations: 12 kPa on 12 kPa, 12 kPa on 26 kPa, 26 kPa on 12 kPa and 26 kPa on 26 kPa. While confined migration (W x H: 3 x 10 μm) in the isotropic (12 on 12) and (26 on 26) HEMICAs was the slowest and fastest respectively, the anisotropic HEMICAs showed intermediate results. The change of one surface made the cells move with a speed closer to that of the isotropic equivalent of that surface. Going from the 12 on 12 gel to the 12 on 26 gel made cells faster, since the 26 on 26 is the fastest environment, and going from the 26 on 26 to the 26 on 12 gel made cells slower, since the 12 on 12 is the slowest environment (Fig. 2-5.A). A similar pattern was seen in cell velocities (Fig. 2-6.A). In terms of persistence, the variations between the slowest isotropic and the anisotropic gels were too small yet in the right direction, and the fastest isotropic gel (26 on 26) showed a significantly higher persistence than all other

combinations (Fig. 2-6.B). As a control, we measured the speed of non-contact guided MDA-MB-231 cells in anisotropic HEMICAs of W = 50 μm which should not have been affected by the design-gel (Fig. 2-6.B). As expected, cell speeds on HEMICAs with 12 kPa and 26 kPa basal flat-gels where different, while cells on HEMICAs with the same stiffness flat-gel migrated with similar speeds regardless of the apicolateral gel stiffness. These results indicated that the stiffness of the walls of a microchannel can differentially affect cell migration when cells are in contact with all of them.

In all of our experiments so far, we have been submerging HEMICAs in media for two reasons; first in order to study migration when no gradients are present, and second, to ensure that the hydrogels won't shrink over time. In order to study migration under a gradient, however, we managed to maintain the bonding of the flat-gel to the design-gel and prevent shrinkage by increasing the humidity in the live-microscopy incubator chamber. Simply adding more DI water in the chamber allowed the devices to stay intact for the course of at least 15 h experiments. In order to showcase that HEMICA can be used in experiments with chemotactic gradients, we added 1% FITC-dextran on the top wells of a 26 kPa HEMICA and PBS on the bottom ones. Under no flow conditions, we established a gradient through the microchannels (blue), in-between the upper (cell exit side - red color Region Of Interest (ROI)) and the lower (cell seeding side - green color ROI) sides of the device (Fig. 2-5.C). Mass transfer allowed for a stable gradient that lasted at least 15 h (Fig. 2-5.D). By normalizing the fluorescence intensity of the ROIs over time to the maximum intensity of the upper ROI, we observed that the channel ROI average intensity was in intermediate levels between the upper and lower ROIs (Fig. 2-5.E). After showcasing the establishment of gradients in HEMICA, we generated a 10% FBS gradient in 12 kPa

HEMICAs and tested the response of MDA-MB-231 cells in confined microchannels (W x H: 3 x 10 μm). The chemotactic gradient, evidently, increased the speed and the persistence of migration (Fig. 2-5.F, G).

By adding fluorescent nanospheres to the polyacrylamide mix, we were also able to use HEMICA for 3D traction force microscopy (TFM). Thus, we examined the traction forces exerted by MDA-MB-231 cells in confined microchannels (W x H: 3 x 10 μm) in 12, 26 and 50 kPa HEMICAs. As shown by the representative heat maps, both normal and shear traction forces increased with stiffness (Fig. 2-6.C). Average normal forces throughout the cell were almost double in magnitude than the shear forces in each stiffness. In addition, normal forces pushed/indented the micro-channel walls as the cells migrated through the preformed tracks. On the lower stiffnesses, shear and normal forces were concentrated around the nuclear region, which indicated that the nucleus becomes a barrier in soft substrate confined migration. On the higher stiffnesses, traction forces were spread throughout the cell body, suggesting a greater interaction between the walls and the cell membrane.

In addition to single cell migration, HEMICA can be used to study collective or single cell file migration, which are both prevalent in-vivo (Alexander, Koehl et al. 2008). To exhibit both of these uses, we used a multichannel design with channels of fixed height and length (H: 10 μm, L: 200 μm), yet with widths ranging from 3 μm to 50 μm. Subsequently, we formed a confluent monolayer of A431 squamous cell carcinoma cells on the cell seeding areas of 50 kPa HEMICAs. Cells entering the larger (50 μm and 20 μm) width channels used a collective mode of migration (Fig. 2-5.H, I), while cells in smaller width channels migrated as single cells or single cell-files (Fig. 2-5.J).

To sum up, we were able to use HEMICA to create isotropic and anisotropic stiffness microenvironments, environments that promote collective and single cell file migration, and chemotactic gradients. Our experiments raise the importance of the basal and apicolateral walls of a microchannel in confined migration and prove that HEMICA is multifaceted tool that can be used for studies with chemical gradients and TFM.

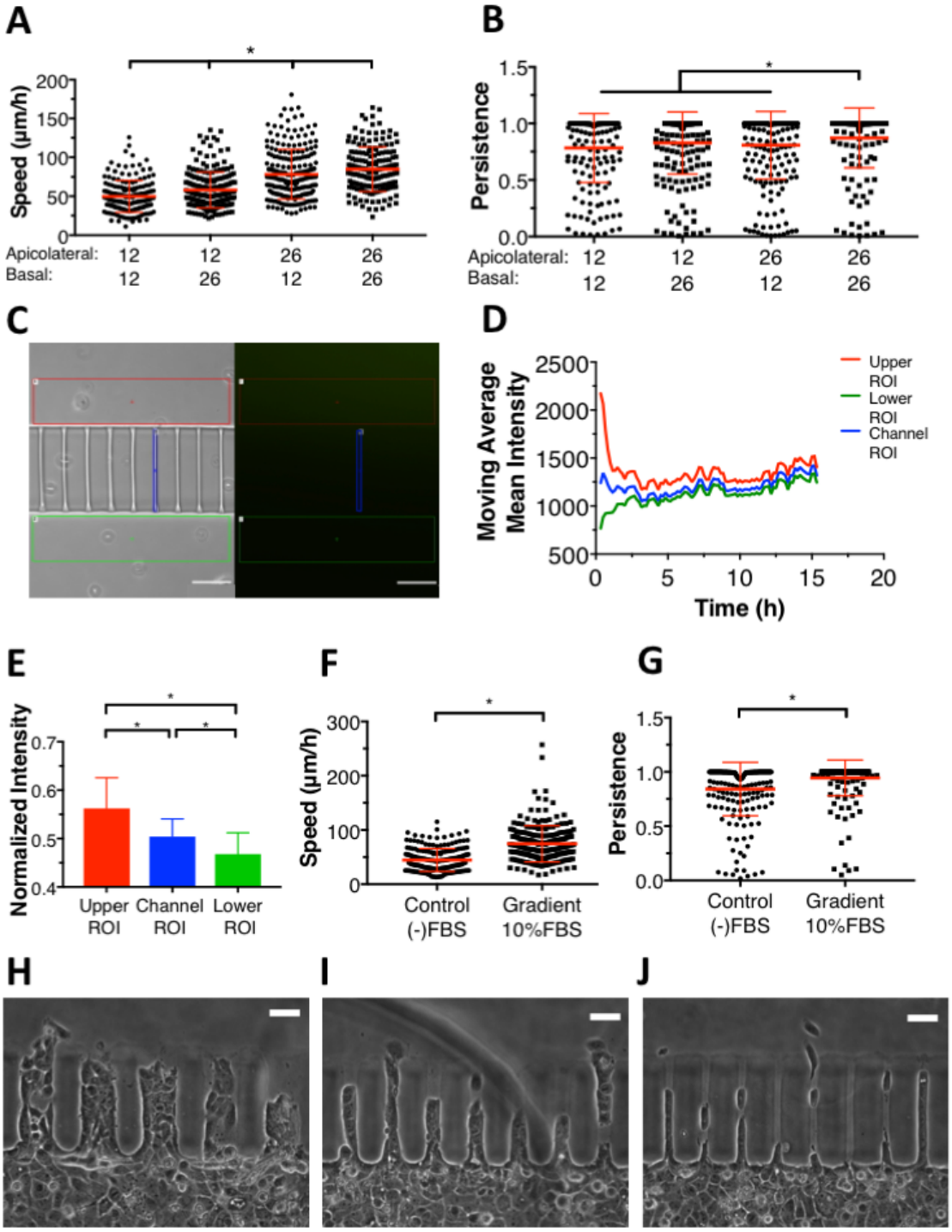

Figure 2-5. HEMICA is a multifaceted tool which can be used to generate stiffness anisotropy and chemotactic gradients, study collective and single cell-file migration,

and analyze forces in 3D through Traction Force Microcopy (TFM). (**A**) Confined migration speed, (**B**) Persistence of MDA-MB-231 cells in isotropic and anisotropic HEMICAs of apicolateral (top) on basal (bottom) PA stiffness gel combinations: 12 on 12 kPa, 12 on 26 kPa, 26 on 12 kPa, 26 on 26 kPa. The channel height, length and width were H = 10 μm, L = 200 μm, W = 3 μm (n >= 170, 3 independent experiments were performed). One-way non parametric ANOVA (Kruskal-Wallis test) was performed, * $p < 0.05$. (**C**) Phase contrast image (left) and FITC image (right) of 26 kPa HEMICA showing H = 10 μm, L = 200 μm, W = 3 μm microchannels with 1% wt/vol FITC-Dextran added on the top side and PBS on the bottom for chemotactic gradient measurements. Red, green and blue boxes represent the upper, lower and channel ROIs used for fluorescence measurements. Scale bars represent 100 μm. (**D**) Representative moving average (average over 3 frames, 10 minutes per frame) of mean FITC-Dextran fluorescence intensity over time for all three aforementioned ROIs (2 independent experiments were performed). (**E**) Representative graph of mean FITC-Dextran fluorescence intensity of all three aforementioned ROIs normalized to the upper ROI (red box). One-way non parametric ANOVA on ranks (Kruskal-Wallis test) was performed, * $p < 0.05$. (**F**) Confined migration speed, (**G**) Persistence of MDA-MB-231 cells through H = 10 μm, L = 200 μm, W = 3 μm channels in 26 kPa HEMICA under 10% fetal bovine serum (FBS) as a chemoattractant. Mann-Whitney (non-parametric) test was performed, * $p < 0.05$. (**H**) Image of collective migration of A431 cells through 50 μm channels in 50 kPa HEMICA. (**I**) Image of collective migration of A431 cells through 20 μm channels in 50 kPa HEMICA. (**J**) Image of single cell and single cell-file migration of A431 cells through 10 μm channels in 50 kPa HEMICA. Scale bars represent 50 μm. Data represent the mean ± SD. * $p < 0.05$.

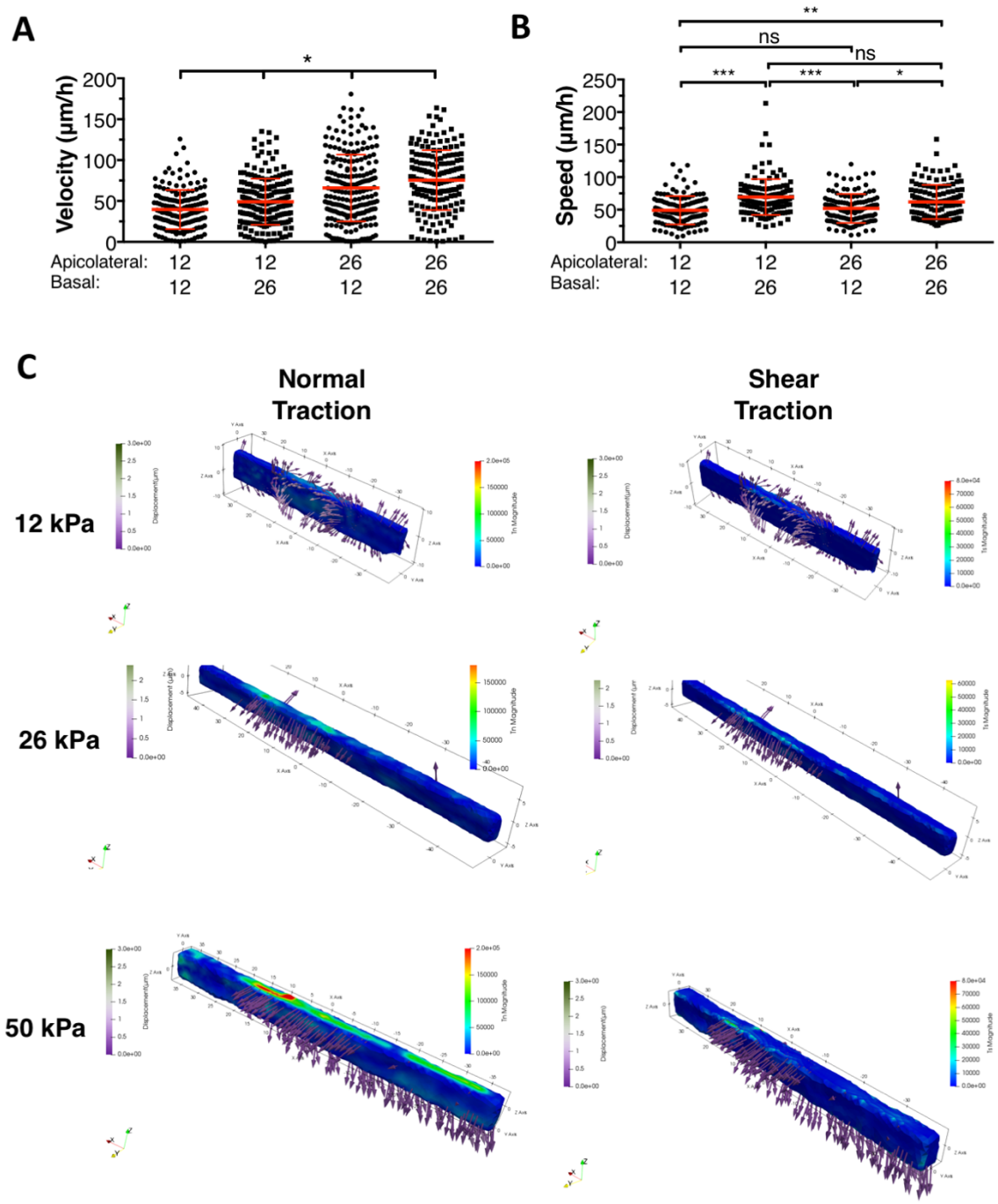

Figure 2-6. Stiffness anisotropy and TFM. (**A**) Confined migration speed of MDA-MB-231 cells in isotropic and anisotropic HEMICAs of apicolateral (top) on basal (bottom) PA

stiffness gel combinations: 12 on 12 kPa, 12 on 26 kPa, 26 on 12 kPa, 26 on 26 kPa. The channel height, length and width were H = 10 μm, L = 200 μm, W = 3 μm (n >= 170, 3 independent experiments were performed). One-way non parametric ANOVA (Kruskal-Wallis test) was performed, * $p < 0.05$. (**B**) Migration speed of non-contact guided MDA-MB-231 cells in isotropic and anisotropic HEMICAs with the aforementioned combinations through 2D-like channels with dimensions H = 10 μm, L = 200 μm, W = 50 μm (n = 129, 4 independent experiments were performed). One-way non parametric ANOVA (Kruskal-Wallis test) was performed, * $p < 0.05$, ** $p = 0.0007$, *** $p < 0.0001$. (**C**) Representative 3D heatmaps of normal and shear traction forces in 12, 26 and 50 kPa HEMICAs. The heatmap scale bars include the highest occurring values of traction forces. Data represent the mean ± SD.

2.3.4 Confined Migration in Physiologically Relevant Stiffness in HEMICA Reveals the Important Roles of Myosin IIA-based Contractility, Integrin β1 and Focal Adhesions. In our attempt to dig deeper into the elements that affect non-proteolytic confined cell migration, we fabricated HEMICAs of intermediate stiffness (26 kPa) (in which cells exhibited optimum speeds), fixed the channel width to 3 μm and analyzed the migration of MDA-MB-231 cells in HEMICA compared to PDMS-based microfluidic devices, which are the current golden standard in the field.

In PDMS, inhibition of contractility with a high dose of blebbistatin had a minor effect in cell speed (Fig. 2-6.A) and no effect in cell persistence (Fig. 2-7.A). In HEMICA cell speed and persistence reduced dramatically (Fig. 2-6.A, Fig. 2-7.A), indicating the importance of contractility in soft substrate migration.

To elucidate the roles of the primary myosin isoforms which are implicated in cell migration, we generated MIIA (Myh9), MIIB (Myh10) and combined MIIA and MIIB knock-downs (Fig. 2-6.G). Our results showed that MIIA is the primary myosin responsible for soft substrate confined migration, since it reduced the speed (Fig. 2-6.B) and persistence (Fig. 2-7.B) of migrating cells. MIIB did not affect any of these parameters (Fig. 2-7.C, D), and more importantly, there was no additive effect from the combined knock-down (Fig. 2-7.E, F). As expected from the pharmacological inhibition of contractility, none of the major myosin genes that affect migration had any effect on migration in PDMS (Fig. 2-6.B, Fig. 2-7.B-F). However, the elevated levels of RhoA in PDMS compared to HEMICA (Fig. 2-6.E) would have signified a greater impact of contractility in stiff substrate migration. To clarify this point, we stained for phosphorylated myosin light chain (pMLC), a downstream effector of MLCK which in turn is regulated by RhoA. In PDMS,

pMLC was localized on the front and rear of the cell, whereas in HEMICA it was present throughout the entire cell body (Fig. 2-6.C, D). As a result, we attributed the loss of importance of contractility in PDMS and reversely the gain of importance in HEMICA to the polarization of pMLC which rendered the cells unable to push and pull the cell body efficiently.

Focal adhesions and integrins are crucial for 3D migration and their function is closely interrelated to myosin contractility for the propagation of contractile forces to the extracellular environment. As such, we set forth to investigate their role on confined migration in PDMS versus in 26 kPa HEMICA. Since integrin β1 is abundant in MDA-MB-231 cells and mediates adhesion to collagen I, we generated knock-downs (Fig. 2-7.H) and studied their migration in collagen I coated PDMS microchannels and 26 kPa HEMICAs. In PDMS, integrin β1 was dispensable for migration since β1-KD showed no difference in speed compared to scramble control cells (Fig. 2-6.F). On the other hand, β1 played a crucial role in soft substrate migration, since the knock-down almost abrogated migration (Fig. 2-6.F).

In order to understand why integrin β1 had no significant effect in stiff substrate migration and also further elucidate the role of focal adhesions in soft substrate confined migration, we transduced our cells with paxillin-GFP, used confocal microscopy and performed 0.2 μm z-stacks over the entire channel height. Subsequently, we reconstructed the z-stack volume of adhesions in 3D, split the field on four wall surfaces (basal, apical and two lateral) and revealed the existence of adhesions all around the cell body. Compared to PDMS, paxillin-rich adhesions on the basal and lateral surfaces in HEMICA were smaller (Fig. 2-6.G, H, Fig. 2-8.A, C, Fig. 2-9.A) and on average their number on the basal

plane was the same (Fig. 2-8.B). Similar trends were observed on the basal focal adhesions on the 2D region of the devices (Fig. 2-8.E-G). On the contrary, adhesions on the apical surfaces had no significant differences (Fig. 2-8.H-J). Surprisingly, when integrin β1 was knocked down, although lateral and apical adhesions were eliminated in PDMS (Fig. 2-6.H, F, Fig. 2-8.C,D, H-J, Fig. 2-9.A), on the basal surface their size remained the same (Fig. 2-6.G, Fig. 2-8A, Fig. 2-9.A) and their number increased as compared to scramble control (Fig. 2-8..B, Fig. 2-9.A). As a result, while the lateral and apical adhesions did not seem to influence cell speed, the basal adhesions proved to be critical in stiff substrate confined migration. On the 2D region of PDMS devices, adhesion size of integrin β1 knock-down cells reduced yet their number showed an increasing trend (Fig. 2-8.E-G). On the other hand, in HEMICA integrin β1 knock-down eliminated all adhesions from all planes in confinement and on 2D (Fig. 2-6.G, H, Fig. 2-8.A-J, Fig. 2-9.A). Considering the major impact of myosin in soft substrate confined migration, the elimination of adhesions in HEMICA explains why migration was abrogated in β1-KD cells and raises the importance of integrins and focal adhesions in soft substrate confined migration.

To sum up, through HEMICA we revealed the essential roles of MIIA, integrin β1 and focal adhesions in soft substrate confined migration. We attributed the diminished role of MIIA in contracting the cell body and affecting cell speed in PDMS to the high polarization of pMLC. We justified the non-essential function of integrin β1 in influencing cell speed in PDMS to the maintenance of cell adhesions even when β1 was knocked-down and revealed the existence of focal adhesions all around the cell body in confined migration whose role is currently unknown.

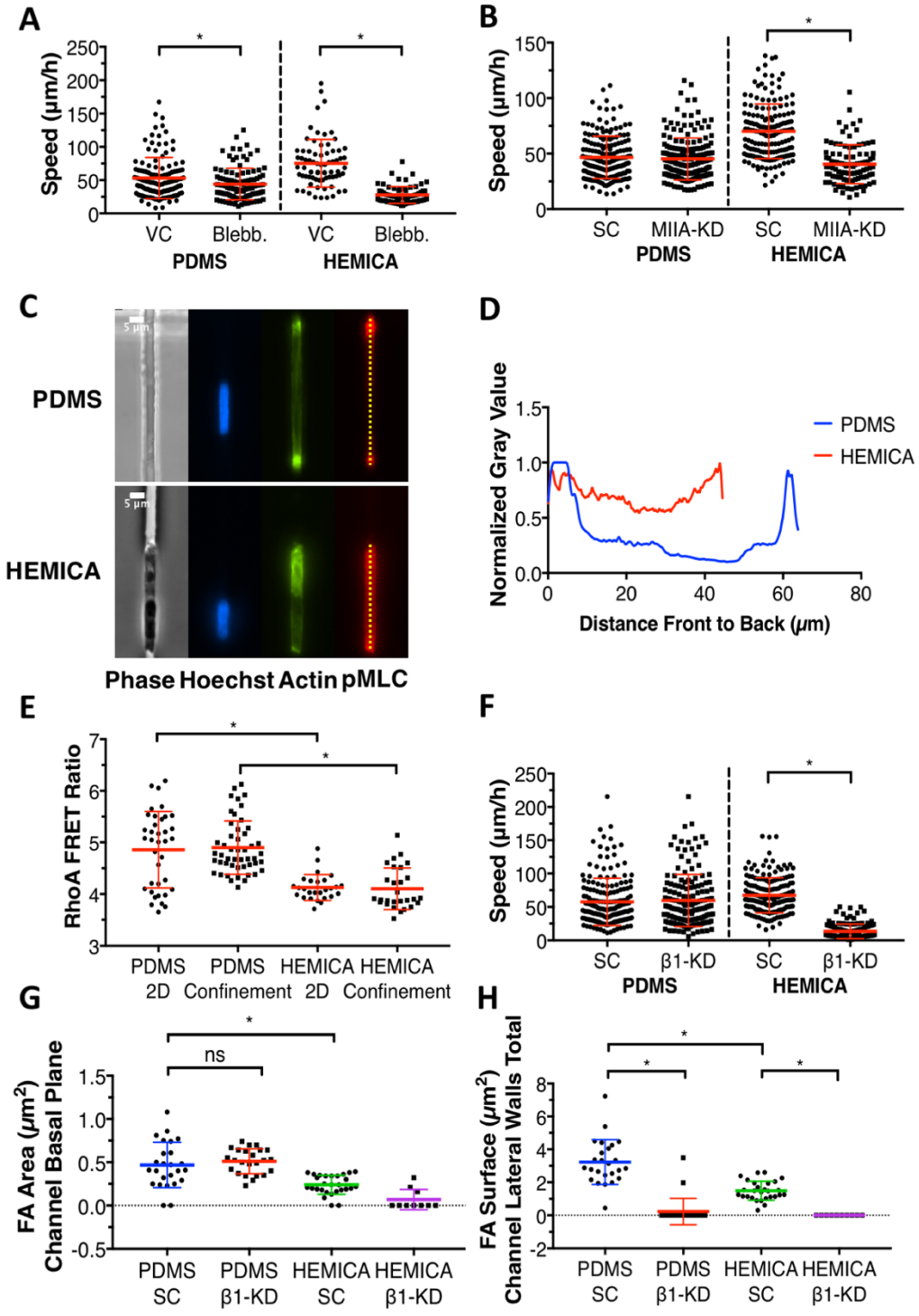

Figure 2-6. Myosin IIA-based contractility, integrin β1 and focal adhesions are critical for confined migration in HEMICA. (**A**) Confined migration speed of MDA-

MB-231 cells in PDMS and 26 kPa HEMICA under high dose blebbistatin (50 μM) treatment for contractility inhibition (n >= 109, 3 independent experiments were performed). Mann-Whitney (non-parametric) test was performed. (**B**) Confined migration speed of MDA-MB-231 MIIA-KD cells in PDMS and 26 kPa HEMICA (n >= 99, 3 independent experiments were performed). Mann-Whitney (non-parametric) test was performed. (**C**) Phase contrast and epifluorescence images of fixed and stained MDA-MB-231 cells in PDMS and 26 kPa HEMICA in confinement depicting nucleus (Hoechst), actin (phalloidin) and pMLC localization. Scale bar represents 5 μm. (**D**) Quantification of the pMLC fluorescence intensity line profile in PDMS and 26 kPa HEMICA of the previous epifluorescence image down the center of the cells. Intensity values were normalized to the maximum pixel intensity of each cell. (**E**) RhoA FRET ratios of MDA-MD-231 cells in PDMS and 26 kPa HEMICA on 2D and confined environments (n >= 28, 2 independent experiments were performed). ROUT method was used to identify 1% of outliers and Mann-Whitney (non-parametric) test was performed for statistical analysis. (**F**) Confined migration speed of MDA-MB-231 β1-KD cells in PDMS and 26 kPa HEMICA (n >= 138, 3 independent experiments were performed). Mann-Whitney (non-parametric) test was performed. (**G**) Focal adhesion area of MDA-MB-231 β1-KD paxillin-GFP cells on the basal plane of PDMS and 26 kPa HEMICA confining channels (n >= 10, > 3 independent experiments were performed). One-way non parametric ANOVA on ranks (Kruskal-Wallis test) was performed. (**H**) Focal adhesion surface of 3D reconstructed adhesions of MDA-MB-231 β1-KD paxillin-GFP cells on the lateral walls of PDMS and 26 kPa HEMICA confining channels (n >= 10, > 3 independent experiments were performed). One-way non

parametric ANOVA on ranks (Kruskal-Wallis test) was performed. Data represent the mean ± SD. * $p < 0.05$, ns: non-significant.

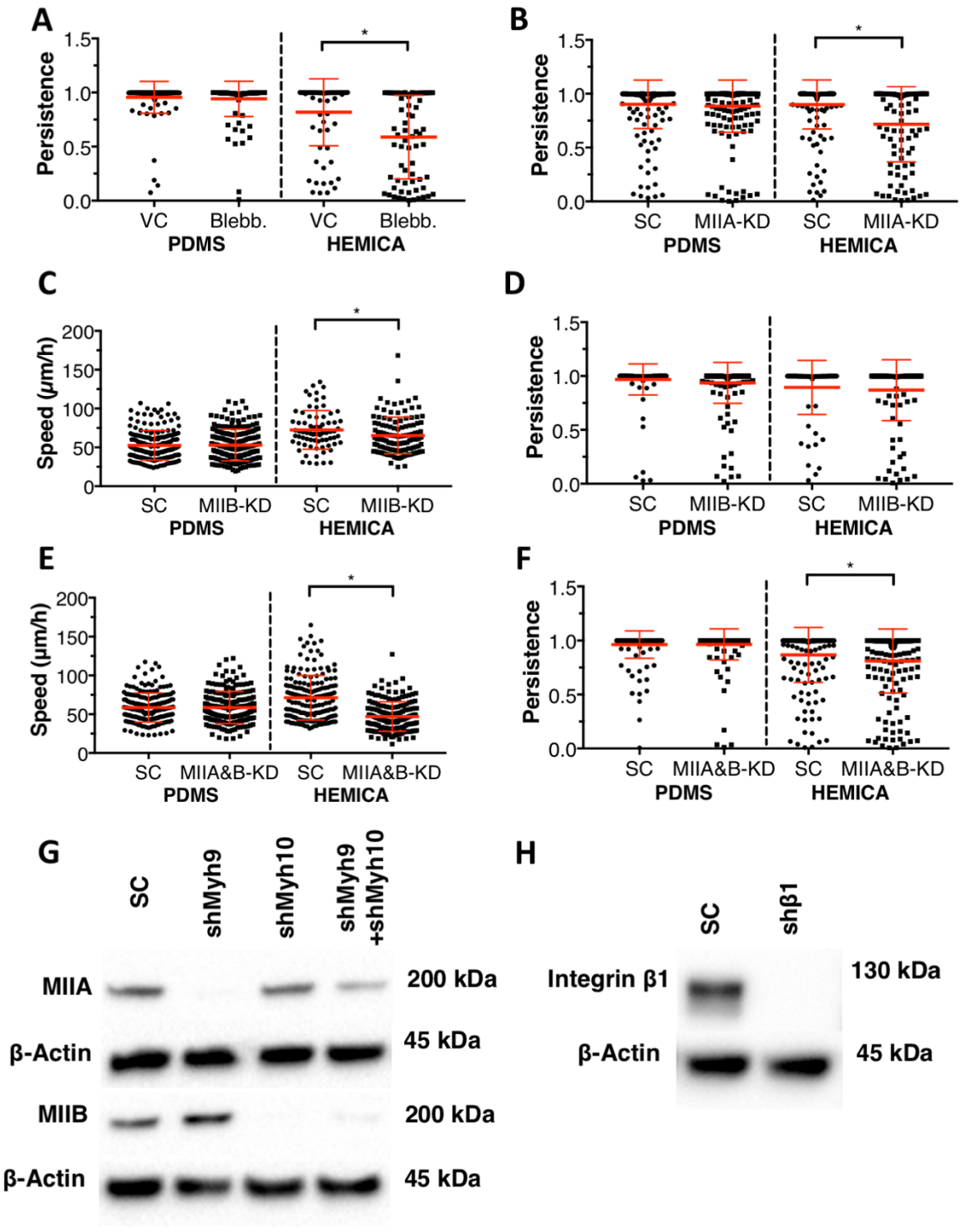

Figure 2-7. Contractility and integrin β1 regulate confined migration in soft substrates. (**A**) Confined migration persistence of MDA-MB-231 cells in PDMS and 26

kPa HEMICA under high dose blebbistatin (50 μM) treatment for contractility inhibition (n >= 109, 3 independent experiments were performed). Mann-Whitney (non-parametric) test was performed. (**B**) Confined migration persistence of MDA-MB-231 MIIA-KD cells in PDMS and 26 kPa HEMICA (n >= 99, 3 independent experiments were performed). Mann-Whitney (non-parametric) test was performed. (**C**) Confined migration speed of MDA-MB-231 MIIB-KD cells in PDMS and 26 kPa HEMICA (n >= 74, 3 independent experiments were performed). Mann-Whitney (non-parametric) test was performed. (**D**) Confined migration persistence of MDA-MB-231 MIIB-KD cells in PDMS and 26 kPa HEMICA (n >= 74, 3 independent experiments were performed). Mann-Whitney (non-parametric) test was performed. (**E**) Confined migration speed of MDA-MB-231 MIIA&B-KD cells in PDMS and 26 kPa HEMICA (n >= 171, 3 independent experiments were performed). Mann-Whitney (non-parametric) test was performed. (**F**) Western blots showing the knockdown efficiencies of shMIIA, shMIIB and shMIIA&B. β-Actin was used as housekeeping protein. (**H**) Western blot showing the knockdown efficiency of shβ1. β-Actin was used as housekeeping protein. Data represent the mean ± SD. * $p < 0.05$, ns: non-significant.

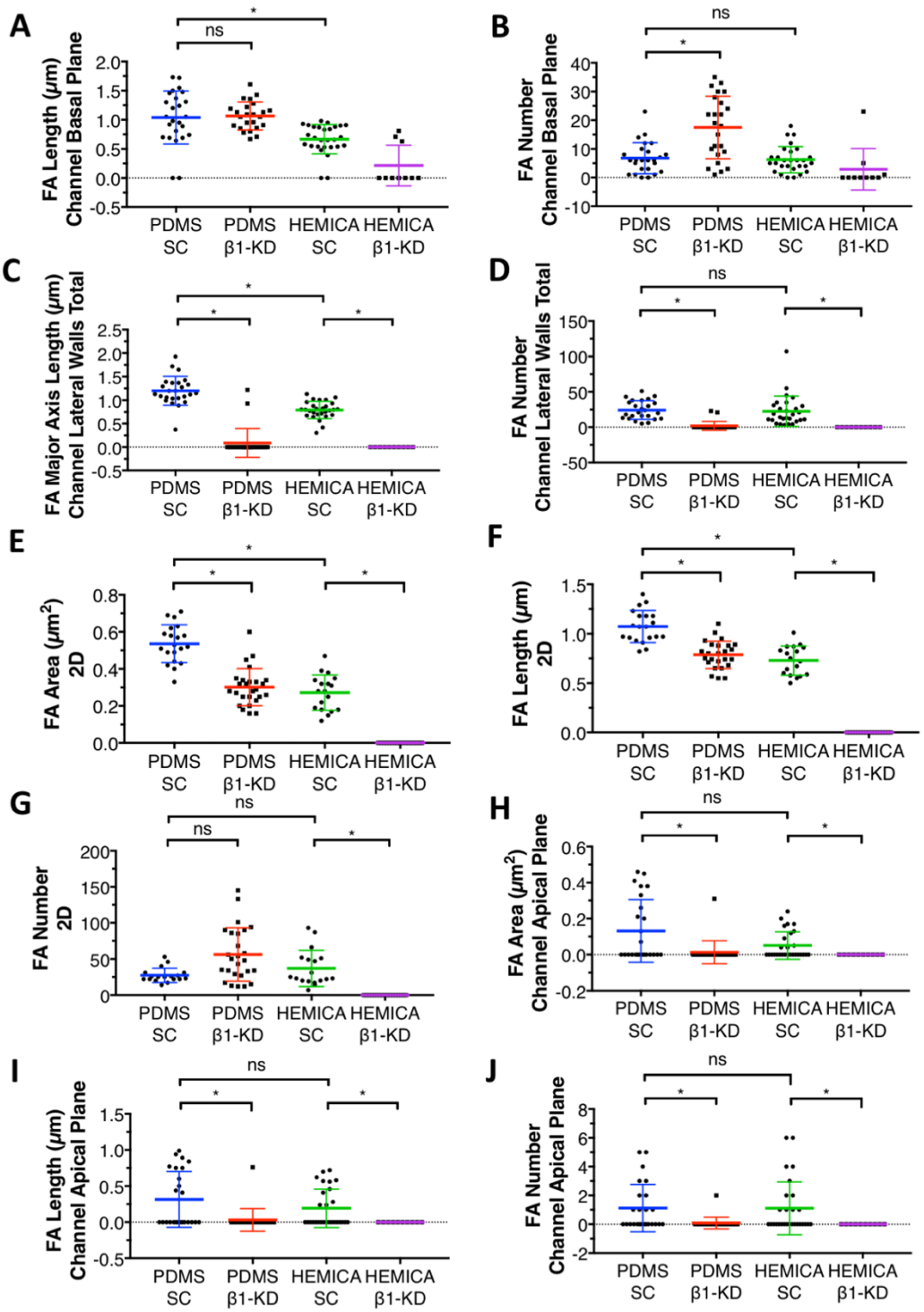

Figure 2-8. Quantification of focal adhesions in 3D. (**A**) Focal adhesion length, (**B**) Focal adhesion number of MDA-MB-231 β1-KD paxillin-GFP cells on the basal plane of PDMS

and 26 kPa HEMICA confining channels (n >= 10, > 3 independent experiments were performed). One-way non parametric ANOVA on ranks (Kruskal-Wallis test) was performed. (**C**) Focal adhesion major axis and (**D**) focal adhesion number of 3D reconstructed adhesions of MDA-MB-231 β1-KD paxillin-GFP cells on the lateral walls of PDMS and 26 kPa HEMICA confining channels (n >= 10, > 3 independent experiments were performed). One-way non parametric ANOVA on ranks (Kruskal-Wallis test) was performed. (**E**) Focal adhesion area, (**F**) focal adhesion length and (**G**) focal adhesion number of MDA-MB-231 β1-KD paxillin-GFP cells on the 2D seeding regions of PDMS and 26 kPa HEMICA (n >= 17, > 3 independent experiments were performed). ROUT method was used to identify 1% of outliers and one-way non parametric ANOVA on ranks (Kruskal-Wallis test) was performed. (**H**) Focal adhesion area, (**I**) focal adhesion length and (**J**) focal adhesion number of MDA-MB-231 β1-KD paxillin-GFP cells on the apical plane of PDMS and 26 kPa HEMICA (n >= 10, > 3 independent experiments were performed). One-way non parametric ANOVA on ranks (Kruskal-Wallis test) was performed. Data represent the mean ± SD. * $p < 0.05$, ns: non-significant.

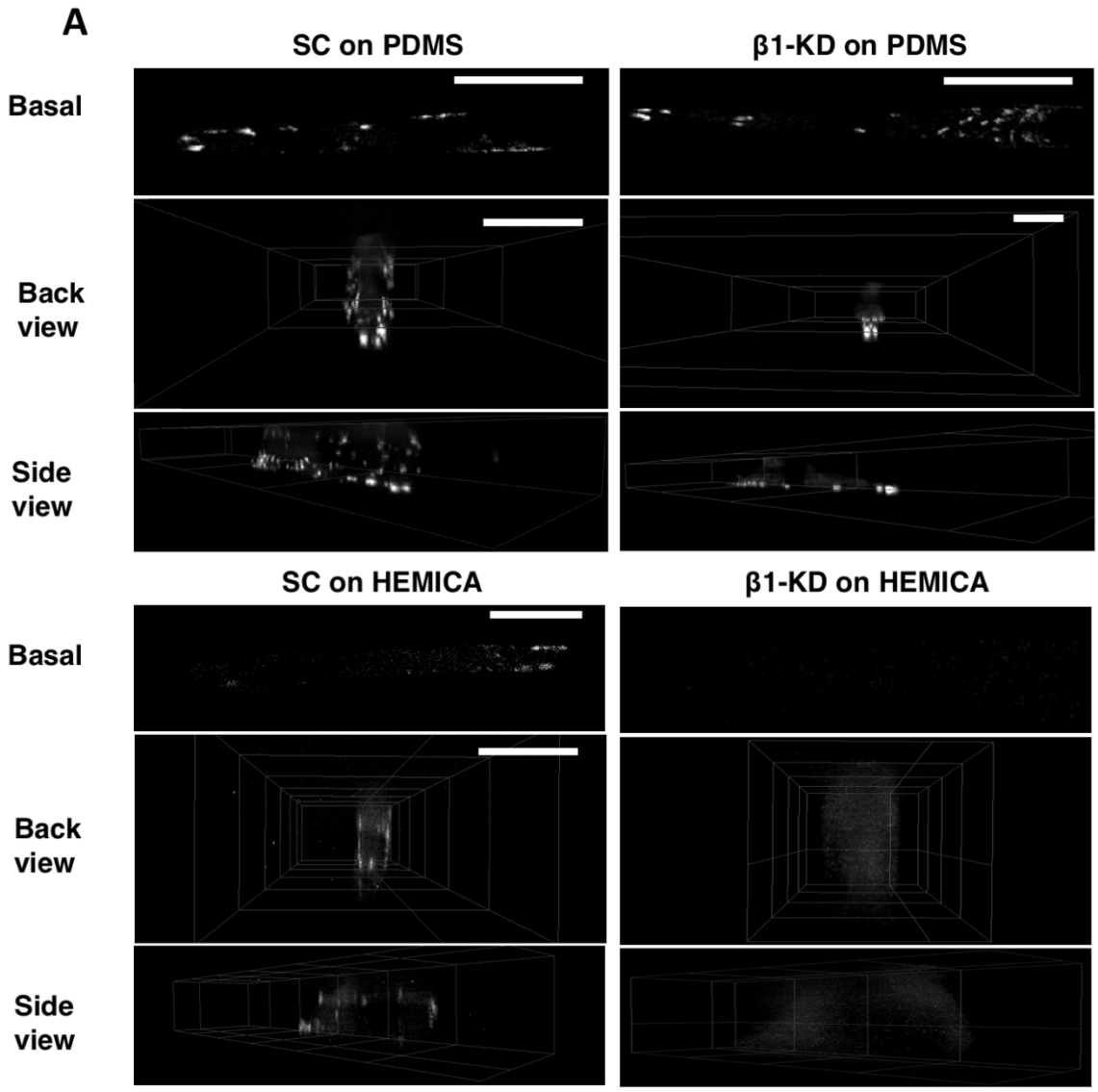

Figure 2-9. 3D reconstruction of focal adhesions in PDMS and HEMICA. (**A**) Images of focal adhesions of representative SC and β1-KD MDA-MB-231 paxillin-GFP cells in PDMS and 26 kPa HEMICA in confinement. Basal focal adhesions are shown as well as back and side views of background subtracted and 3D reconstructed 0.2 μm confocal z-stacks (60x lens). The original dimensions and zoom of the β1-KD images on HEMICA have been changed for better visualization of the background signal since adhesions are

absent. Scale bars represent 10 μm. Data represent the mean ± SD. * $p < 0.05$, ns: non-significant.

2.3.5 Experiments in HEMICA Bring to Light the Central Role of Actin and Call into Question the Effects of the Osmotic Engine Model in Confined Migration. Since confined migration in stiff PDMS substrates is characterized by a front-rear polarization of actin, we transduced MDA-MB-231 cells with LifeAct-GFP and measured F-actin flow in PDMS and compared it to soft 26 kPa HEMICAs. Two distinct patterns of actin flow were revealed; in PDMS actin retrograde flow was polarized with higher velocities on the front and rear of the cell while in HEMICA actin flow was more homogeneous throughout the cell with higher velocities around the cell center and lower at the poles (Fig. 2-10.A). Based on the Osmotic Engine Model (OEM), we know that in PDMS-based confined environments ions followed by water intake from the front of the cell and its outflux from the rear create a force that propels the cells forward (Stroka, Jiang et al. 2014). Since sodium hydrogen exchanger 1 (NHE1) was found to initiate the water intake, we generated NHE1 and aquaporin 5 (AQP5) knock-downs (Fig. 2-11.A, B) in order to investigate their role on confined migration in soft versus stiff substrates. As expected by the OEM model, our results showed that migration speed in both NHE1 and AQP5 knock-downs was inhibited to the same extent in PDMS and in HEMICA (Fig. 2-10.B, C). However, cell persistence was consistently slightly inhibited for both NHE1-KD and AQP5-KD in HEMICA (Fig. 2-11.C, D). Staining for NHE1, though, showed once more a definite polarization in PDMS (front-rear and at the edges of the nucleus) compared to HEMICA in which NHE1 was homogeneously spread throughout the cell body (Fig. 2-10.D, E). This discrepancy was reminiscent of the difference on the role of pMLC and contractility in PDMS compared to HEMICA. NHE1 is known to function as a plasma membrane anchor for actin filaments (Denker and Barber 2002) and aquaporins have been implicated in

promoting lamellipodium formation and stabilization of actin filaments (Loitto, Huang et al. 2007, Papadopoulos and Saadoun 2015). As such, we hypothesized that if the osmotic engine effects were present, then we would still observe migration when actin polymerization is inhibited with high doses of latrunculin A. Our experiments showed that in PDMS cell motility persisted under actin inhibition while on HEMICA migration was abolished (Fig. 2-10.G). As a result, NHE1 and AQP5 may affect confined cell motility in soft substrates yet the absence of NHE1 polarization does not allow for migration devoid of actin polymerization to take place, rendering the effects of the osmotic engine model unidentifiable.

In summary, our study of MDA-MB-231 cell migration in 26 kPa HEMICA revealed the central role of actin in confined cell migration on a physiologically relevant stiffness and uncovered the potential for a novel role of NHE1 and AQP5 in soft substrate confined migration. In PDMS, front-rear polarization of basic cytoskeletal or membrane elements diminished the importance of some (actin, MIIA) and added to the functionality of others (NHE1, AQP5), while in HEMICA all elements had to be in symphony with each other for cell motility to take place efficiently.

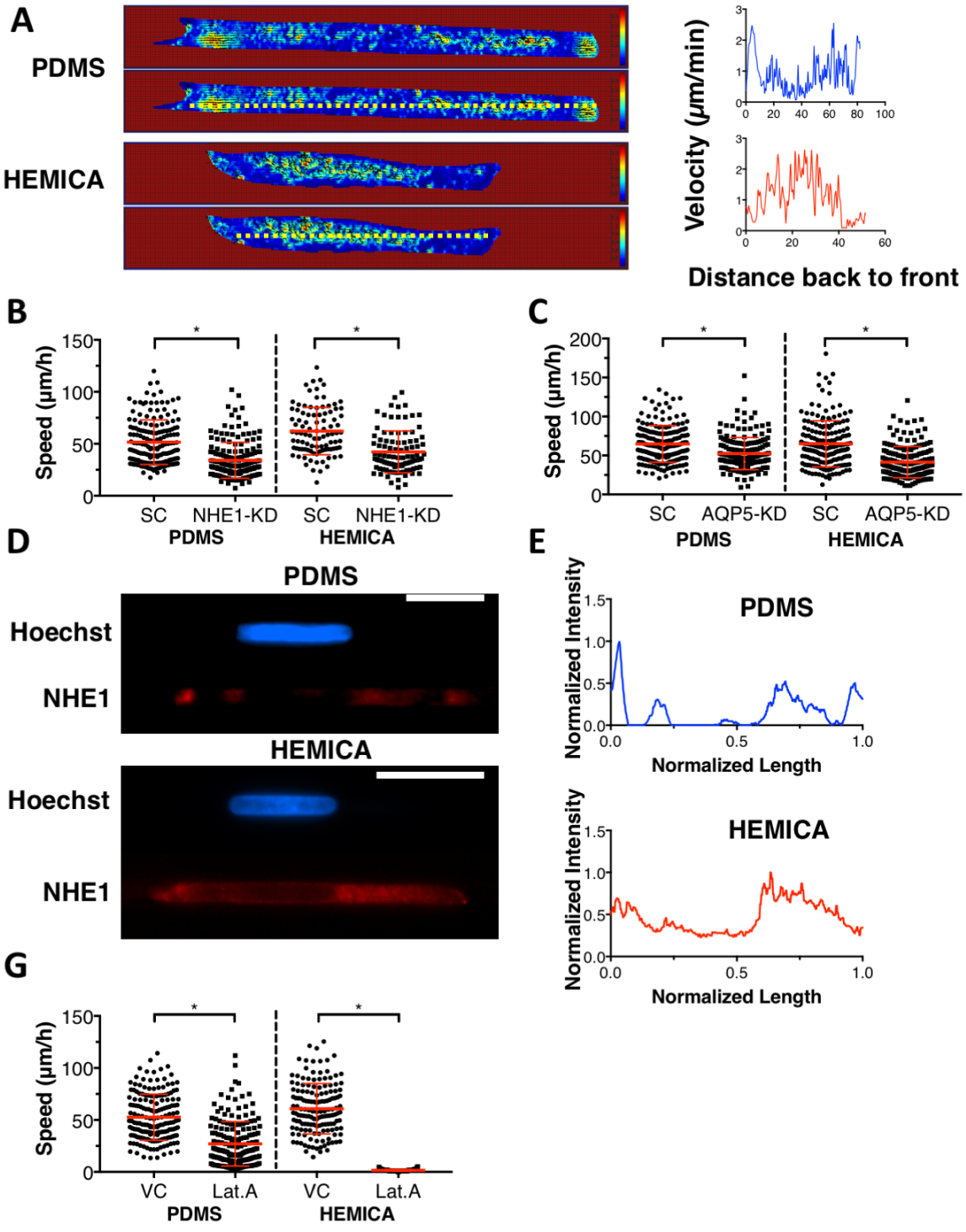

Figure 2-10. Soft substrate confined migration cannot proceed without actin. (**A**) Representative heat maps of confined migration actin flow of MDA-MB-231 LifeAct-GFP

cells in PDMS and 26 kPa HEMICA. Quantification of F-actin velocities. The yellow dotted lines denote the axis over which actin velocities were calculated. (**B**) Confined migration speed of MDA-MB-231 NHE1-KD cells in PDMS and 26 kPa HEMICA (n >= 96, 3 independent experiments were performed). Mann-Whitney (non-parametric) test was performed. (**C**) Confined migration speed of MDA-MB-231 AQP5-KD cells in PDMS and 26 kPa HEMICA (n >= 176, > 3 independent experiments were performed). Mann-Whitney (non-parametric) test was performed. (**D**) Representative epifluorescence images of the nucleus (Hoechst/blue) and NHE1 (red) of confined MDA-MB-231 cells in PDMS and 26 kPa HEMICA. Images were taken using a 20x lens. Scale bars represent 20 μm. (**E**) Quantification of the NHE1 fluorescence intensity of the previous representative images over a line that runs through the center of the cells from left to right. Values were normalized to the maximum pixel intensity of each cell. (**G**) Confined migration speed of MDA-MB-231 cells under 2 μM latrunculin treatment for actin inhibition in PDMS and 26 kPa HEMICA (n >= 150, 3 independent experiments were performed). Mann-Whitney (non-parametric) test was performed. Data represent the mean ± SD. * $p < 0.05$.

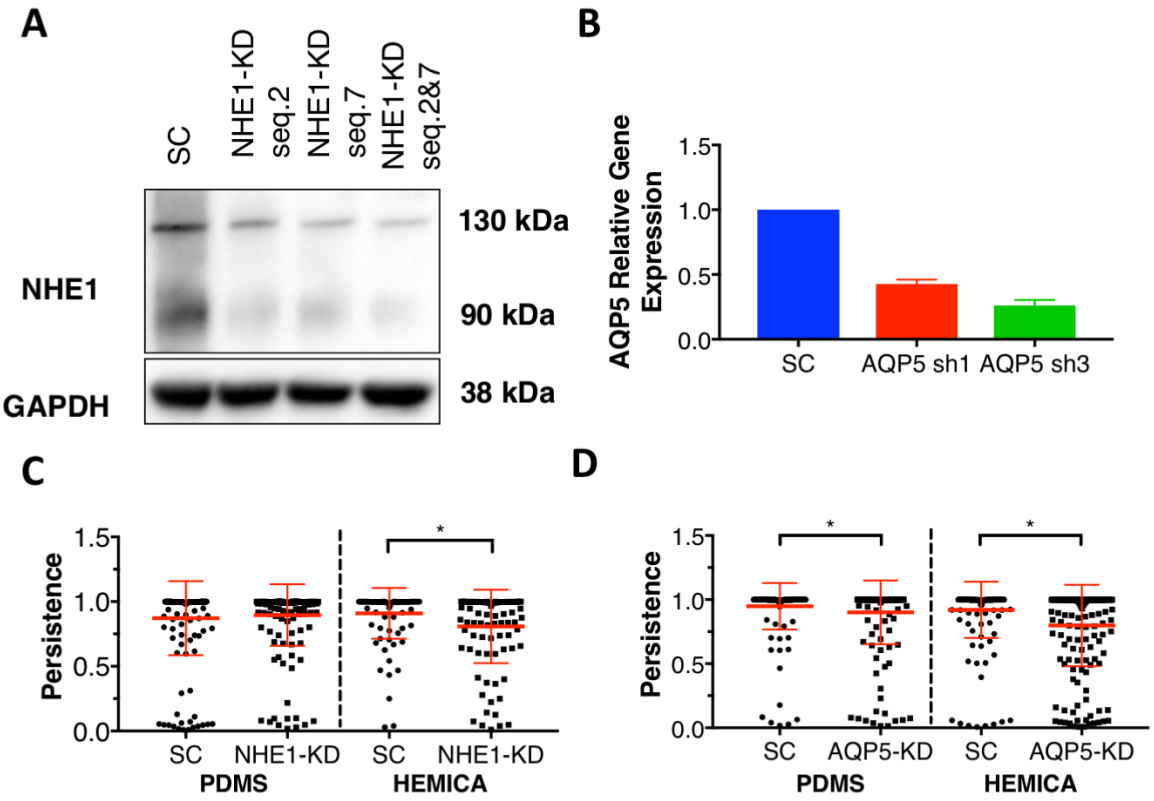

Figure 2-11. NHE1 and AQP5 channels are important for confined migration in soft substrates. (**A**) Western blot showing the knockdown efficiency of shNHE1. Two shRNA sequences (seq.2 and seq.7) were tested and the final NHE1-KD which was used for the experiments was produced using both of them since it resulted a better knock-down. Glyceraldehyde-3-phosphate dehydrogenase (GAPDH) was used as housekeeping protein. (**B**) qPCR showing the relative expression of AQP5 in cells transduced with two shRNA sequences (sh1, sh3). The cell line transduced with the lentivirus containing sh3 was used for the experiments. (**C**) Confined migration persistence of MDA-MB-231 NHE1-KD cells in PDMS and 26 kPa HEMICA (n >= 96, 3 independent experiments were performed). Mann-Whitney (non-parametric) test was performed. (**D**) Confined migration persistence

of MDA-MB-231 AQP5-KD cells in PDMS and 26 kPa HEMICA (n >= 176, > 3 independent experiments were performed). Mann-Whitney (non-parametric) test was performed. Data represent the mean ± SD. * $p < 0.05$.

2.3.6 Contractility Dependent Polarization of pMLC and NHE1 in Confined Cell Migration. Contractility has been suggested to have a critical role in substrate mechanosensing (Griffin, Sen et al. 2004, Discher, Janmey et al. 2005) and we have shown that RhoA, which affects stress fiber formation, stabilization of focal adhesions and contractility levels, is higher on 2D and confined MDA-MB-231 cells on stiff substrates (glass/PDMS) than on softer 26 kPa HEMICAs. Consequently, we hypothesized that the lower, physiological stiffness of HEMICAs leads to a RhoA decrease which subsequently facilitates the depolarization of actin, pMLC and NHE1. In short, we attempted to make cells in PDMS respond and function as cells in HEMICA. In order to emulate the lower contractility environment in HEMICA we treated confined cells in PDMS with a low dose of blebbistatin. Speed measurements showed a significant increase in cell speed which reached values even higher than the ones observed in W = 3 μm 26 kPa HEMICA (Fig. 2-12.A). In addition, MDA-MB-231 cells transduced with paxillin-GFP under low blebbistatin treatment showed a minor reduction of the size of basal focal adhesions (Fig. 2-12.B) and a significant reduction on the number of adhesions (Fig. 2-12.C). Actin flow measurements under low blebbistatin treatment indicated a loss of actin retrograde flow polarization with a more homogeneous flow throughout the cell body similar to 26 kPa HEMICA measurements (Fig. 2-12.D). Actin staining, also, revealed the loss of actin polarization under low blebbistatin (Fig. 2-12.E). Furthermore, staining for pMLC and NHE1 under minor reduction of contractility led to a loss of their front-rear polarization (Fig. 2-12.F). Finally, by adding a high dose of latrunculin A in addition to the low dose of blebbistatin we managed to achieve almost complete abrogation of migration in PDMS, the same way we abolish motility in HEMICA (Fig. 2-12.G).

In summary, by minimally reducing cell contractility in PDMS, in order to replicate the cellular conditions in HEMICA, we achieved higher speeds, less adhesions, reversal of actin flow, NHE1 and pMLC polarization, and functionally we abrogated migration with inhibition of actin.

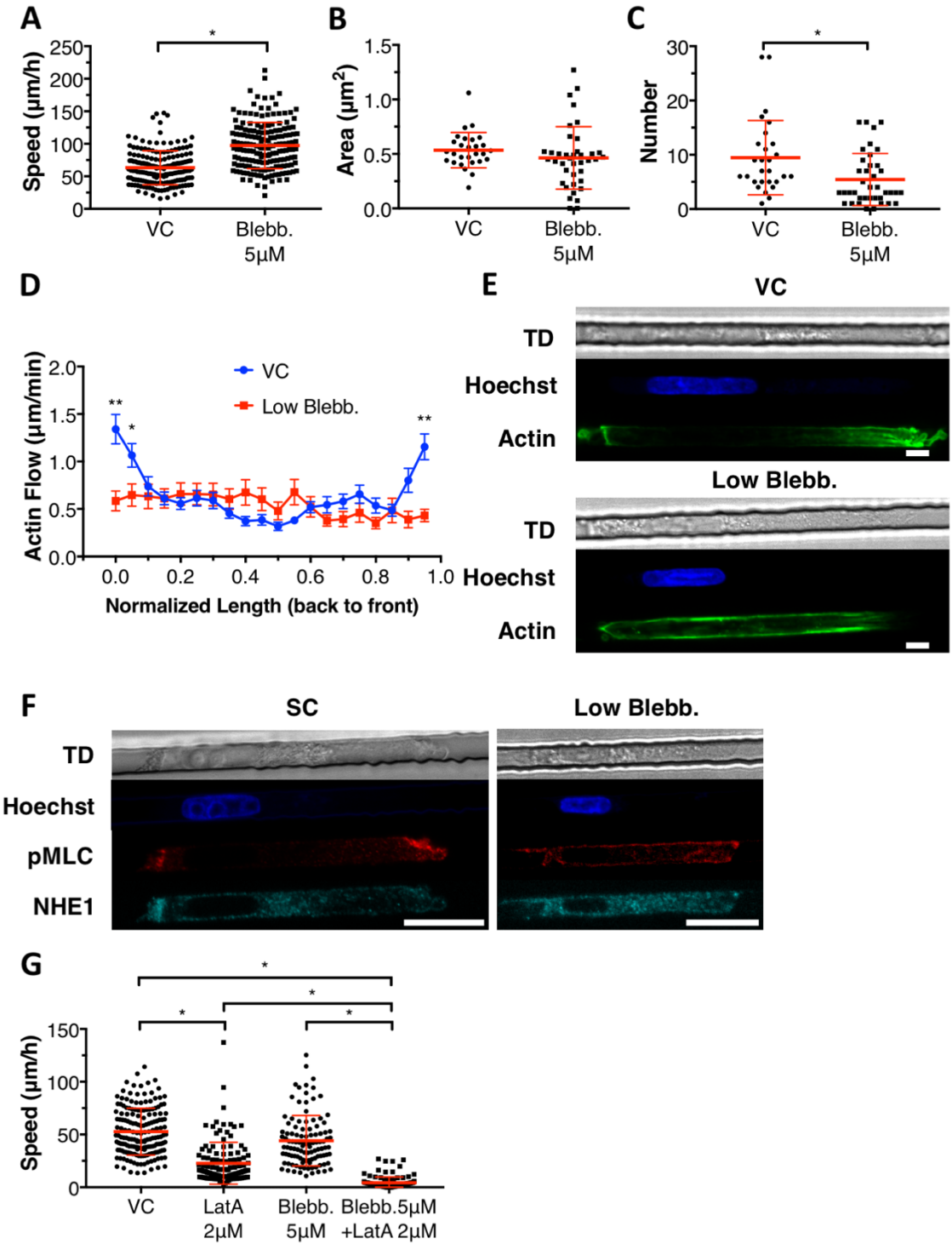

Figure 2-12. Myosin facilitates pMLC and NHE1 polarization. (**A**) Confined migration speed of MDA-MB-231 cells in PDMS and 26 kPa HEMICA under low dose of

blebbistatin (5 μM) treatment for partial contractility inhibition (n = 174, 3 independent experiments were performed). Mann-Whitney (non-parametric) test was performed. (**B**) Basal plane focal adhesion area and (**C**) basal plane focal adhesion number of MDA-MB-231 paxillin-GFP cells under low blebbistatin (5 μM) treatment in PDMS confining channels (n >= 28, 2 independent experiments were performed). Mann-Whitney (non-parametric) test was performed. (**D**) Quantification of F-actin velocities of MDA-MB-231 LifeAct-GFP cells in PDMS under low blebbistatin (5 μM) treatment. Velocity profiles were acquired over a line at the center of the cells from back to front. Cell lengths were normalized to the maximum length of each cell. Velocity values of n >= 19 cells were averaged for every 5% normalized length segments (data pulled from 3 independent experiments). 2-way ANOVA was performed. * $p < 0.05$, ** $p < 0.0005$. Velocity values were compared between vehicle control (VC) and low blebbistatin treatment for the same segment of normalized length. Data represent the mean ± S.E.M. (**E**) Confocal (60x lens), transmitted light (TD) and fluorescence images of fixed and stained MDA-MB-231 cells in confinement under low blebbistatin treatment in PDMS. Nucleus (Hoechst/blue), actin (green). Scale bar represents 3 μm. (**F**) Confocal (60x lens), transmitted light and fluorescence images of fixed and stained MDA-MB-231 cells in confinement under low blebbistatin treatment in PDMS. Nucleus (Hoechst/blue), pMLC (red), NHE1 (cyan). Scale bar represents 20 μm. (**G**) Confined migration speed of MDA-MB-231 cells in PDMS under high dose latrunculin A (2 μM), low dose of blebbistatin (5 μM) and combined treatment (n >= 109, 3 independent experiments were performed). One-way non parametric ANOVA on ranks (Kruskal-Wallis test) was performed. Data represent the mean ± SD. * $p < 0.0005$.

2.4 Discussion

Multiple in-vitro devices attempt to recreate micro-topographies which are found in-vivo while controlling the stiffness, dimensions, protein concentrations and water/small molecule permeation. These devices include the use of materials such as PA, ECM proteins or PDMS. The existence of open micro-tracks in-vivo through which cells migrate with or without proteolytic degradation of the ECM has inspired researchers to use either soft lithography in order to generate those microchannels and then imprint them on the material of their choice or use two-photon microscopy to create those tracks on 3D gels. These efforts, however, have led to devices which are either not confining the cells from all sides (Pathak and Kumar 2012), creating vertical compression on the cells (Liu, Le Berre et al. 2015), confining the cells on 1D (Junkin and Wong 2011), capping the microchannels with a layer of gel without proper bonding between the top and the bottom gel (Kraning-Rush, Carey et al. 2013), using PDMS/glass which are not liquid permeable and exhibit stiffnesses over 1000kPa (Balzer, Tong et al. 2012) or using expensive/scarce techniques such as two-photon microscopy for creating microchannels in 3D which do not allow high throughput experiments (DeForest and Anseth 2011).

With HEMICA, not only do we present a tool which is affordable, built with already established techniques and materials, properly confining cells from all directions, allowing for chemotactic gradients, stiffness anisotropy, collective and single-cell file migration, TFM, immunofluorescence, live-microscopy, confocal microscopy, FRET, high aspect ratio micro-fluidic features and high cell throughput, but also we establish a gel-to-gel bonding protocol based on primary amines which can be applied beyond polyacrylamide to any other material that contains them. As such, HEMICA can be used for studying

single-cell behavior, cell-cell communication, cell-matrix interactions and cell population dynamics. The unique, highly controlled and physiologically relevant mircro-environment generated in HEMICA, also, permits its usage in organ-on-a-chip applications.

On the other hand, HEMICA has certain limitations. Imprinting microchannels smaller than 3 μm would be an issue in really soft gels with Young's modulus less than 10kPa. Handling gels of low Young's modulus will require special attention. Chemical or osmotic gradients that last longer than 15 hours may be difficult to achieve unless the volume of the gel is tweaked. Finally, really stiff gels (Young's modulus >=100kPa) won't be able to seal properly unless a longer NHS-ester ligand is used, since both gel surfaces that are about to be bonded together won't come to a sufficient distance from one another.

Cell migration in 3D occurs via either proteolytic degradation and rearrangement of the ECM or via migration through pre-established open micro-tracks. In general, 3D migration implicates cell-matrix adhesions, RhoA, ROCK and myosin II for mechanotransduction which in turn can govern the mode of migration (Petrie and Yamada 2012). Cancer cells with a round morphology may exhibit high contractility with low adhesions and integrin clustering, moving in an amoeboidal blebbing manner (Lammermann, Bader et al. 2008, Deakin and Turner 2011, Lorentzen, Bamber et al. 2011), while more mesenchymal cells with lower levels of RhoA, ROCK or myosin II are dependent upon contractility and β1 integrins for fast migration (Carragher, Walker et al. 2006, Doyle, Wang et al. 2009, Petrie, Gavara et al. 2012). In addition, reorganization of the actin cytoskeleton and local actin polymerization is essential for the creation of lamellipodia, podosomes and invadopodia which are needed for driving cell migration and invasion (Yamaguchi and Condeelis 2007). On the other hand, confined cell migration

through PDMS-based open tracks does not necessarily need myosin contractility in order to occur (Hawkins, Piel et al. 2009). The role of β1 integrin is suppressed in breast mesenchymal-like MDA-MB-231 and pancreatic epithelial Pa03C cells (Balzer, Tong et al. 2012), actin is dispensable for cell motility to proceed once the cells are polarized within the confining microchannels, and forces through water permeation are able to drive migration (Stroka, Jiang et al. 2014).

However, by using HEMICA and studying confined migration in physiologically relevant stiffnesses, we found that motility in confining spaces shares more characteristics with 3D migration. Migration of MDA-MB-231 cells is affected significantly by MIIA-based contractility and pMLC is found throughout the cell body. Since cells in HEMICA are also able to perturb the compliant walls of the microchannel, it is reasonable to suggest that confined migration in soft substrates occurs similarly to metastatic adenocarcinoma MTLn3E cells in a collagen matrix as described by (Wyckoff, Pinner et al. 2006) where a ROCK-dependent regulation of MLC generates enough pushing force that deforms the ECM and allows migration. In addition, cell-pressure induced tissue compression as we observed via our TFM experiments, has also been witnessed by (Ilina, Bakker et al. 2011) where mammary tumor (MMT) breast cancer cells in a 3D collagen gel expand preformed tracks by a MMP-independent pushing mechanism. This tumor induced pressure on the ECM (Netti, Berk et al. 2000) may lead to condensation of the ECM structure (Egeblad, Nakasone et al. 2010) and act as a barrier for drug delivery and macromolecule transport (Pluen, Boucher et al. 2001).

The integrin β1-dependent mode of confined migration of MDA-MB-231 cells in HEMICA contrasts with the β1-independent migration in PDMS. Maintenance of basal

paxillin-rich adhesions in PDMS after integrin β1 knockdown suggests a high degree of plasticity which may enable cells to mobilize a different set of integrins such as $\alpha_v\beta_3$ which is found in stiff matrices (Jones and Ehrlich 2011, Zhao, Li et al. 2014) in order to maintain the same cell speed. The existence of apicolateral paxillin-rich adhesions, though, and loss thereof after β1 knockdown implies a different mode of migration and a secondary role of non-basal adhesions in stiff substrate confined migration. On 2D polyacrylamide gels coated with collagen I, mouse embryonic fibroblasts (MEFs) and human fibrosarcoma HT-1080 cells display a biphasic relationship between cell speed and mean focal adhesion size (Kim and Wirtz 2013). Knowing that stiffer substrates regulate the phosphorylation of multiple proteins involved in focal adhesions such as FAK and paxillin (Pelham and Wang 1997, Wozniak, Desai et al. 2003) and thus adhesions in stiff substrates are more stable than in soft ones (Discher, Janmey et al. 2005), the reduction of the total number and size of paxillin rich adhesions in soft substrate confined migration of mesenchymal-like cells explains why cells move faster than in stiff PDMS.

Although actin has been shown to polarize towards the rear of cells by creating a higher retrograde actin flow at the cell center thus propelling them forward under vertical confinement in A2 migrating cells and low adhesion regimes (Liu, Le Berre et al. 2015), our findings through HEMICA in full confining soft environments show that actin is not polarized yet actin flow is more homogeneous through most of the cell with higher velocities towards the cell center and lower on the front and rear. Actin and actin flow polarization are observed in stiff PDMS confining microchannels. Under the same conditions, NHE1 assumes a front-rear polarization which supports osmotic engine propulsion forces yet in HEMICA neither NHE1 polarization nor its effects are observed

under actin inhibition. While NHE1-KD and AQP5-KD reduce the speed of confined migration, their mechanism is yet to be determined for soft substrate confined migration.

Our results suggest that lower adhesion regimes, just like the ones encountered in physiological stiffness HEMICAs, increase the dependence of mesenchymal-like cell migration on actin, myosin II and β1 integrins due to the smaller adhesions and lower RhoA levels. Conversely, via low dose blebbistatin treatment in PDMS which lowers myosin II-based contractility and focal adhesion number we reverse the initial polarization of actin, actin flow, pMLC and NHE1 and abrogate migration via latrunculin treatment. As such, cells in PDMS can be manipulated to behave like in HEMICA and myosin II appears to be involved in the polarization of cytoskeletal and membranous proteins. Evidence of MLC polarization on the dorsal dome of invading cells (Estecha, Sanchez-Martin et al. 2009) and NHE1 polarization at the front of invadopodia (Beaty, Wang et al. 2014) with an increased Rho-ROCK signaling promoting tumor invasion (Sahai and Marshall 2003), and elevated Rho levels aiding mitosis (Narumiya and Yasuda 2006) which is regulated by volume-regulated anion channels (VRACs) (Pedersen, Hoffmann et al. 2013), support the hypothesis that Rho or myosin II signaling facilitate pMLC and ion channel polarization in various processes.

Chapter 3

MYOSIN IIA AND TRPM7 CHANNEL SENSE HYDRAULIC RESISTANCE AND DICTATE DECISION-MAKING

3.1 Introduction

Cells employ various biochemical machinery in order to navigate efficiently through the extracellular matrix (ECM). The dimensions of pre-established migration tracks through the body confine cells in 3D and affect drastically their migratory behavior. Directional dilemmas imposed by intersections of these tracks present a new challenge for deciphering the migratory behavior of cells (Pathak and Kumar 2012, Hung, Chen et al. 2013, Lautscham, Kammerer et al. 2015, Paul, Shea et al. 2016). Choosing one direction over another relies on sensing and interpreting chemical and stiffness gradients which ultimately govern the cell decision-making process. (Ambravaneswaran, Wong et al. 2010, Pathak and Kumar 2012, Plotnikov, Pasapera et al. 2012, Scherber, Aranyosi et al. 2012). In addition, various bodily liquids such as the blood and the interstitial fluid can exert additional resisting forces on cells in confined micro-environments, thus rendering the hydraulic resistance a major contributor in cell decision-making. (Fuerstman, Lai et al. 2007, Ioannis K. Zervantonakis 2010, Harrison V. Prentice-Motta 2013, Bergert, Erzberger et al. 2015). In response to the external pressure, a population of neutrophils has a higher probability in choosing the directional track with lower hydraulic resistance (Ambravaneswaran, Wong et al. 2010, Harrison V. Prentice-Motta 2013). Combinations

of bifurcated channels of different dimensions present different patterns of cell entry (Harrison V. Prentice-Motta 2013, Mak and Erickson 2014, Paul, Shea et al. 2016). However, it is unclear how hydraulic resistance results into cells exhibiting these decision-making patterns, which are practically probability distributions of cells entering and navigating through set arrays of channel branches. The relationship between hydraulic resistance, cell mechanosensing and cell decision-making is yet to be shown.

For cell entry and migration inside channel branches, the hydraulic resistance or the resulting pressure drop to their leading edge has to be physically balanced (Sims, Karp et al. 1992, Chicurel, Chen et al. 1998, Lammermann and Sixt 2009, Lieber, Yehudai-Resheff et al. 2013). External forces are counteracted by the cell membrane and the cytoskeleton which act as physical scaffolds. The rigid actomyosin network, which is connected to the lipid bilayer through the membrane-to-cortex-attachment (MCA), provides the majority of membrane tension. (Diz-Munoz, Krieg et al. 2010, Salbreux, Charras et al. 2012, Diz-Munoz, Fletcher et al. 2013). Contractile forces generated by cortical actomyosin create high local hydrostatic pressures which can be sustained for relatively long time scales before propagating throughout the rest of the cell (Charras, Yarrow et al. 2005). The interplay between the competing forces/pressures across the cell membrane is suspected to result in blebbing instability and membrane stretching which in turn leads to mechanosensing (Lee and Liu 2015, On Shun Pak 2015).

Apart from the cortical actomyosin networks, studies on mechanosensitive ion channels have raised their importance in various cell functions (Clark, Middelbeek et al. 2008, Dhennin-Duthille, Gautier et al. 2011, Prevarskaya, Skryma et al. 2011, Ouadid-Ahidouch, Dhennin-Duthille et al. 2013). In particular, from the transient receptor potential

channel (TRP) family, which is present in numerous cancer cells, TRPM7 coupled with calcium signaling has been implicated to direct 2D migration (Krapivinsky, Mochida et al. 2006, Petrie, Doyle et al. 2009, Wei, Wang et al. 2009). In addition, calcium plays an important role in several other cell functions which are important for migration such as cytoskeletal remodeling, traction force transmission and focal adhesion turnover. (Ridley, Schwartz et al. 2003, Wei, Wang et al. 2009, Chen, Hung et al. 2013, Monteith, Prevarskaya et al. 2017). However, molecular signaling and intracellular remodeling are still not tied to cell decisions in confinement in a concise manner.

Here we investigate the dynamics of migrating cells during their decision-making process in trifurcated microchannel intersections across a large range of hydraulic resistances. Through a systematic study we characterize the decision-making process and split it into three phases: the exploratory, the cell entering and the post nuclear entrance phase. We identify the cell decision-making time point based on the growth of cell protrusions and explain the roles of cortical actin and myosin in affecting the time course of cell decisions or the actual decisions made. We single out TRPM7 channels and myosin as the main mechanosensors of hydraulic resistance, relate hydraulic resistance to the levels of actin and myosin, and raise the importance of calcium signaling in confined cell decision-making.

3.2 Materials and Methods

3.2.1 Cell culture and pharmacological inhibitors. Human MDA-MB-231 adenocarcinoma and HT-1080 fibrosarcoma cells were cultured in Dulbecco's Modified Eagle Medium (DMEM) containing 4.5 g/L glucose, L-glutamine, and sodium pyruvate

(Gibco) and supplemented with 10% heat inactivated fetal bovine serum (Gibco) and 1% penicillin/streptomycin (10,000 U/mL, Gibco). Cells were grown in an incubator maintained at 37 ºC and 5% CO_2, and passaged every 2-4 days.

In selected experiments, cells were treated with pharmacological agents and corresponding vehicle controls as follows: Y-27632 (10 μM), blebbistatin (50 μM), colchicine (125 μM), CK666 (100 μM), latrunculin A (2 μM), 2-APB (100 μM), bapta-AM (25 μM), GsMTx4 (20 μM), SKF 96365 (10 μM), FTY720 (2 μM), HC 067047 (5 μM).

3.2.2 Cloning, lentivirus preparation and transduction. Target sequences were subcloned into pLVTHM (gift from Didier Trono, Addgene, Cambridge, MA, plasmid # 12247) using MluI and ClaI as restriction sites, or pLKO.1 (gift from Bob Weinberg, Addgene, Cambridge, MA, plasmid #8453) using AgeI and EcoRI as restriction sites. The target sequences are:

Scramble Control: sh1 (GCACTACCAGAGCTAACTCAGATAGTACT),

human MYH9 (ACGGAGATGGAGGACCTTATG),

human MYH10 (GGATCGCTACTATTCAGGA),

human DIA1 sh1 (GCATGCCCTATCAAGAGATTA)

human DIA1 sh3 (GCCGCTGCTGGATGGATTAAA)

The pLenti.PGK.LifeAct-GFP.W (gift from Rusty Lansford, plasmid # 51010), pLenti.PGK.H2B-mCherry (gift from Rusty Lansford, plasmid # 51007), pLenti.PGK.LifeAct-Ruby.W (gift from Rusty Lansford, plasmid #51009) were purchased from Addgene.

For lentivirus production, 293T/17 cells were co-transfected with psPAX2, pMD2.G and the lentiviral plasmid. Lentivirus was harvested and purified after 48h transfection via centrifugation (50,000 g for 2 h at 4 ºC). Subsequently, cells were transduced for 24 h with media containing lentiviral particles.

For transient transfections, 60-80% confluent MDA-MB-231 cells were transfected using Lipofectamine 3000 reagent using manufacturer's recommendations. MYH9-GFP was introduced into MDA-MB-231 cells by transfection and placed under G418 selection before sorting.

3.2.2 Immunofluorescence. Cells in micro-channels were fixed with 4% paraformaldehyde (Affymetrix, Inc.), permeabilized in 0.1% Triton X-100 (Sigma), and blocked in 1% bovine serum albumin. Cells were stained with Alexa Fluor 488 phalloidin (1:100, Invitrogen), Hoechst (1:2500, Invitrogen) and anti-phospho-MLC (1:50, Cell Signaling), with corresponding secondary antibodies.

3.2.3 Photolithography and Device Fabrication. Polydimethylsiloxane (PDMS)-based microfluidic devices consisting of an array of a parallel decision-making channel maze were fabricated as described previously (Balzer et al., 2012). A 200 μm in length straight channel, with a height, H, of 3 μm and a width, W, of 10 μm, was introduced for cell to migrate before encountering the three-way intersection. The three-way intersection contained a 3 μm × 10 μm × 320 μm (H × W × L) channel on the left, a 3 μm × 10 μm × 200 μm (H × W × L) channel straight and 3 μm × 20 μm × 2240 μm (H × W × L) channel on the right. A second design was also applied as the dimensions of the sub-channel

on the right were adjusted to $3\,\mu$m × $20\,\mu$m × $320\,\mu$m (H × W × L) whereas the rest were kept the same. The dimensions were verified using a laser profilometer. In decision-making experiments, channels were coated with 20 μg/mL collagen I (Collagen I Rat Protein, Tail, Thermo Fisher Scientific) for all cases.

3.2.4 Microfluidic Device Seeding and Live Cell Imaging. Cells were collected from culture dishes using 0.25% trypsin-EDTA (Gibco), followed by 5 min centrifuge at 300 g and re-suspended in DMEM (1% penicillin/streptomycin and 10% FBS) to a concentration of 5 x 10^6 cells/mL. 20 μL of cell suspension were added to the device inlet, generating a pressure gradient for cell to enter the device. The pressure was then balanced by transferring 7-8 μL of cell suspension from the inlet to the outlet. Cells were allowed to adhere and spread outside of the channel entrances for 20-40 min. All wells of the device were then filled with 120 μL DMEM (plus 10% FBS, 1% penicillin/streptomycin). Devices were incubated at 37 ºC, 5% CO_2 prior to imaging.

Cells were imaged for every 10 min for at least 20 h on an inverted Nikon Eclipse Ti microscope (Nikon, Tokyo, Japan) with automated controls (NIS-Elements; Nikon) and a 10x/0.45 numerical aperture Ph1 objective using time-lapse microscopy. During the experiments, cells were maintained on a stage top incubator (Okolab, Pozzuoli, Italy or Tokai Hit, Shizuoka-hen, Japan) at 37 ºC and 5% CO_2. For selected experiments, FITC and TRITC filters were used to excite cell fluorescence.

3.2.5 Decision-Making Analysis. For decision-making tracking, a successful decision was acknowledged when the nucleus, and at least 90% of the volume of the cell, entered one

sub-channel from the three-way intersection. Live cell videos were exported to ImageJ (National Institute of Health, Bethesda, Maryland) for protrusion dynamics measurements and to a custom-made MATLAB (MathWorks, Natick MA) script for cell migration behavior analysis. Decision-making time was determined from the first contact of the cell to the intersection to when a successful decision was made.

For migration phenotype classification, cells were examined with an inverted Nikon Eclipse Ti microscope (Nikon, Tokyo, Japan) using a 40X air objective. Cell migration phenotype and nuclear blebbing were tabulated manually.

3.2.6 Calcium Assay. The calcium assay was performed using Fluo-4 Direct Calcium Assay Kits (Invitrogen, F10471). Cells were cultured in 6-well plates and were used at near confluence the next day. The solutions were prepared as described by the manufacturers' protocol. A 0.4X reagent, 250 μL reagent in 1 mL media, was applied for loading. The cells were then incubated at 37 ºC and 5% CO_2 for 45 min and then at room temperature for 15 min. After that, the cells were collected and seeded into the device for imaging as demonstrated above.

3.2.7 Confocal Imaging. Cells were imaged using a Nikon A1 confocal microscope (Nikon, Tokyo, Japan) with a 63X oil objective. Actin or calcium intensity was processed manually using ImageJ and quantified by custom-made MATLAB scripts.

3.2.8 CRISPR-Cas9-mediated knockout of TRPM7. CRISPR-Cas9-mediated knockout was performed using the methodology presented before (Ran, Hsu et al. 2013). The short

guide RNA (sgRNA) sequence (5'-AAATTTGTCAGCAACTCGTC-3') from the GeCKO library (Shalem, Sanjana et al. 2014) was cloned into the BbsI restriction site of the SpCas9-2A-Puro V2.0 vector, which was a gift from Feng Zhang (Addgene #62988). MDA-MB-231 cells were transiently transfected with the sgRNA-plasmid, grown for 48h, and selected with puromycin. Surviving cells were plated as single cell colonies in a 96-well plate (1 cell/well) and expanded. Knock-out of TRPM7 in expanded cells was confirmed by western blotting with an anti-TRPM7 antibody (clone N74/25, Abcam).

3.2.9 Western Blotting. Western blots were performed as previously described (Wang, Zhu et al. 2012, Chen, Hung et al. 2013) using NuPage 3-8% or 4-12% gels and the following antibodies:

Primary antibodies: anti-MIIA antibody (rabbit) (Sigma Aldrich M8064, 1:1000), anti-MIIB antibody (rabbit) (Cell Signaling 3404S, 1:1000), anti-DIA1 antibody (E-4) (mouse) (Santa Cruz Biotechnology SC-373807, 1:100). β-actin was used as a loading control (Purified Mouse Anti-Actin Ab-5, BD Biosciences 612656, 1:10,000).

Secondary antibodies: Anti-mouse IgG, HRP-linked Antibody (Cell Signaling 7076S, 1:2000), Anti-rabbit IgG, HRP-linked Antibody (Cell Signaling 7074S, 1:2000), donkey anti-goat IgG-HRP (Santa Cruz Biosciences sc-2020, 1:2000).

3.2.10 Statistical Analysis. Data represent the mean ± SD from ≥3 independent experiments for each condition unless stated otherwise. A two-tailed unpaired t test, a Mann-Whitney U test and a one-way ANOVA test were used to determine statistical

significance. Statistical significance was identified as $p < 0.05$. Analysis was performed using GraphPad Prism 6 and OriginPro 9 Software.

3.3 Results

3.3.1 Decision-Making Cascade Guided by the Persistent Growth of One Protrusion. To study cell decision-making patterns in confinement, we fabricated a microfluidic device consisting of an array of microchannel units (Fig. 3-1.A). Each unit contained a L = 200 μm straight base channel of 30 μm^2 cross section (W × H = 10 × 3 μm^2) which led to a trifurcated intersection. The intersection consisted of three channel branches (Left: W × H × L = 10 × 3 × 320 μm^3; Straight: W × H × L = 10 × 3 × 200 μm^3; Right: W × H × L = 20 × 3 × 2240 μm^3) each presenting a different hydraulic resistance that had to be overcome by the migrating cells (Fig. 3-1.B) (Left: intermediate resistance (1x), Straight: low resistance (0.6x), Right: high resistance (2.2x)) (Fuerstman, Lai et al. 2007).

Two cancer cell lines, MDA-MB-231 adenocarcinoma cells and HT-1080 fibrosarcoma cells, migrated through the channels and made decisions in a similar way; approximately 50% of the cells chose to enter the straight/low resistance channel (Fig. 3-1.C). If the front-rear polarization of the cells affected their persistence which in turn influenced the decision process (Ridley, Schwartz et al. 2003), we would expect that by creating a design where the lowest hydraulic resistance branch was located at the right side of the intersection (Left: high resistance (1x), Straight: intermediate resistance (0.6x), Right: low resistance (0.3x)) (Fig. 3-2.A, B), cells would continue migrating straight. However, this was not observed. In agreement with our previous results, 50% of cells in

both cell lines chose the right/low resistance branch (Fig. 3-2.C). This suggested that hydraulic resistance rather than the persistence of cells guided the decisions.

Interestingly, HT-1080 cells spent a much shorter time to make a decision (defined from the first cell contact with the intersection to complete entrance to a branch of the 1x-0.6x-2.2x design) (Fig. 3-2.D). Because HT1080 cells migrated faster than MDA-MB-231 cells (Fig. 3-2.E), we made time dimensionless by scaling it with each cell line's base channel speed and dividing it by a characteristic unit of length. Thus, we determined that both cells lines spent a similar amount of time within their own time frame for making decisions (Fig. 3-2.F).

We next studied the behavior of MDA-MB-231 cells at the intersection by tracking their normalized protrusion length (L / L_0, where L denotes the distance from the leading edge to either the entrance of the branch or the nucleus – whichever was shorter – and L_0 the cell length at the base channel) and cell entry times (Fig. 3-1.D, Fig. 3-2.G). The normalized protrusion lengths revealed that there was a time point t_0 when one protrusion persistently grew faster than the other two and became dominant. Since the cell entry time was not the same for all three branches of the trifurcation, with cells choosing the straight/low resistance branch being slower (Fig. 3-1.D), we normalized the time of the entire decision-making process for cells entering the same branches and grouped them together. By plotting the normalized leading protrusion length as a function of that time we observed the existence of three distinct phases (Fig. 3-1.E). On the first phase (exploratory) cells reached the trifurcation and extended/retracted lamellipodial or filopodial protrusions repeatedly. The competition among the three protrusions continued until, on the second phase (cell entrance), one protrusion became dominant and led the cell into one of the

branches. One the third phase (post nuclear entrance), the nucleus had fully entered the branch dictated by the leading protrusion and cells assumed either an elongated or compact morphology with smaller protrusion variations. As a result, we were able to determine the decision-making time point at the very end of the exploratory phase I, right before the persistent growth of one of the protrusions.

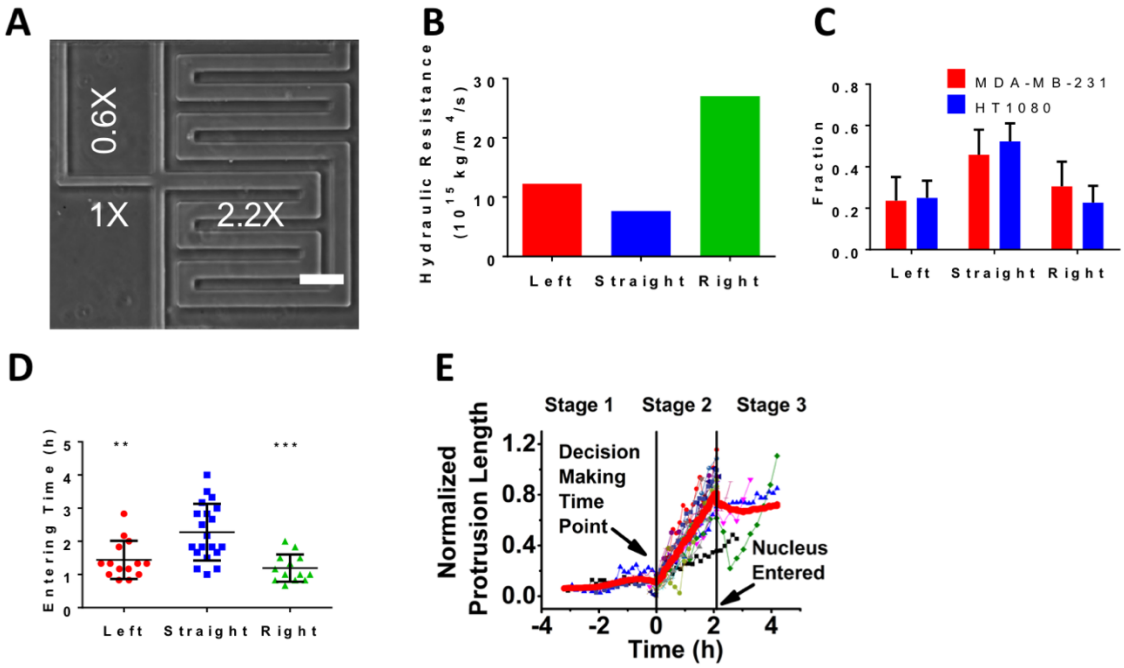

Figure 3-1. Decision-Making Pattern and Protrusion Dynamics Based on Hydraulic Resistance. **(A)** Phase contrast image of decision-making design (1X-0.6X-2.2X). Scale bar: 50 μm. **(B)** Hydraulic resistance calculated from channel geometry for three directions in **Fig. 3-1.A**. **(C)** Fraction of MDA-MB-231 and HT1080 cells entering the branches of the 1X-0.6X-2.2X design (n>70 from 3 independent experiments for each cell line). Data represent the mean with 95% confidence interval. **(D)** Entering time in each branch. Calculated from the beginning until the end of nuclear entrance (n>10 for each branch). The data represent mean±SD, one-way ANOVA, **p<0.01, ***p<0.001 relative to cells entering the straight branch. **(E)** Normalized leading protrusion length (L/L_0) from cells entering the straight branch of the 1X-0.6X-2.2X design (n=14). L denotes the distance from the leading edge to either the entrance of the branch or the nucleus – whichever was

shorter – and L_0 the cell length at the base channel. x-axis rescaled based on the mean value of time in phase II. Moving average is represented with the red line.

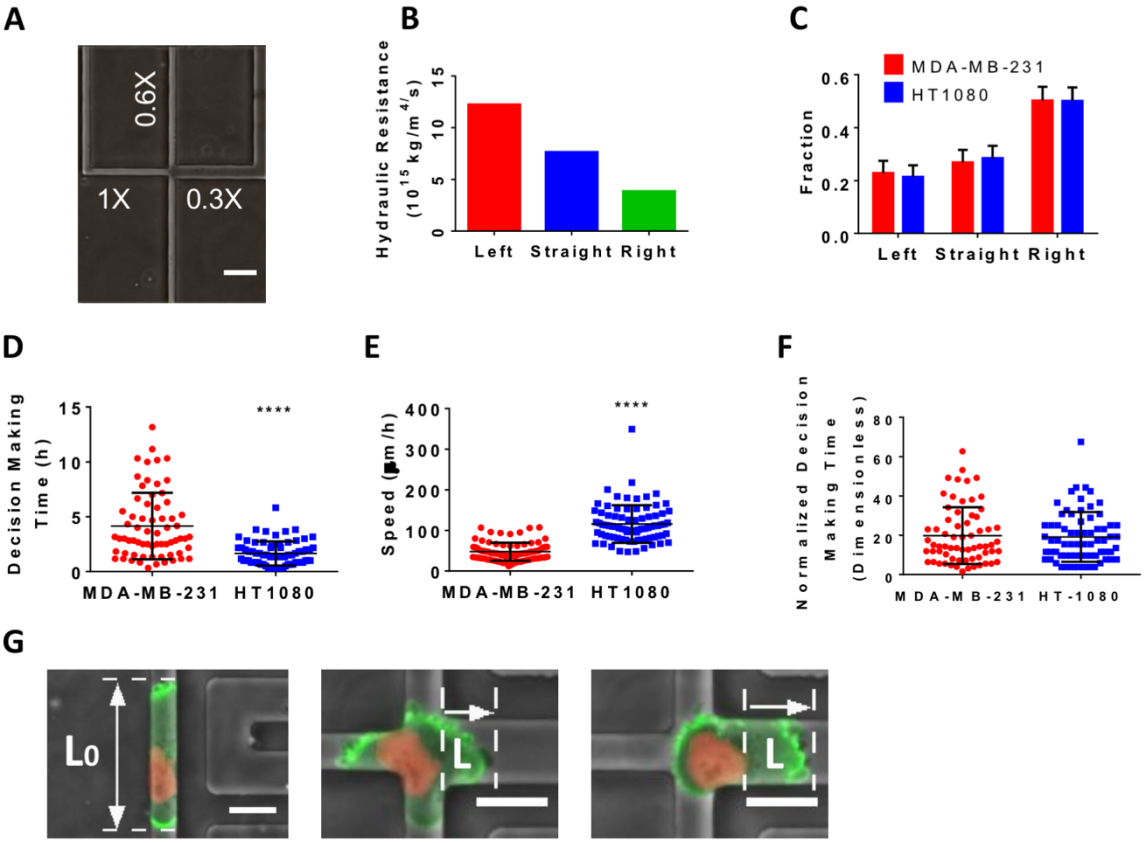

Figure 3-2. Decision-making is dependent on hydraulic resistance, and MDA-MB-231 and HT1080 cells spend equal amounts of time making decisions within their own time frame. **(A)** Phase contrast image of second decision-making design (1X-0.6X-0.3X). Scale bar: 50 μm. **(B)** Hydraulic resistance calculated from the channel geometry of each branch in **Figure 3-2.A**. **(C)** Fractions of MDA-MB-231 and HT1080 cells entering the branches of the 1X-0.6X-2.2X design (n>300 from 3 independent experiments for each cell line). Data represent the mean with 95% confidence interval. **(D)** Decision-Making time for MDA-MB-231 and HT1080 cells defined as the period between arrival at the intersection and complete nuclear entry to a branch (≥ 3 independent experiments). Data represent the mean±SD, two-tailed unpaired t test; ****p<0.0001 relative to MDA-MB-

231 cells. **(E)** Migration speed of MDA-MB-231 and HT1080 cells in the base channel (≥ 3 independent experiments). Data represent mean ± SD, two-tailed unpaired t test; ****p<0.0001 relative to MDA-MB-231 result. **(F)** Normalized decision-making time of MDA-MB-231 and HT1080 cells (≥ 3 independent experiments). Dimensionless decision-making time scaled by multiplying the migration speed and dividing by the characteristic channel dimension of 10 μm. Data represent mean ± SD. **(G)** Representative images of LifeAct-GFP H2B-mCherry MDA-MB-231 cells during decision-making. **(left)** Cell in base channel before reaching intersection. Overall cell length measured as L_0. **(middle)** Exploratory phase when cells randomly protrude into branches. Protrusion length measured as L. **(right)** Cell entering right channel after decision is made. Protrusion length measured as L. Scale bar: 20 μm.

3.3.2 Actin Nucleation Affects Cell Decision-Making Time and Myosin IIA Acts as a Mechanosensor of Hydraulic Resistance. The continuous protrusion growth/retraction cycles in the exploratory phase along with the persistent fast growth in the cell entrance phase prompted us to further investigate the role of the basic cytoskeletal structures of migrating cells. Using both cell decision designs (1x-0.6x-2.2x and 1x-0.6x-0.3x), we observed that most MDA-MB-231 cells expressed a blebbing phenotype at the intersections (Fig. 3-3.A). Since the cells with elongated protrusions (protrusive) did not occupy the entire intersection (Fig. 3-4.A) we continued our experiments by focusing only on the blebbing cells.

Several studies have reported that actin polymerization regulates the direction of cell migration. (Tojkander, Gateva et al. 2012, Kassianidou and Kumar 2015). As such, we used CK666 to pharmacologically inhibit Arp2/3, which is responsible for actin branching, in the 1x-0.6x-2.2x design. Although the decision-making pattern did not change (Fig. 3-3.B), the exploratory phase was prolonged significantly (Fig. 3-3.C). Given that the migration speed and persistence remained unchanged (data not shown), we concluded that Arp2/3 is important in finalizing phase I yet with no implications to the decisions made. Subsequently, we inhibited actin nucleation by generating a mDia1 knock-down (Fig. 3-4.B). Similarly to Arp2/3 inhibition, mDia1-KD increased the time to exit phase I, but did not affect the decisions made (Fig. 3-3.B, C). mDia1-KD cells migrated with the same speed and persistence as scramble controls (data not shown). The decision-making pattern altered significantly when we completely inhibited actin polymerization via high doses of latrunculin A (2μM). Cells migrated through the base channel at slower speeds, as previously reported (Stroka, Jiang et al. 2014) and 10% of our sample population made

decisions (Supplemental Fig. 3-4.C) with an extended exploratory phase (Fig. 3-3.C). From this subpopulation, 90% chose to enter the straight/low resistance channel (Fig. 3-3.B), thus showing an even stronger dependence on hydraulic resistance. Arp2/3 and mDia1 sped up decision-making by increasing the actin cortex assembly rate, but did not contribute to the decisions made. The presence of actin per se, though, appeared to be of paramount importance. The cell membrane may be critical in counteracting external forces, determining cell shape and regulating signaling which affects motility (Keren, Pincus et al. 2008, Tinevez, Schulze et al. 2009, Diz-Munoz, Krieg et al. 2010, Batchelder, Hollopeter et al. 2011, Bergert, Chandradoss et al. 2012, Salbreux, Charras et al. 2012, Diz-Munoz, Fletcher et al. 2013, Lieber, Yehudai-Resheff et al. 2013), yet upon actin depletion cells had a smaller chance of overcoming those forces. Actin was thus needed in order to help cells counterbalance and overcome higher hydraulic resistance forces.

Because latrunculin A-treated cells were able to choose the path of lowest resistance, we hypothesized that hydraulic resistance is sensed via other membranous or cytoskeletal elements which may play a critical role in decision-making. Hydraulic resistance acts as an energy barrier or a pressure drop to the impeding object (Harrison V. Prentice-Motta 2013, Bergert, Erzberger et al. 2015). Reports on the establishment of local high hydrostatic pressure through cortical contractility which can counter the external pressure (Raucher and Sheetz 2000, Charras, Yarrow et al. 2005, Keren, Pincus et al. 2008, Houk, Jilkine et al. 2012, Lieber, Yehudai-Resheff et al. 2013), enabled us to examine the effects of contractility in confined cell decision-making. Treatment of MDA-MB-231 cells with a high dose of blebbistatin (50 μM), which inhibits non-muscle myosin II, in the 1x-0.6x-2.2x design, increased the time to exit phase I and reversed the decision-making

pattern (Fig. 3-3.D, E). Cells preferred the right/high resistance channel. Subsequently, we generated MDA-MB-231 cells with myosin IIA (MIIA) and myosin IIB (MIIB) knock-downs (Supplemental Fig. 3-4.C) and investigated which myosin isoform played a greater role in this process. While MIIB-KD did not alter the decision pattern, MIIA-KD did, similarly to the blebbistatin treatment, without any changes in speed or persistence (Fig. 3-3.D). In contrast to the decision pattern, both MIIA-KD and MIIB-KD increased the time to exit phase I (Fig. 3-3.E).

Since membrane tension is primarily attributed to cortical actomyosin which, through the ezrin-radixin-moesin (ERM) complex, contributes to the membrane-to-cortex-attachment (MCA) (Charras, Hu et al. 2006, Salbreux, Charras et al. 2012, Diz-Munoz, Fletcher et al. 2013) we pharmacologically inhibited ezrin phosphorylation via NSC 668394 (Fig. 3-3.F). Once more, the decision pattern was altered and cells preferentially entered the right/high resistance branch. Our experiments suggest that cortical actomyosin contractile forces, which are transferred to the cell membrane via ezrin, are responsible for hydraulic resistance mechanosensing in confined migration decision-making. Either reduced contractility or lack of the connection between the contractile machinery and the cell membrane results in cell entrance to the high resistance branch.

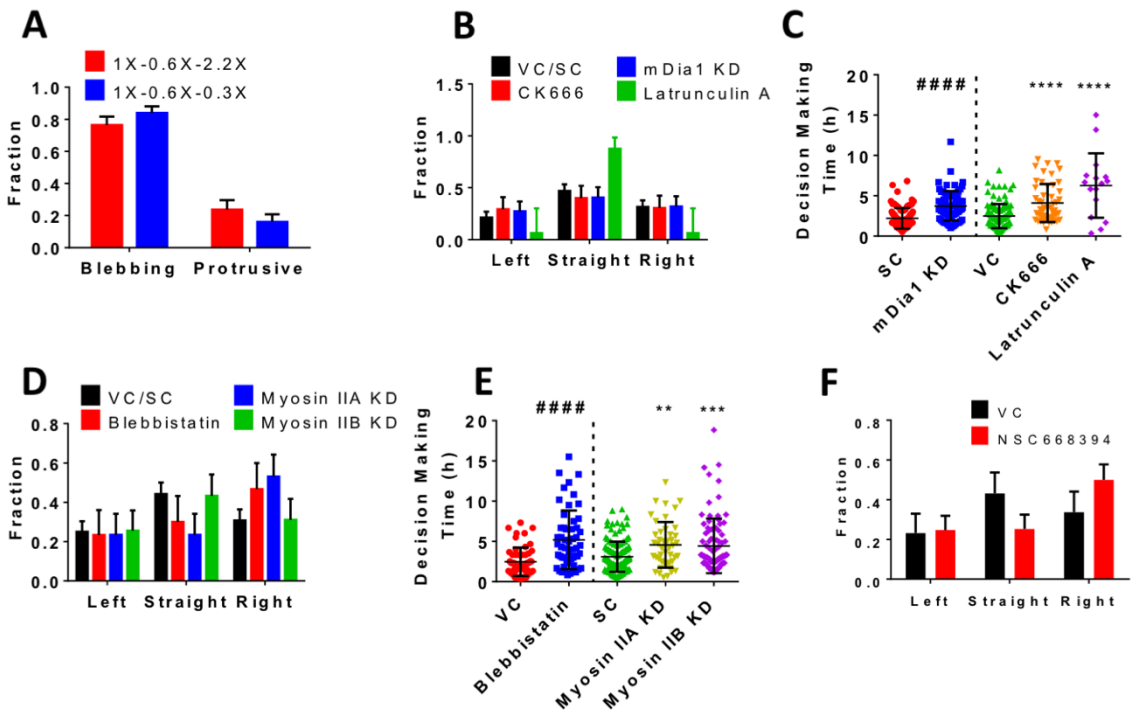

Figure 3-3. Influence of Actin Nucleation on Decision-Making Time and Hydraulic Resistance Mechanosensing via MIIA. (A) Fraction of blebbing vs. elongated protrusion phenotypes in two decision-making designs 1X-0.6X-2.2X and 1X-0.6X-0.3X (n>200 cells from ≥ 3 independent experiments for each design). Data represent the mean with 95% confidence interval. **(B)** Fraction of MDA-MB-231 cells entering branches of 1X-0.6X-2.2X design under Arp2/3 inhibition via CK666 (100 μM), actin depolymerization via latrunculin A (2 μM) and mDia1 knock-down (≥ 3 independent experiments for each condition). Data represent the mean with 95% confidence interval. **(C)** Decision-Making time of MDA-MB-231 cells entering branches of 1X-0.6X-2.2X design under Arp2/3 inhibition via CK666 (100 μM), actin depolymerization via latrunculin A (2 μM) and mDia1-KD, defined as the period from arrival at the intersection until complete nuclear

entry to a branch (≥ 3 independent experiments for each condition). Data represent the mean ± SD. One-way ANOVA, ****p<0.0001 relative to vehicle control. Mann-Whitney U test, ####p<0.0001 relative to scramble control. **(D)** Fraction of MDA-MB-231 cells entering branches of the 1X-0.6X-2.2X design under blebbistatin treatment (50 μM), Myosin IIA knock-down and Myosin IIB knock-down (≥ 3 independent experiments for each condition). Data represent the mean with 95% confidence interval. **(E)** Decision-Making time of MDA-MB-231 cells entering branches of the 1X-0.6X-2.2X design under blebbistatin treatment (50 μM), Myosin IIA knock-down and Myosin IIB knock-down, defined as the period from arrival at the intersection until complete nuclear entry to a branch (≥ 3 independent experiments for each condition). Data represent the mean ± SD. One-way ANOVA, **p<0.01, ***p<0.001 relative to scramble control. Mann-Whitney U test, ####p<0.0001 relative to vehicle control. **(F)** Decision-Making pattern of MDA-MB-231 cells under pharmacological ezrin inhibition via NSC668394 entering branches of the 1X-0.6X-2.2X design (n>30 cells from 3 independent experiments for each). Data represent the mean with 95% confidence interval.

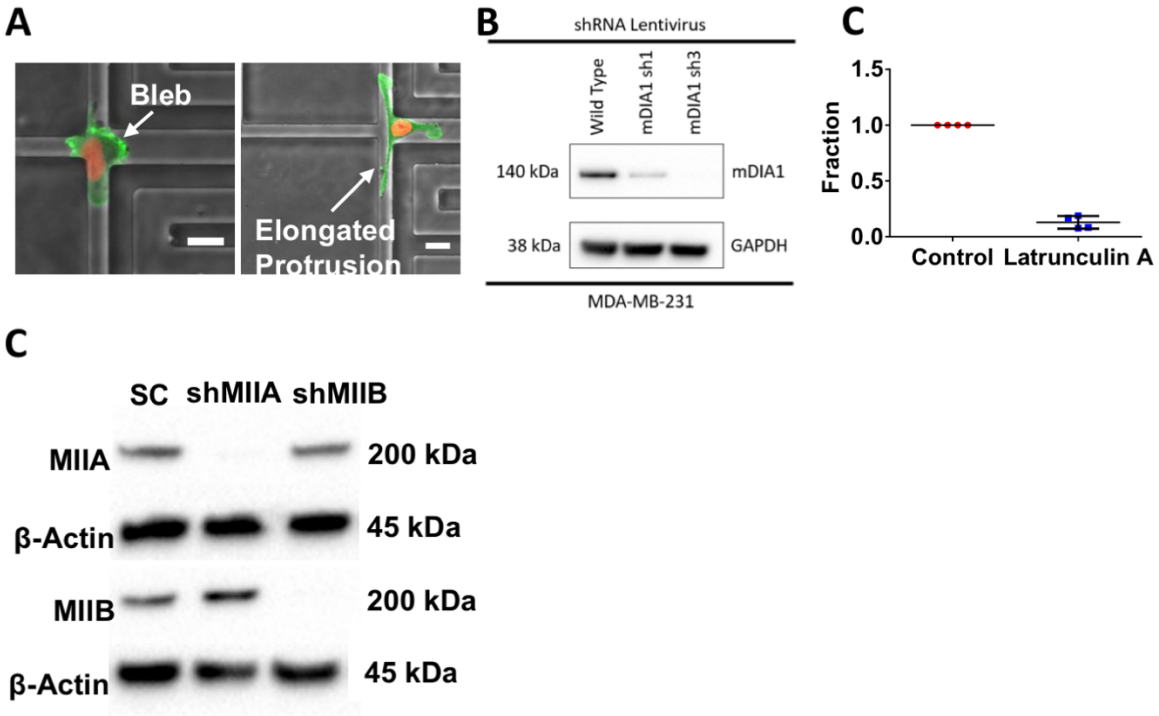

Figure 3-4. Cell morphologies at the intersection, mDia1-KD, MIIA-KD, MIIB-KD and fraction of the population that makes decisions under pharmacological actin depolymerization. (A) Representative images depicting the blebbing (left) and elongated protrusion (right) LifeAct-GFP H2B-mCherry MDA-MB-231 cells at the intersection. Scale bar: 100 μm. **(B)** Western blot showing the knock-down efficiency of two sequences (sh1, sh3) of shmDia1 on MDA-MB-231 cells. **(C)** Fraction of vehicle control and 2 μM Latrunculin A treated MDA-MB-231 cells that made a decision at the intersection. Data represent the mean ± SD. **(D)** Western blot showing the knock-down efficiency of shMIIA and shMIIB on MDA-MB-231 cells.

3.3.3 TRPM7 Channel Acts as the Primary Hydraulic Resistance Mechanosensor Leading to a Calcium Cascade which Helps Characterize the Decision-Making Process. The preferential entry of MDA-MB-231 cells under myosin or ezrin inhibition in the high resistance channels led us to hypothesize the following: either cells cannot sense the low hydraulic resistance or they can sense it but are unable to act accordingly. In addition, under myosin inhibition the high resistance branch on the right may be more appealing due to possible effects on actin polymerization. If sensing of the hydraulic resistance occurs via another mechanism, then it should depend on differential stretching of mechanosensitive ion channels on the cell membrane, which function by allowing calcium to enter the cell. Calcium has been acknowledged as a secondary messenger that controls multiple cell functions such as motility, division and apoptosis (Prevarskaya, Skryma et al. 2011, Chen, Hung et al. 2013, Azimi, Roberts-Thomson et al. 2014, Monteith, Prevarskaya et al. 2017) and its influx through ion channels has been shown to direct 2D migration and trigger cytoskeletal remodeling (Wei, Wang et al. 2009, Balzer, Tong et al. 2012). Thus, we treated MDA-MB-231 cells with Bapta-AM which chelates all intracellular calcium. Without any effects on migration speed or persistence (data not shown), the chelator resulted in a change of the decision pattern towards the right/high resistance branch (Fig. 3-5.A). Since the mechanosensitive TRP channels are highly expressed in breast cancer cells (Dhennin-Duthille, Gautier et al. 2011, Ouadid-Ahidouch, Dhennin-Duthille et al. 2013) and after activation through membrane stretching allow Ca^{2+} ion influx, we inhibited them pharmacologically and investigated any possible decision-making effects. In agreement with our data using MIIA-KD or Bapta-AM, treatment with 2-APB, which inhibits all TRP channels and the inositol 1,4,5-triphosphate

receptor (IP_3R), altered the decision pattern and cells preferentially entered the right/high resistance branch (Fig. 3-5.A). Subsequently, in order to identify the specific TRP channel which is involved in confined cell mechanosensing, we used a series of pharmacological inhibitors against mechanosensitive ion channels that have been reported to be highly expressed in MDA-MB-231 cells (Aydar, Yeo et al. 2009). Both GsMTx-4 (which inhibits TRPC1, TRPC6 and Piezo1 channels) and HC 067047 (which inhibits TRPV4 channels) did not lead to a change in the cell decision pattern (Fig. 3-6.A). However, treatment with SKF-96365 which blocks STIM/ORAI1 calcium channels on the endoplasmic reticulum (ER) and are activated by IP_3R changed the decision pattern to the one observed with 2-APB (Fig. 3-5.A). Thus, IP_3R plays a key role in decision-making. Moreover, cells treated with FTY720, which has been reported to inhibit the TRPM7 channel (Qin, Yue et al. 2013), altered the decision making pattern towards the high resistance channel (Fig. 3-5.A). In order to eliminate any possible side effects from the pharmacological inhibitor of TRPM7, we knocked out TRPM7 in MDA-MB-231 cells via CRISPR/Cas9 (Fig. 3-6.B) and verified that the decision pattern favored entry into the high resistance branch (Fig. 3-5.A). Of note, Ca^{2+}, IP_3R or TRP channel inhibition did not alter the decision making time (Fig. 3-6.C). Thus, we concluded that cells have the ability to sense hydraulic resistance through the TRPM7 channel. In addition, the change of the decision pattern from STIM/Orai1 and IP_3R inhibition suggests that calcium entry through the TRPM7 channel is captured by the IP_3R at the ER, causes the STIM1 channel to release stored calcium to the cytosol and the conjugated Orai1 channel opens to restore calcium. Any loss of function of these channels leads to a loss in mechanosensitivity.

In our experiments, the right branch with the high hydraulic resistance had also a larger cross-sectional area. To examine whether TRPM7-KO cells preferentially entered this branch due to the high hydraulic resistance or due to the larger opening presented, we designed two devices which either maintained the same hydraulic resistance in all branches of the trifurcation yet with different cross-sectional areas (Fig. 3-5.B) or maintained the same cross-sectional area and had different hydraulic resistances (Fig. 3-5.D). In the device with the different hydraulic resistances, control cells preferentially entered the low resistance branch, while the TRPM7-KO cells entered all branches with equal probability (Fig. 3-5.C), and in the device with the same hydraulic resistance, control cells entered all branches with the same probability and TRPM7-KO cells preferred the branch with the larger cross-section (Fig. 3-5.E). This set of experiments indicated that cells with a defective mechanosensory mechanism do not choose the branch with the highest resistance but switch to a decision pattern based on the cross section of the intersecting branch.

As calcium signaling appears to be critical for cell decision-making in confinement, we used Fluo-4 Direct, a fluorescent Ca^{2+} indicator, to image intracellular Ca^{2+} as the cells were exploring the intersection of a 1x-0.6x-2.2x device. We observed that the overall Ca^{2+} levels spiked (calcium sparks) in a cyclical manner through the exploratory phase (Fig. 3-5.F). However, we did not observe any calcium flickers. Furthermore, TRPM7-KO cells exhibited a lower frequency of calcium sparks (Fig. 3-5.G) yet with the same spark intensity (Fig. 3-5.H), indicating that there may be other triggers of global calcium increase. Control cells exhibited two interesting characteristics. First, at the exploratory phase, when cells occupied the entire intersection, Ca^{2+} intensity on the right protrusion was higher than the left which, in turn, was higher than the straight. This was evidence that Ca^{2+}

correlates with hydraulic resistance (Fig. 3-5.I). Second, at the decision-making time point, which we determined based on the protrusion dynamics, Ca^{2+} signal on all three protrusions fell to the same level (Fig. 3-5.I). As such, cells exhibited a momentary Ca^{2+}equilibrium.

As Ca^{2+} facilitates contractility via its interaction with calmodulin and myosin light chain kinase (MLCK) which generates a local high intracellular pressure and pulls the actin cortex from the cell membrane, we studied the bleb sizes on all three protrusions. The variation of the bleb size is an indication of the physical instability of the cell membrane (Charras, Yarrow et al. 2005, Tinevez, Schulze et al. 2009, Batchelder, Hollopeter et al. 2011). Our experiments indicated that the deviation of the maximum bleb size between the three protrusions drops sharply to a minimum at the decision-making time point (Fig. 3-5.J). This indicated an equal membrane stretch on all three branches. In addition, at the same time point we observed a minimum in the actin variance of LifeAct-GFP cells between the three branches (Fig. 3-5.K). By subtracting the actin intensity of one frame from the next, we observed that, at the decision-making point, actin intensity changes the least during the exploration phase (Fig. 3-6.D, E, decision-making point: 4:30). These experiments suggest the existence of a contractile equilibrium at the decision-making time point.

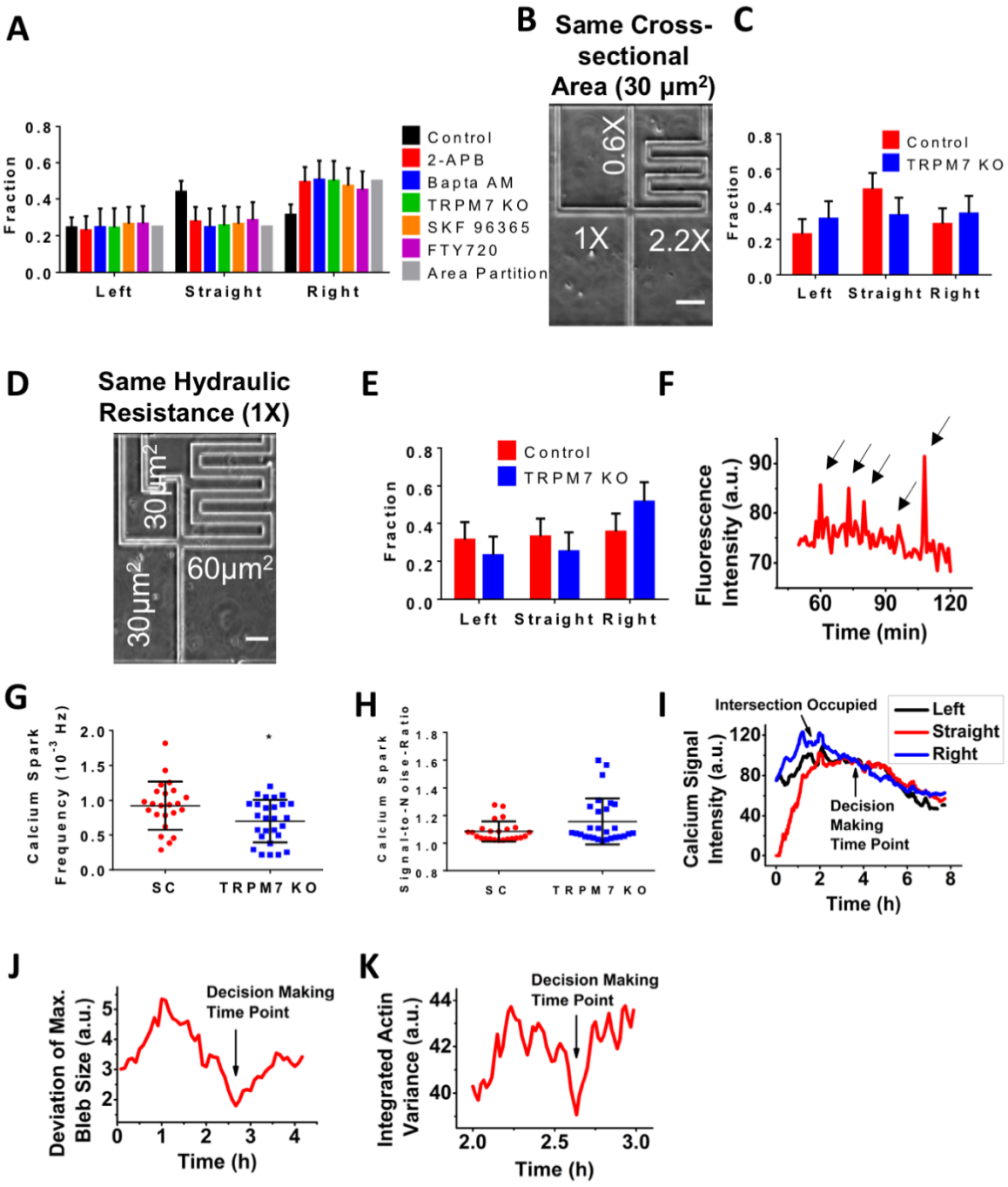

Figure 3-5. Hydraulic Resistance Mechanosensing via TRPM7 Channel Correlates with Ca^{2+} Signaling. **(A)** Fraction of MDA-MB-231 cells entering branches of the 1X-

0.6X-2.2X design under TRP channels inhibition via 2-APB (100 μM), calcium chelation via bapta-AM (25 μM), TRPM7 knock-out, ezrin inhibition via SKF 96365 (10 μM) and TRPM7 inhibition via FTY720 (2 μM), compared with area partition calculation derived from the probability of cells entering a branch based on its cross-sectional area (Probability of entering branch 1 = Area of Branch 1 / (Area of branch 1 + Area of branch 2 + Area of branch 3) (≥ 3 independent experiments for each condition). Data represent the mean with 95% confidence interval. **(B)** Phase contrast image of same-area-different-resistance design (1X-0.6X-2.2X) (30 μm^2-30 μm^2-30 μm^2). Scale bar: 50 μm. **(C)** Fraction of MDA-MB-231 scramble control and TRPM7 knock-out cells entering branches in the same-area-different-resistance design 1X-0.6X-2.2X (≥ 3 independent experiments). Data represent the mean with 95% confidence interval. **(D)** Phase contrast image of same-resistance-different-area design (1X-1X-1X) (30 μm^2-30 μm^2-60 μm^2). Scale bar: 50 μm. **(E)** Fraction of MDA-MB-231 scramble control and TRPM7 knock-out cells entering branches in the same-resistance-different-area design (30 μm^2-30 μm^2-60 μm^2) (≥ 3 independent experiments). Data represent the mean with 95% confidence interval. **(F)** Representative graph of global cell calcium levels measured by Fluo-4 direct assay on MDA-MB-231 cells over time during decision-making phase I. Arrows indicate calcium sparks. **(G)** Frequency of calcium sparks in MDA-MB-231 scramble control (SC) and TRPM7 knockout cells (n≥20) as they enter branches of the 1X-0.6X-2.2X design. Data represent the mean ± SD, two-tailed unpaired t test; *p<0.05 relative to scramble control. **(H)** Signal-to-Noise-Ratio of calcium sparks in MDA-MB-231 SC and TRPM7 knockout cells during decision-making phase I in the 1X-0.6X-2.2X design (n≥20). Data represent the mean ± SD. **(I)** Representative graph of calcium intensity signal at each protrusion of

a cell during decision-making in the 1X-0.6X-2.2X design. Arrows indicate the time point of the first occupation of the intersection and the decision-making time point. **(J)** Representative graph of the standard deviation of the maximum bleb sizes between the three protrusions of a cell during decision-making in the 1X-0.6X-2.2X design over time. Arrow indicates the decision-making time point. The same cell is presented in **Fig. 3-5.K**. **(K)** Representative graph of the variance of the integrated actin signal between the three protrusions of a cell during decision-making in the 1X-0.6X-2.2X design over time. Arrows indicate the decision-making time point.

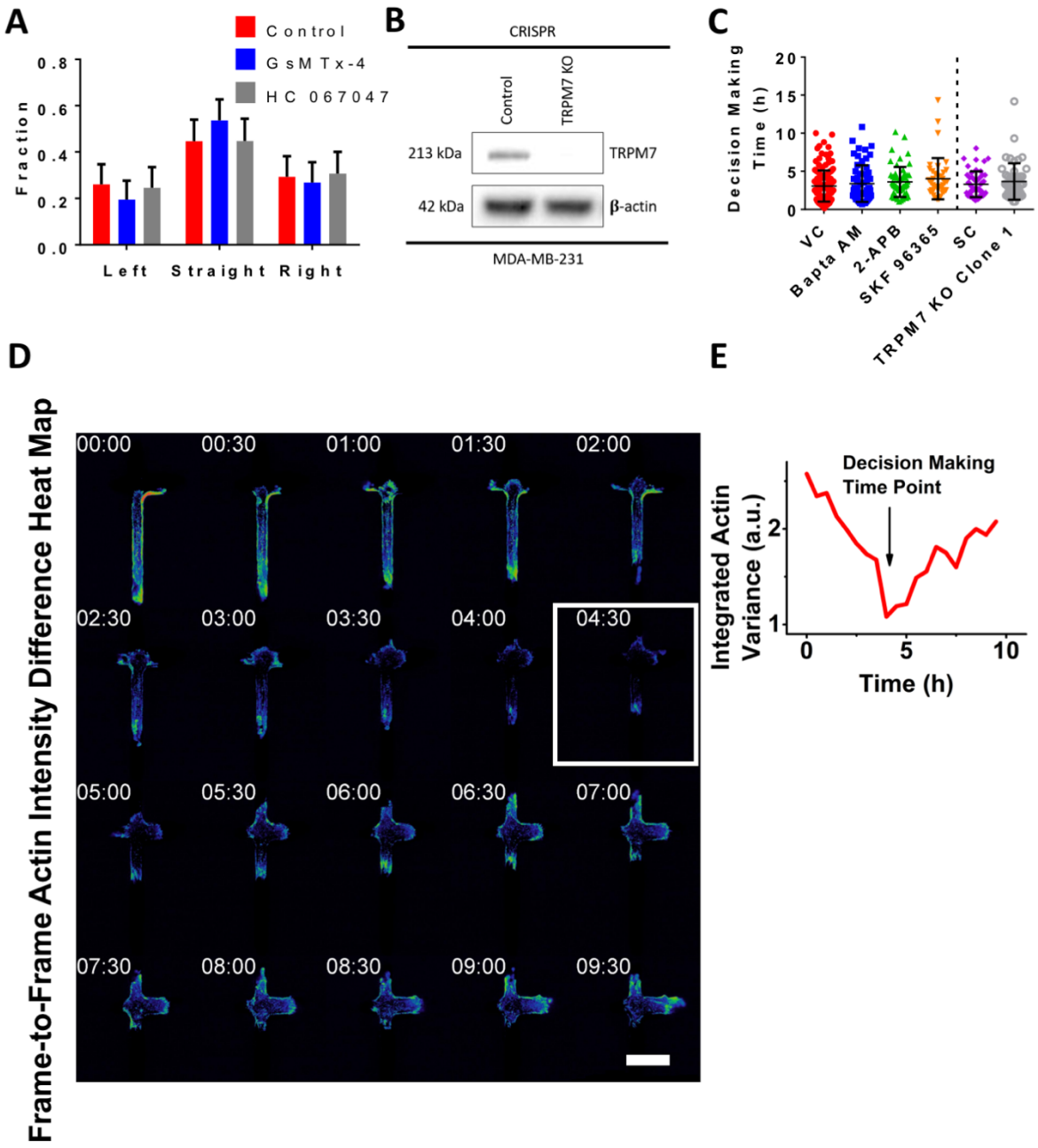

Figure 3-6. Ion channel pharmacological inhibition, knock-out of TRPM7 channel, decision-making time under calcium chelation and ion channel inhibition, and actin equilibrium at the decision-making time point. **(A)** Fraction of MDA-MB-231 cells

entering branches of the 1X-0.6X-2.2X design under TRPC1, TRPC6, Piezo1 channel inhibition via GsMtx-4 (20 μM) and under TRPV4 channel inhibition via HC 067047 (5 μM), (n>50 cells from 3 independent experiments for each treatment). Data represent the mean with 95% confidence interval. **(B)** Western blot showing the knock-out efficiency of CRISPR TRPM7 on MDA-MB-231 cells. **(C)** Decision-Making time of MDA-MB-231 cells entering branches of the 1X-0.6X-2.2X design under TRP channels inhibition via 2-APB (100 μM), calcium chelation via bapta-AM (25 μM), TRPM7 knock-out, ezrin inhibition via SKF 96365 (10 μM), defined as the period from arrival at the intersection until complete nuclear entry to a branch. Data represent the mean $\pm$ SD. **(D)** Representative frame-to-frame actin intensity difference heat map of a LifeAct-GFP MDA-MB-231 cell during decision-making. Decision made around 4:30 h (white box). Scale bar: 50 µm. **(E)** Variance of the integrated actin signal between the three protrusions of the cell presented in **Fig. 3-6.D** during decision-making over time. Arrow indicates the decision-making time point.

3.3.4 Relationship Between Hydraulic Resistance, Actin and Myosin Helps Build a Theoretical Framework for Cell Decision-Making. In order to investigate the relationship between actin, myosin and hydraulic resistance, we generated LifeAct-GFP and Myosin IIA-GFP MDA-MB-231 cell lines and studied the actin and myosin signal intensities in all three protrusions at the intersection of the 1x-0.6x-2.2x device. By subtracting the background actin and myosin signals at the central part of the cell from the signals at the protrusions (Fig. 3-8.A) and integrating the residual signal intensity in each protrusion, we revealed that at the decision-making time point all cells present the least amount of actin at the straight/low resistance protrusion and roughly equal amounts on the left and right (Fig. 3-7.A). Myosin, on the other hand, exhibited a more direct relationship with hydraulic resistance (Fig. 3-7.B); high resistance corresponded to high myosin and low resistance to low myosin. TRPM7-KO cells do not show differences in the amount of actin or myosin that they localize at the protrusions (Fig. 3-7.A, B).

Subsequently, we created four different designs (1x-0.6x-0.17x, 1x-0.3x-0.8x, 1x-0.6x-1.25x, 1x-0.6x-5x) which together with our 1x-0.6x-0.3x and 1x-0.6x-2.2x gave us a wide range of hydraulic resistances in order to examine the amounts of actin and myosin employed in each protrusion as a function of resistance (Fig. 3-8.B). While actin first increased monotonically with increasing hydraulic resistance, it plateaued at the threshold of 1x (W: 10 μm, H: 3 μm, L: 320 μm) (Fig. 3-7.C, box). On the contrary, myosin IIA correlated directly with resistance from low to high regimes (Fig. 3-7.C). By contrasting the cell speed at the post nuclear entrance phase inside the branches with the growth rate of the protrusions in the same branch at the cell entrance phase, we observed that protrusion

growth rate, similarly to actin, plateaued at high hydraulic resistances (Fig. 3-7.D). This suggests that the ability of cells to enter the high resistance branch is limited by actin.

Using actin as the limiting factor for entrance into environments of various hydraulic resistances, we created a simple model for decision-making. As cell shape transformations in packed tissues have an energy barrier which follows an exponential distribution (Bi, Lopez et al. 2014), we drew a parallel to 3D confined migration. Cells experienced a stopping force caused by the hydraulic resistance. After the decision-making time point, cells squeezed into one of the narrow opening branches. By the force balance across the cell membrane, the pressure drop caused by the hydraulic resistance ΔP was balanced by the local internal cell pressure, P_c, minus the surface tension of the membrane, T_c. The pressure drop was calculated as described by (Fuerstman, Lai et al. 2007), and the volumetric flow rate was obtained from the leading protrusion dynamics (Fig. 3-8.C). The membrane tension, thus, was expressed by $T_c = \frac{P_c - \Delta P}{2}\left(\frac{1}{W} + \frac{1}{H}\right)^{-1}$. We approximated $P_c - \Delta P \approx \Delta P$, assuming that the internal pressure was on the same order of magnitude as the pressure from the hydraulic resistance. From the surface tension we calculated the surface energy, E, required for each branch and finally plugged it into the linear probability equation, $P_{i,i=\text{left,straight or right}} = \frac{\exp\left(-\frac{E_i}{E_{ref}}\right)}{\sum \exp\left(-\frac{E_i}{E_{ref}}\right)}$. As the reference energy, E_{ref}, is a background surface energy that can be applied throughout the cell, we assigned it to the smallest value of E_i, which was calculated at the lowest hydraulic resistance branch. In this model we assumed cortical actomyosin as the provider of the major physical support to the cell. In the cases where cells were devoid of actin e.g. high dose latrunculin A treatment, the reference energy was substituted by the random heat fluctuation, kT, meaning that the

hydraulic resistance was counteracted by random fluctuations of the lipid bilayer. When comparing the theoretical decision-making probability pattern with the experimental values on two designs (1x-0.6x-2.2x and 1x-0.6x-0.3x)(Fig. 4E, H), we achieved a good prediction of the decision pattern when actin was absent (Fig. 3-7.G, J) but our model failed to accurately predict the experimental data when cortical actin was present (Fig. 3-7.F, I). This inaccuracy was attributed to the non-linear relation between the balancing force/energy of the actin cortex and the hydraulic resistance. As such, we substituted the surface energy term, E_i, with the integrated actin signal of each protrusion multiplied by an arbitrary unit of energy, e, assuming that the force load per actin fiber was the same everywhere; hence $E_i = N_{actin,i} \cdot e$. The arbitrary unit of energy was cell dependent and eventually canceled out in the final probability distribution: $P_{i,i=left,straight\ or\ right} = \frac{\exp\left(-\frac{N_i}{N_{ref}}\right)}{\sum \exp\left(-\frac{N_i}{N_{ref}}\right)}$ (N: relative amount of actin based on signal intensity, N_{ref}: minimum value of N_i). Our new probability distribution agreed with the experimental data (Fig. 3-7.F, I).

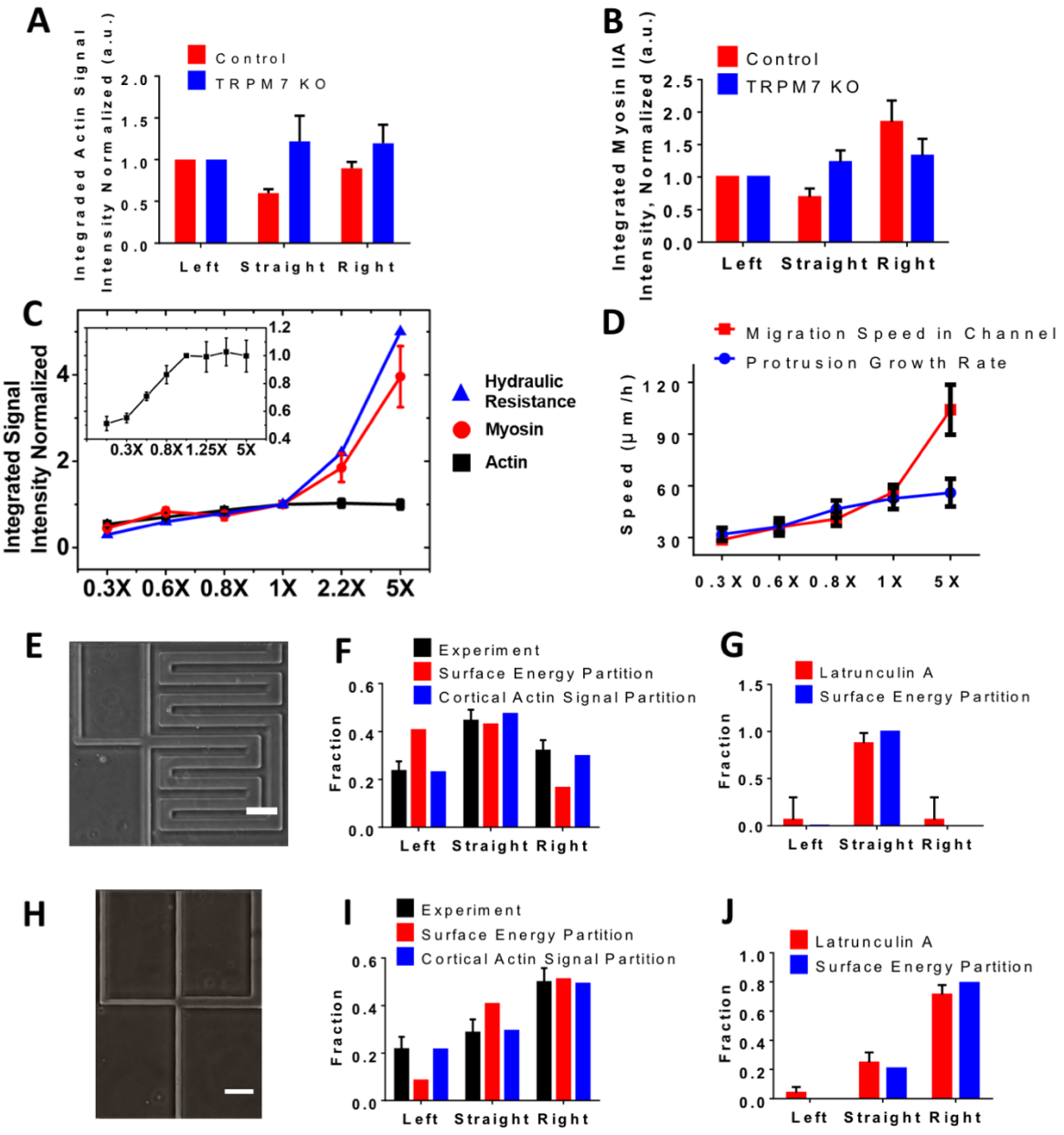

Figure 3-7. Hydraulic Resistance Affects Actin and Myosin IIA Levels at the Protrusions which Help Build a Model for Predicting Decision-Making Patterns. (A) Integrated actin signal between the three protrusions of LifeAct-GFP MDA-MB-231

scramble control and TRPM7 knock-out cells in the 1X-0.6X-2.2X design (n>10 cells from 3 independent experiments), all normalized to the left branch protrusion actin signal. **(B)** Integrated myosin IIA signal between the three protrusions of MIIA-GFP scramble control and TRPM7 knock-out MDA-MB-231 cells in the 1X-0.6X-2.2X design, all normalized to the left branch protrusion MIIA signal (n>10 cells from 3 independent experiments). **(C)** Integrated actin and MIIA signal intensity at the protrusions of LifeAct-GFP and MIIA-GFP MDA-MB-231 cells at the decision-making time point as a function of hydraulic resistance (normalized to the values at 1X) (n>10 cells for each data point). Box: Integrated actin signal intensity at the protrusions of LifeAct-GFP MDA-MB-231 cells at the decision-making time point as a function of hydraulic resistance (normalized to the values at 1X) with extra data points. Data represent the mean ± SD. **(D)** Migration speed inside branches of various hydraulic resistances and leading protrusion growth rate at phase II of MDA-MB-231 cells (n>10 cells for each data point). Data represent the mean ± SD. **(E)** Phase contrast image of decision-making design (1X-0.6X-2.2X). Scale bar: 50 μm. **(F)** Comparison between experimental decision-making pattern of MDA-MB-231 cells in the 1X-0.6X-2.2X design**,** and the predictions by the surface energy-based partition model and the cortical actin signal-based partition model (≥ 3 independent experiments). Data represent the mean with 95% confidence interval. **(G)** Comparison between the experimental decision-making pattern of MDA-MB-231 cells in the 1X-0.6X-2.2X design under actin depolymerization treatment via latrunculin A (2 μM) and the predictions by the surface energy-based partition model (≥ 3 independent experiments). Data represent the mean with 95% confidence interval. **(H)** Phase contrast image of the decision-making design 1X-0.6X-0.3X. Scale bar: 50 μm. **(I)** Comparison between the experimental

decision-making pattern of MDA-MB-231 cells in the 1X-0.6X-0.3X design, and the predictions by the surface energy-based partition model and the cortical actin signal-based partition model (≥ 3 independent experiments). Data represent the mean with 95% confidence interval. **(J)** Comparison between the experimental decision-making pattern of MDA-MB-231 cells in the 1X-0.6X-0.3X design under actin depolymerization treatment via latrunculin A (2 μM) and the predictions by the surface energy-based partition model (≥ 3 independent experiments). Data represent the mean with 95% confidence interval.

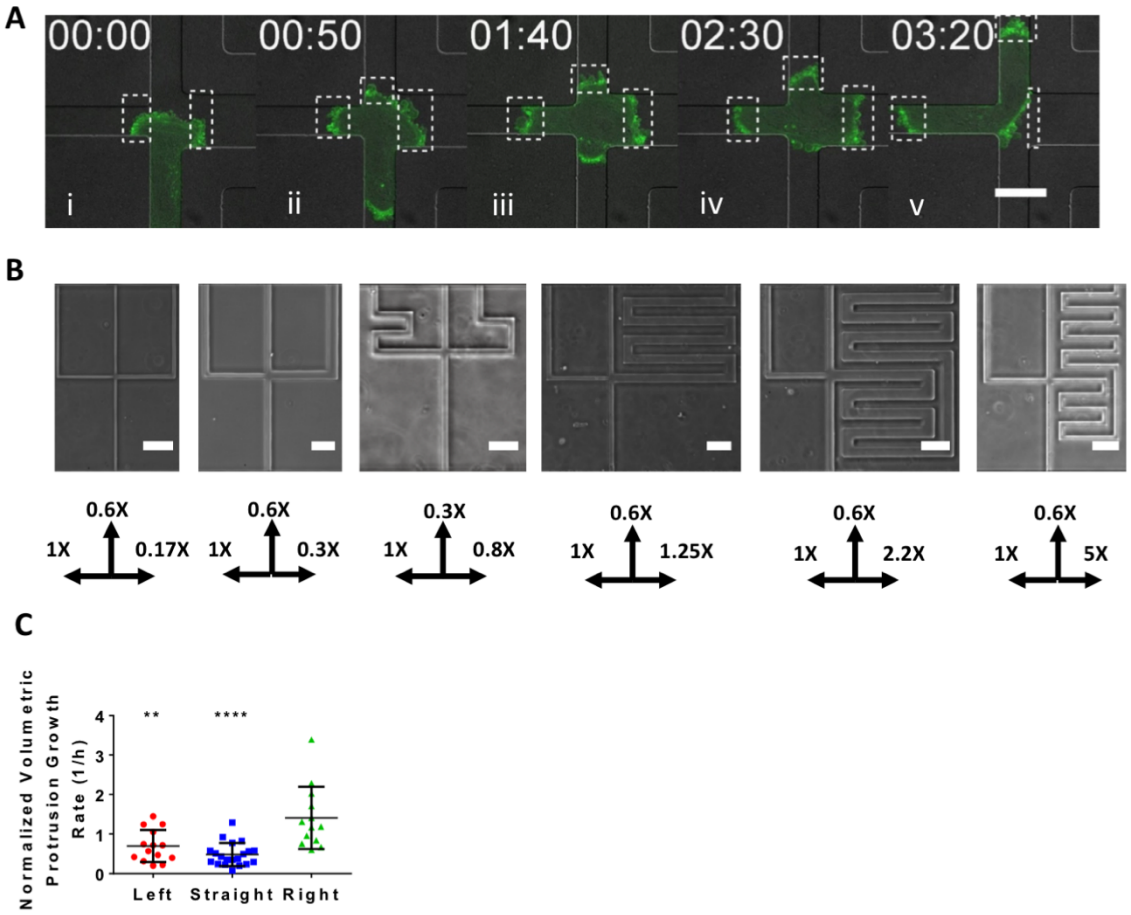

Figure 3-8. Actin signal at the protrusions during decision-making, designs of various hydraulic resistance combinations and volumetric protrusion growth rate at intersection branches. (A) Representative image sequence depicting the actin signal at the protrusions (areas in dashed boxes) of a LifeAct-GFP MDA-MB-231 cell during decision-making in the 1X-0.6X-2.2X design. Decision-making time point at iv (2:30). **(B)** Decision-Making trifurcated designs with various combinations of hydraulic resistances used in the experiments for **Fig. 3-8.C**. Arrows at the bottom indicate the direction of branches with their relative hydraulic resistances. Scale bar: 50 μm. **(C)** Leading protrusion growth rate at decision-making phase II of MDA-MB-231 cells in the 1X-0.6X-2.2X

design (n>10 for each direction), normalized by the entering time presented in **Fig. 3-1.D**. Data represent the mean ± SD, one-way ANOVA, **p<0.01, ****p<0.0001 relative to cells turning right at the high resistance branch.

3.4 Discussion

Decision-making in 3D confined microenvironments has been attributed to hydraulic resistance. Low hydraulic resistance correlates with a high probability that cells within a population will enter these branches at an intersection of channels. However, there is no significant evidence that explains the decisions-made, the proteins involved in hydraulic resistance sensing and the cytoskeletal changes which lead to cell decisions. Our work establishes a comprehensive analysis of the cell decision-making process and identifies the main cytoskeletal and membranous proteins involved.

Cells at the intersections of confining micro-channels regulate the localization of actin and myosin in order to balance hydraulic resistance forces. Our actin depolymerization experiments provide evidence that actin is not a mechanosensor yet its nucleation affects the time it takes for decisions to occur. Myosin IIA, on the other hand, plays a critical role in hydraulic resistance sensing and guides cell motility towards the branch of lowest resistance. As cell membrane tension has to overcome hydraulic resistance forces exerted by the liquid which fills the micro-channel branches, the transfer of actomyosin forces to the membrane via the membrane-to-cortex-attachment is of utmost significance. As such, ezrin mediated attachment of cortical actomyosin to the cell membrane allows cells to propagate these forces and respond to hydraulic resistance.

The persistent growth of one cell protrusion is an indication of the decision made. Thus, any partial cell entering in a different branch than the one denoted by the leading protrusion is a false entering and cells retract back to the intersection and continue the assessment of the micro-environment.

The three phases of the decision-making process are important in characterizing cell behavior at the intersection. Each has its own time course and entails a sequence of events that have to take place for successful decision-making to occur. First, cells reach the intersection and start exploring their environment by generating protrusions in all directions. Hydraulic resistance forces stretch the cell membrane unequally and TRPM7 channels activate differentially on each protrusion based on these forces. Calcium enters the cell and the IP_3R at the ER activates the STIM1 channel to release stored calcium into the cytosol. At the same time actin and myosin localize at the cell protrusions based on hydraulic resistance. Calcium binds to calmodulin and MLCK, stimulates contraction and generates a local differential pressure within each protrusion. In addition, ezrin transfers the contractile forces to the cell membrane and cells reach a local dynamic equilibrium designated by small changes in calcium concentration and polymerized actin within each protrusion. Cells compile the different external hydraulic resistance forces and choose to initiate a persistent growth of one of the protrusions via mDia1 and Arp2/3. Cellular entry into one of the branches is guided by the leading protrusion which grows continuously until the nucleus fully enters one of the branches. Subsequently, cells change or maintain their morphology based on the hydraulic resistance encountered in order to successfully maintain their motility within the selected branch without, however, any major changes in their leading protrusion length.

TRPM7 channel is expressed in various tissues such as the brain, spleen, kidney, lung, liver and heart (Nadler, Hermosura et al. 2001, Runnels, Yue et al. 2001). Regarding cancer, its expression has been reported in head and neck carcinoma (Dou, Li et al. 2013), retinoblastoma (Hanano, Hara et al. 2004), breast cancer (Dhennin-Duthille, Gautier et al.

2011) and gastric cancer (Kim, Park et al. 2008). TRPM7 knock-down or its pharmacological inhibition has been reported to reduce ischemic stroke (Sun, Jackson et al. 2009) and arrest proliferation of human pancreatic cancer cells (Yee, Zhou et al. 2011, Yee, Kazi et al. 2015). Furthermore, TRPM7 is required for cell migration of nasopharyngeal carcinoma (Chen, Luan et al. 2010), pancreatic adenocarcinoma (Rybarczyk, Gautier et al. 2012) and lung carcinoma (Gao, Chen et al. 2011).

Our experiments suggest that cells with TRPM7 migrate by following the path a least resistance. This may increase the metastatic efficiency of cells within the body. Downregulation of TRPM7 results in decisions based on the cross sectional area of the microchannels in which cells prefer the larger openings. As such, we speculate that migration and homing of tissues with small ECM porosities will be reduced. Cells will occupy larger spaces which allow for better diffusion of pharmacological agents rendering more efficient cancer therapies. As cells with downregulated myosin IIA follow the same decision-making pattern, we hypothesize that cell migration in really soft 3D environments within the body, which do not require cell to express high levels of myosin II (Petrie and Yamada 2012), will be subjected to the same principles. Decisions will be guided by the size of the open tracks within the tissues which can facilitate therapeutic interventions.

Chapter 4

CONCLUSIONS AND FUTURE DIRECTIONS

4.1 Advantages of microfluidic devices

Microfluidic devices are composed of small dimension channels, chambers and valves, which can be manipulated to perform precise, complicated operations. The size of the microchannels in the devices allow for easy mass and heat transfer, faster detection, high throughput screening, high speed analysis, improved sensitivity with low consumption of samples and reagents, and greatly reduced costs (Nge, Rogers et al. 2013). In addition, the small size of the devices render them portable and as such, they can be used as point-of-care tools for on-site testing. They can integrate multiple processes such as purification, separation and detection and achieve multiplex analysis (Whitesides 2006). Due to their unique features and advantages, microfluidic systems have been used in various scientific, engineering and medical fields.

4.2 Protein and nucleic acid detection by microfluidic devices

Recent advances in microfluidics have showcased their potential for protein and nucleic acid detection. The current state of art for detecting proteins as a diagnostic tool in clinical laboratories is the enzyme-linked immunosorbent assay (ELISA). It utilizes antibodies and the color change of reactions in order to identify protein markers. While it

is has achieved a widespread use, it requires several steps of washing and reagent incubation, which are time consuming. Chin and colleagues recently showed that it is possible to miniaturize these steps into a small microfluidic chip (mChip), which is loaded with wash buffer and reagents over an antibody coated detection region (Chin, Laksanasopin et al. 2011). The mChip was able to detect human immunodeficiency virus (HIV) antigen in 1 μL of unprocessed whole blood. In addition, the assay was completed in 20 min. Further studies coupled the microfluidic ELISA into a dongle that was attached to a smartphone and performed detection of HIV and syphilis (Laksanasopin, Guo et al. 2015).

Paper-based microfluidic chips have been recently fabricated. Their low weight, ease of use, biocompatibility and low cost have made them perfect candidates for molecular analysis in on-site detection. They have been shown to detect numerous biomarkers such as HIV and influenza virus antigens and tumor markers (Song, Zhang et al. 2012, Lei, Huang et al. 2015, Li, Xuan et al. 2015).

Detection of nucleic acids from biological samples, in order to obtain genetic information for disease diagnosis, is still challenging to achieve. Recently, the combination of microfluidics with bead technology has been able to achieve high-efficiency collection of DNA from only 100 cells for epigenomic analysis (Reinholt and Baeumner 2014, Cao, Chen et al. 2015). Ferguson and colleagues have developed a magnetic integrated microfluidic electrochemical detector, which can perform immunomagnetic target capture, concentration, purification, PDR amplification and electrochemical detection of influenza H1N1 from throat swab samples (Ferguson, Buchsbaum et al. 2011).

4.3 Microfluidics in cell sorting

Cell sorting is used to enrich and purify cell populations. Clinically, it is applied for capturing cells presenting distinct properties and either performing diagnostics or purifying/modifying them and re-transplanting them back into the patient for treatment of cancers and other blood and immune system disorders (Lagasse, Connors et al. 2000). The most widely used cell sorter is fluorescence-activated cell sorting (FACS) (Herzenberg, Parks et al. 2002), which can achieve multiplexed analysis and has a throughput of 50,000 cells/s. Targeting populations of cells that are present in really low numbers in the circulation system, though, has been challenging. An example of such cells are circulating tumor cells (CTCs). CTC levels in blood is an indication of tumor progressions and survival (Qian, Zhang et al. 2015). CTC detection is currently performed via CellSearch, which uses magnetic particles functionalized with antiepithelial cell adhesion molecule (EpCAM) (Riethdorf, Fritsche et al. 2007). Microfluidic devices have been recently developed containing chaotic and geometrically enhance differential immunocapture structures in combination with EpCAM antibodies that improve the capture efficiency (Nagrath, Sequist et al. 2007, Stott, Hsu et al. 2010, Smith, Lannin et al. 2014). CTCs, however, may have undergone EMT, which can downregulate the expression of epithelial markers (Yu, Bardia et al. 2013). Since CTCs have a larger diameter and are stiffer than leukocytes, multiple microfluidic devices have been developed to capture CTCs based on the physical differences between them and blood cells. Various devices utilize filtration, hydrodynamic force, inertial focusing, double spiral microchannels and magnetic separation structures that achieve high capture yield and throughput (Zheng, Lin et al. 2011, Sun, Li et al. 2012, Liu, Huang et al. 2013, Liu, Zhang et al. 2013, Ozkumur, Shah et al. 2013).

Another use of microfluidic devices is the isolation and purification of stem cells. High purity of stem cells is needed for treatment or prevention of diseases (stem cell therapy). Although FACS can isolate stem cells using biomarkers, it results low yields due to cell death. In order to achieve a high purity collection of stem cells with high survival, several microfluidic have been introduced. Singh and colleagues produced a microfluidic chip that takes advantage of the adhesions strength differences between undifferentiated and differentiated stem cells and yields human pluripotent stem cell populations with 95-99% purity and over 80% survival (Singh, Suri et al. 2013). In addition, micropost arrays have been embedded in microchips which can isolate cancer stem cells in populations that are flexible enough to navigate through (Zhang, Kai et al. 2012).

4.4 Microfluidics in cell migration

Microchambers which mimic live tissue topographical and biochemical cues have been used to study cell migration. Microfluidic devices allow the use of chemotactic gradients and are useful for high throughput screening of antimetastatic drugs (Zhang, Zhang et al. 2014). The study of rheotaxis, fluid flow induction of cell migration in the upstream direction, has been possible in a collagen I-based microfluidic hydrogel (Polacheck, German et al. 2014) and the study of intravasation is facilitated by microfluidic chips that allow for precise simulation of the endothelial barrier function (Bersini, Jeon et al. 2014). Another microfluidic device mimics the biophysical environment of the female reproductive tract and thus is used for the study of the migratory behavior of sperms and pathogens (Tung, Hu et al. 2015), where microgrooves facilitate sperm motility and prevent Tritrichomonas foetus migration.

4.5 Organ-on-chip applications

The culture and continuous perfusion of living cells in micrometer sized devices which recapitulate tissues and organs has been widely used in disease modeling and drug screening. Hydrogel-based methods and bioreactors have been used to create biomimetic designs of the liver, kidney, intestine, lung, heart, fat, bone, skin, cornea, nerve, bone marrow and blood vessels (Huh, Matthews et al. 2010, Bhatia and Ingber 2014, Torisawa, Spina et al. 2014, An, Qu et al. 2015). In addition, models of various diseases on-a-chip have been helpful in discovering new biomarkers of drug efficacy, toxicity and disease response (Huh, Leslie et al. 2012).

4.6 HEMICA: future directions

HEMICA is an affordable microfluidic device which mimics physiological tissue properties such as stiffness, water content, gas, water and macromolecule permeation. It allows high throughput experiments in an environment which can be highly controlled in order to present microchannels of high aspect ratio and stiffness anisotropy. It allows the establishment of chemotactic gradients, the study of collective, single and single cell-file migration as well as the use of various techniques (such as immunofluorescence, live-microscopy, confocal microscopy, FRET, TFM) for the characterization and investigation of cell behaviors. As HEMICA is assembled based on primary amine reactions, polyacrylamide can be substituted with a wide range of materials and proteins used for hydrogel production. Our experiments show that confined migration and 3D migration share multiple similarities. However, the breadth of the techniques supported by HEMICA, the cost and ease of its production, and its incorporation of microfluidics, make it a perfect

vessel for organ-on-a-chip applications. In addition, the low cell count required for microfluidic assays, the differential regulation of channel size and matrix stiffness, and the capability to be functionalized with an array of ligands, make HEMICA a promising candidate either as a personalized diagnostic tool or as a drug screening medium. It can incorporate the advantages of microfluidics in a physiologically relevant environment which is more appropriate for the growth and function of explanted cells. Thus, we are hopeful that HEMICA will serve researchers, clinicians and patients by opening new horizons in the fields of drug discovery, prevention and treatment.

BIBLIOGRAPHY

Abbenante, G. and D. P. Fairlie (2005). "Protease inhibitors in the clinic." Med Chem **1**(1): 71-104.

Agre, P. and D. Kozono (2003). "Aquaporin water channels: molecular mechanisms for human diseases." Febs Letters **555**(1): 72-78.

Alexander, S., G. E. Koehl, M. Hirschberg, E. K. Geissler and P. Friedl (2008). "Dynamic imaging of cancer growth and invasion: a modified skin-fold chamber model." Histochem Cell Biol **130**(6): 1147-1154.

Almany, L. and D. Seliktar (2005). "Biosynthetic hydrogel scaffolds made from fibrinogen and polyethylene glycol for 3D cell cultures." Biomaterials **26**(15): 2467-2477.

Ambravaneswaran, V., I. Y. Wong, A. J. Aranyosi, M. Toner and D. Irimia (2010). "Directional decisions during neutrophil chemotaxis inside bifurcating channels." Integr Biol (Camb) **2**(11-12): 639-647.

An, F., Y. Y. Qu, X. M. Liu, R. T. Zhong and Y. Luo (2015). "Organ-on-a-Chip: New Platform for Biological Analysis." Analytical Chemistry Insights **10**: 39-45.

Aydar, E., S. Yeo, M. Djamgoz and C. Palmer (2009). "Abnormal expression, localization and interaction of canonical transient receptor potential ion channels in human breast cancer cell lines and tissues: a potential target for breast cancer diagnosis and therapy." Cancer Cell International **9**.

Azimi, I., S. J. Roberts-Thomson and G. R. Monteith (2014). "Calcium influx pathways in breast cancer: opportunities for pharmacological intervention." Br J Pharmacol **171**(4): 945-960.

Balzer, E. M., Z. Tong, C. D. Paul, W. C. Hung, K. M. Stroka, A. E. Boggs, S. S. Martin and K. Konstantopoulos (2012). "Physical confinement alters tumor cell adhesion and migration phenotypes." FASEB J **26**(10): 4045-4056.

Batchelder, E. L., G. Hollopeter, C. Campillo, X. Mezanges, E. M. Jorgensen, P. Nassoy, P. Sens and J. Plastino (2011). "Membrane tension regulates motility by controlling lamellipodium organization." Proc Natl Acad Sci U S A **108**(28): 11429-11434.

Beaty, B. T., Y. R. Wang, J. J. Bravo-Cordero, V. P. Sharma, V. Miskolci, L. Hodgson and J. Condeelis (2014). "Talin regulates moesin-NHE-1 recruitment to invadopodia and promotes mammary tumor metastasis." Journal of Cell Biology **205**(5): 737-751.

Bergert, M., S. D. Chandradoss, R. A. Desai and E. Paluch (2012). "Cell mechanics control rapid transitions between blebs and lamellipodia during migration." Proc Natl Acad Sci U S A **109**(36): 14434-14439.

Bergert, M., A. Erzberger, R. A. Desai, I. M. Aspalter, A. C. Oates, G. Charras, G. Salbreux and E. K. Paluch (2015). "Force transmission during adhesion-independent migration." Nature Cell Biology **17**(4): 524-+.

Bersini, S., J. S. Jeon, G. Dubini, C. Arrigoni, S. Chung, J. L. Charest, M. Moretti and R. D. Kamm (2014). "A microfluidic 3D in vitro model for specificity of breast cancer metastasis to bone." Biomaterials **35**(8): 2454-2461.

Betapudi, V., V. Rai, J. R. Beach and T. Egelhoff (2010). "Novel regulation and dynamics of myosin II activation during epidermal wound responses." Experimental Cell Research **316**(6): 980-991.

Bhatia, S. N. and D. E. Ingber (2014). "Microfluidic organs-on-chips." Nature Biotechnology **32**(8): 760-772.

Bi, D., J. H. Lopez, J. M. Schwarz and M. L. Manning (2014). "Energy barriers and cell migration in densely packed tissues." Soft Matter **10**(12): 1885-1890.

Bomben, V. C., K. L. Turner, T. T. C. Barclay and H. Sontheimer (2011). "Transient Receptor Potential Canonical Channels Are Essential for Chemotactic Migration of Human Malignant Gliomas." Journal of Cellular Physiology **226**(7): 1879-1888.

Breckenridge, M. T., T. T. Egelhoff and H. Baskaran (2010). "A microfluidic imaging chamber for the direct observation of chemotactic transmigration." Biomed Microdevices **12**(3): 543-553.

Bryant, S. J., K. S. Anseth, D. A. Lee and D. L. Bader (2004). "Crosslinking density influences the morphology of chondrocytes photoencapsulated in PEG hydrogels during the application of compressive strain." J Orthop Res **22**(5): 1143-1149.

Campbell, R. L. and P. L. Davies (2012). "Structure-function relationships in calpains." Biochemical Journal **447**: 335-351.

Cao, Z. N., C. Y. Chen, B. He, K. Tan and C. Lu (2015). "A microfluidic device for epigenomic profiling using 100 cells." Nature Methods **12**(10): 959-962.

Carey, S. P., C. M. Kraning-Rush, R. M. Williams and C. A. Reinhart-King (2012). "Biophysical control of invasive tumor cell behavior by extracellular matrix microarchitecture." Biomaterials **33**(16): 4157-4165.

Carragher, N. O., S. M. Walker, L. S. A. Carragher, F. Harris, T. K. Sawyer, V. G. Brunton, B. W. Ozanne and M. C. Frame (2006). "Calpain 2 and Src dependence distinguishes mesenchymal and amoeboid modes of tumour cell invasion: a link to integrin function." Oncogene **25**(42): 5726-5740.

Chang, S. S., W. H. Guo, Y. Kim and Y. L. Wang (2013). "Guidance of cell migration by substrate dimension." Biophys J **104**(2): 313-321.

Charras, G. T., C. K. Hu, M. Coughlin and T. J. Mitchison (2006). "Reassembly of contractile actin cortex in cell blebs." J Cell Biol **175**(3): 477-490.

Charras, G. T., J. C. Yarrow, M. A. Horton, L. Mahadevan and T. J. Mitchison (2005). "Non-equilibration of hydrostatic pressure in blebbing cells." Nature **435**(7040): 365-369.

Chen, J. P., Y. Luan, C. X. You, X. H. Chen, R. C. Luo and R. Li (2010). "TRPM7 regulates the migration of human nasopharyngeal carcinoma cell by mediating Ca2+ influx." Cell Calcium **47**(5): 425-432.

Chen, S. H., W. C. Hung, P. Wang, C. Paul and K. Konstantopoulos (2013). "Mesothelin binding to CA125/MUC16 promotes pancreatic cancer cell motility and invasion via MMP-7 activation." Sci Rep **3**: 1870.

Chew, S. Y., R. Mi, A. Hoke and K. W. Leong (2008). "The effect of the alignment of electrospun fibrous scaffolds on Schwann cell maturation." Biomaterials **29**(6): 653-661.

Chiang, Y. H., C. Y. Chou, K. F. Hsu, Y. F. Huang and M. R. Shen (2008). "EGF upregulates Na+/H+ exchanger NHE1 by post-translational regulation that is important for cervical cancer cell invasiveness." Journal of Cellular Physiology **214**(3): 810-819.

Chicurel, M. E., C. S. Chen and D. E. Ingber (1998). "Cellular control lies in the balance of forces." Current Opinion in Cell Biology **10**(2): 232-239.

Chin, C. D., T. Laksanasopin, Y. K. Cheung, D. Steinmiller, V. Linder, H. Parsa, J. Wang, H. Moore, R. Rouse, G. Umviligihozo, E. Karita, L. Mwambarangwe, S. L. Braunstein, J. van de Wijgert, R. Sahabo, J. E. Justman, W. El-Sadr and S. K. Sia (2011). "Microfluidics-based diagnostics of infectious diseases in the developing world." Nature Medicine **17**(8): 1015-U1138.

Christopherson, G. T., H. Song and H. Q. Mao (2009). "The influence of fiber diameter of electrospun substrates on neural stem cell differentiation and proliferation." Biomaterials **30**(4): 556-564.

Clark, K., J. Middelbeek and F. N. van Leeuwen (2008). "Interplay between TRP channels and the cytoskeleton in health and disease." Eur J Cell Biol **87**(8-9): 631-640.

Crescenzi, V., L. Cornelio, C. Di Meo, S. Nardecchia and R. Lamanna (2007). "Novel hydrogels via click chemistry: Synthesis and potential biomedical applications." Biomacromolecules **8**(6): 1844-1850.

Cruse, G., S. M. Duffy, C. E. Brightling and P. Bradding (2006). "Functional K(Ca)3.1 K+ channels are required for human lung mast cell migration." Thorax **61**(10): 880-885.

Cuddapah, V. A. and H. Sontheimer (2010). "Molecular Interaction and Functional Regulation of ClC-3 by Ca2+/Calmodulin-dependent Protein Kinase II (CaMKII) in Human Malignant Glioma." Journal of Biological Chemistry **285**(15): 11188-11196.

Cuddapah, V. A., K. L. Turner, S. Seifert and H. Sontheimer (2013). "Bradykinin-induced chemotaxis of human gliomas requires the activation of KCa3.1 and ClC-3." J Neurosci **33**(4): 1427-1440.

Danielsen, E. M. and G. H. Hansen (2016). "Small molecule pinocytosis and clathrin-dependent endocytosis at the intestinal brush border: Two separate pathways into the enterocyte." Biochimica Et Biophysica Acta-Biomembranes **1858**(2): 233-243.

Deakin, N. O. and C. E. Turner (2011). "Distinct roles for paxillin and Hic-5 in regulating breast cancer cell morphology, invasion, and metastasis." Molecular Biology of the Cell **22**(3): 327-341.

DeForest, C. A. and K. S. Anseth (2011). "Cytocompatible click-based hydrogels with dynamically tunable properties through orthogonal photoconjugation and photocleavage reactions." Nature Chemistry **3**(12): 925-931.

Dembo, M. and Y.-L. Wang (1999). "Stresses at the Cell-to-Substrate Interface during Locomotion of Fibroblasts." Biophysical Journal **76**(4): 2307-2316.

Denais, C. M., R. M. Gilbert, P. Isermann, A. L. McGregor, M. te Lindert, B. Weigelin, P. M. Davidson, P. Friedl, K. Wolf and J. Lammerding (2016). "Nuclear envelope rupture and repair during cancer cell migration." Science **352**(6283): 353-358.

Denk, W., J. H. Strickler and W. W. Webb (1990). "2-Photon Laser Scanning Fluorescence Microscopy." Science **248**(4951): 73-76.

Denker, S. P. and D. L. Barber (2002). "Cell migration requires both ion translocation and cytoskeletal anchoring by the Na-H exchanger NHE1." Journal of Cell Biology **159**(6): 1087-1096.

Dhennin-Duthille, I., M. Gautier, M. Faouzi, A. Guilbert, M. Brevet, D. Vaudry, A. Ahidouch, H. Sevestre and H. Ouadid-Ahidouch (2011). "High Expression of Transient Receptor Potential Channels in Human Breast Cancer Epithelial Cells and Tissues: Correlation with Pathological Parameters." Cellular Physiology and Biochemistry **28**(5): 813-822.

Discher, D. E., P. Janmey and Y. L. Wang (2005). "Tissue cells feel and respond to the stiffness of their substrate." Science **310**(5751): 1139-1143.

Diz-Munoz, A., D. A. Fletcher and O. D. Weiner (2013). "Use the force: membrane tension as an organizer of cell shape and motility." Trends in Cell Biology **23**(2): 47-53.

Diz-Munoz, A., M. Krieg, M. Bergert, I. Ibarlucea-Benitez, D. J. Muller, E. Paluch and C. P. Heisenberg (2010). "Control of directed cell migration in vivo by membrane-to-cortex attachment." PLoS Biol **8**(11): e1000544.

Dou, Y. L., Y. Li, J. K. Chen, S. H. Wu, X. Xiao, S. S. Xie, L. P. Tang, M. Yan, Y. Q. Wang, J. Lin, W. B. Zhu and G. M. Yan (2013). "Inhibition of cancer cell proliferation by midazolam by targeting transient receptor potential melastatin 7." Oncology Letters **5**(3): 1010-1016.

Doyle, A. D., F. W. Wang, K. Matsumoto and K. M. Yamada (2009). "One-dimensional topography underlies three-dimensional fibrillar cell migration." Journal of Cell Biology **184**(4): 481-490.

Duffy, D. C., J. C. McDonald, O. J. Schueller and G. M. Whitesides (1998). "Rapid Prototyping of Microfluidic Systems in Poly(dimethylsiloxane)." Anal Chem **70**(23): 4974-4984.

Eddy, R. J., L. M. Pierini, F. Matsumura and F. R. Maxfield (2000). "Ca2+-dependent myosin II activation is required for uropod retraction during neutrophil migration." Journal of Cell Science **113**(7): 1287-1298.

Egeblad, M., E. S. Nakasone and Z. Werb (2010). "Tumors as Organs: Complex Tissues that Interface with the Entire Organism." Developmental Cell **18**(6): 884-901.

Engler, A. J., S. Sen, H. L. Sweeney and D. E. Discher (2006). "Matrix elasticity directs stem cell lineage specification." Cell **126**(4): 677-689.

Enyedi, B., M. Jelcic and P. Niethammer (2016). "The Cell Nucleus Serves as a Mechanotransducer of Tissue Damage-Induced Inflammation." Cell **165**(5): 1160-1170.

Espinosa-Tanguma, R., C. O'Neil, T. Chrones, J. G. Pickering and S. M. Sims (2011). "Essential role for calcium waves in migration of human vascular smooth muscle cells." American Journal of Physiology-Heart and Circulatory Physiology **301**(2): H315-H323.

Estecha, A., L. Sanchez-Martin, A. Puig-Kroger, R. A. Bartolome, J. Teixido, R. Samaniego and P. Sanchez-Mateos (2009). "Moesin orchestrates cortical polarity

of melanoma tumour cells to initiate 3D invasion." J Cell Sci **122**(Pt 19): 3492-3501.

Fabian, A., T. Fortmann, E. Bulk, V. C. Bomben, H. Sontheimer and A. Schwab (2011). "Chemotaxis of MDCK-F cells toward fibroblast growth factor-2 depends on transient receptor potential canonical channel 1." Pflugers Archiv-European Journal of Physiology **461**(2): 295-306.

Ferguson, B. S., S. F. Buchsbaum, T. T. Wu, K. Hsieh, Y. Xiao, R. Sun and H. T. Soh (2011). "Genetic Analysis of H1N1 Influenza Virus from Throat Swab Samples in a Microfluidic System for Point-of-Care Diagnostics." Journal of the American Chemical Society **133**(23): 9129-9135.

Friedl, P. and S. Alexander (2011). "Cancer invasion and the microenvironment: plasticity and reciprocity." Cell **147**(5): 992-1009.

Friedl, P. and K. Wolf (2003). "Proteolytic and non-proteolytic migration of tumour cells and leucocytes." Biochem Soc Symp(70): 277-285.

Friedl, P. and K. Wolf (2009). "Proteolytic interstitial cell migration: a five-step process." Cancer Metastasis Rev **28**(1-2): 129-135.

Fuerstman, M. J., A. Lai, M. E. Thurlow, S. S. Shevkoplyas, H. A. Stone and G. M. Whitesides (2007). "The pressure drop along rectangular microchannels containing bubbles." Lab Chip **7**(11): 1479-1489.

Gaggioli, C., S. Hooper, C. Hidalgo-Carcedo, R. Grosse, J. F. Marshall, K. Harrington and E. Sahai (2007). "Fibroblast-led collective invasion of carcinoma cells with differing roles for RhoGTPases in leading and following cells." Nat Cell Biol **9**(12): 1392-1400.

Ganji, F., S. Vasheghani-Farahani and E. Vasheghani-Farahani (2010). "Theoretical Description of Hydrogel Swelling: A Review." Iranian Polymer Journal **19**(5): 375-398.

Gao, H. X., X. J. Chen, X. N. Du, B. C. Guan, Y. N. Liu and H. L. Zhang (2011). "EGF enhances the migration of cancer cells by up-regulation of TRPM7." Cell Calcium **50**(6): 559-568.

Giannone, G., P. Ronde, M. Gaire, J. Beaudouin, J. Haiech, J. Ellenberg and K. Takeda (2004). "Calcium rises locally trigger focal adhesion disassembly and enhance residency of focal adhesion kinase at focal adhesions." Journal of Biological Chemistry **279**(27): 28715-28723.

Giannone, G., P. Ronde, M. Gaire, J. Haiech and K. Takeda (2002). "Calcium oscillations trigger focal adhesion disassembly in human U87 astrocytoma cells." Journal of Biological Chemistry **277**(29): 26364-26371.

Golatta, M., M. Schweitzer-Martin, A. Harcos, S. Schott, H. Junkermann, G. Rauch, C. Sohn and J. Heil (2013). "Normal breast tissue stiffness measured by a new ultrasound technique: virtual touch tissue imaging quantification (VTIQ)." Eur J Radiol **82**(11): e676-679.

Griffin, M. A., S. Sen, H. L. Sweeney and D. E. Discher (2004). "Adhesion-contractile balance in myocyte differentiation." Journal of Cell Science **117**(24): 5855-5863.

Haas, B. R. and H. Sontheimer (2010). "Inhibition of the Sodium-Potassium-Chloride Cotransporter Isoform-1 Reduces Glioma Invasion." Cancer Research **70**(13): 5597-5606.

Hahn, K., R. Debiasio and D. L. Taylor (1992). "Patterns of Elevated Free Calcium and Calmodulin Activation in Living Cells." Nature **359**(6397): 736-738.

Hahn, M. S., J. S. Miller and J. L. West (2006). "Three-dimensional biochemical and biomechanical patterning of hydrogels for guiding cell behavior." Advanced Materials **18**(20): 2679-+.

Hanano, T., Y. Hara, J. Shi, H. Morita, C. Umebayashi, E. Mori, H. Sumimoto, Y. Ito, Y. Mori and R. Inoue (2004). "Involvement of TRPM7 in cell growth as a spontaneously activated Ca2+ entry pathway in human retinoblastoma cells." Journal of Pharmacological Sciences **95**(4): 403-419.

Harrison V. Prentice-Motta, b., c,d, Chi-Han Changa,b,c,e, L. Mahadevanf, Timothy J. Mitchisona, Daniel Irimiag, and Jagesh V. Shaha,b,c,1 (2013). "Biased migration of confined neutrophil-like cells in asymmetric hydraulic environments." PNAS.

Hawkins, R. J., M. Piel, G. Faure-Andre, A. M. Lennon-Dumenil, J. F. Joanny, J. Prost and R. Voituriez (2009). "Pushing off the walls: a mechanism of cell motility in confinement." Phys Rev Lett **102**(5): 058103.

Hayashi, H., O. Aharonovitz, R. T. Alexander, N. Touret, W. Furuya, J. Orlowski and S. Grinstein (2008). "Na+/H+ exchange and pH regulation in the control of neutrophil chemokinesis and chemotaxis." American Journal of Physiology-Cell Physiology **294**(2): C526-C534.

He, L., W. Chen, P.-H. Wu, A. Jimenez, B. S. Wong, A. San, K. Konstantopoulos and D. Wirtz (2016). "Local 3D matrix confinement determines division axis through cell shape." Oncotarget **7**(6): 6994-7011.

Herzenberg, L. A., D. Parks, B. Sahaf, O. Perez, M. Roederer and L. A. Herzenberg (2002). "The history and future of the fluorescence activated cell sorter and flow cytometry: A view from Stanford." Clinical Chemistry **48**(10): 1819-1827.

Heuze, M. L., O. Collin, E. Terriac, A. M. Lennon-Dumenil and M. Piel (2011). "Cell migration in confinement: a micro-channel-based assay." Methods Mol Biol **769**: 415-434.

Hong, Y., H. Song, Y. Gong, Z. Mao, C. Gao and J. Shen (2007). "Covalently crosslinked chitosan hydrogel: properties of in vitro degradation and chondrocyte encapsulation." Acta Biomater **3**(1): 23-31.

Hoshikawa, A., Y. Nakayama, T. Matsuda, H. Oda, K. Nakamura and K. Mabuchi (2006). "Encapsulation of chondrocytes in photopolymerizable styrenated gelatin for cartilage tissue engineering." Tissue Eng **12**(8): 2333-2341.

Houk, A. R., A. Jilkine, C. O. Mejean, R. Boltyanskiy, E. R. Dufresne, S. B. Angenent, S. J. Altschuler, L. F. Wu and O. D. Weiner (2012). "Membrane tension maintains cell polarity by confining signals to the leading edge during neutrophil migration." Cell **148**(1-2): 175-188.

Huang, Y. J., J. Samorajski, R. Kreimer and P. C. Searson (2013). "The influence of electric field and confinement on cell motility." PLoS One **8**(3): e59447.

Huh, D., D. C. Leslie, B. D. Matthews, J. P. Fraser, S. Jurek, G. A. Hamilton, K. S. Thorneloe, M. A. McAlexander and D. E. Ingber (2012). "A Human Disease Model of Drug Toxicity-Induced Pulmonary Edema in a Lung-on-a-Chip Microdevice." Science Translational Medicine **4**(159).

Huh, D., B. D. Matthews, A. Mammoto, M. Montoya-Zavala, H. Y. Hsin and D. E. Ingber (2010). "Reconstituting Organ-Level Lung Functions on a Chip." Science **328**(5986): 1662-1668.

Hung, W. C., S. H. Chen, C. D. Paul, K. M. Stroka, Y. C. Lo, J. T. Yang and K. Konstantopoulos (2013). "Distinct signaling mechanisms regulate migration in unconfined versus confined spaces." Journal of Cell Biology **202**(5): 807-824.

Hung, W. C., J. R. Yang, C. L. Yankaskas, B. S. Wong, P. H. Wu, C. Pardo-Pastor, S. A. Serra, M. J. Chiang, Z. Z. Gu, D. Wirtz, M. A. Valverde, J. T. Yang, J. Zhang and K. Konstantopoulos (2016). "Confinement Sensing and Signal Optimization via Piezo1/PKA and Myosin II Pathways." Cell Reports **15**(7): 1430-1441.

Ilina, O., G. J. Bakker, A. Vasaturo, R. M. Hofmann and P. Friedl (2011). "Two-photon laser-generated microtracks in 3D collagen lattices: principles of MMP-dependent and -independent collective cancer cell invasion." Phys Biol **8**(1): 015010.

Ioannis K. Zervantonakis, S. C., Ryo Sudo, Mengwen Zhang, Joseph L. Charest and Roger D. Kamm (2010). "Concentration gradients in microfluidic 3D matrix cell culture systems." International Journal of Micro-Nano Scale Transport **1**: 27-36.

Irimia, D., G. Charras, N. Agrawal, T. Mitchison and M. Toner (2007). "Polar stimulation and constrained cell migration in microfluidic channels." Lab Chip **7**(12): 1783-1790.

Irimia, D. and M. Toner (2009). "Spontaneous migration of cancer cells under conditions of mechanical confinement." Integr Biol (Camb) **1**(8-9): 506-512.

Jones, C. and H. P. Ehrlich (2011). "Fibroblast expression of alpha-smooth muscle actin, alpha2beta1 integrin and alphavbeta3 integrin: influence of surface rigidity." Exp Mol Pathol **91**(1): 394-399.

Junkin, M. and P. K. Wong (2011). "Probing cell migration in confined environments by plasma lithography." Biomaterials **32**(7): 1848-1855.

Kassianidou, E. and S. Kumar (2015). "A biomechanical perspective on stress fiber structure and function." Biochimica Et Biophysica Acta-Molecular Cell Research **1853**(11): 3065-3074.

Keren, K., Z. Pincus, G. M. Allen, E. L. Barnhart, G. Marriott, A. Mogilner and J. A. Theriot (2008). "Mechanism of shape determination in motile cells." Nature **453**(7194): 475-480.

Kim, B. J., E. J. Park, J. H. Lee, J. H. Jeon, S. J. Kim and I. So (2008). "Suppression of transient receptor potential melastatin 7 channel induces cell death in gastric cancer." Cancer Science **99**(12): 2502-2509.

Kim, D. H. and D. Wirtz (2013). "Focal adhesion size uniquely predicts cell migration." FASEB J **27**(4): 1351-1361.

Kloxin, A. M., A. M. Kasko, C. N. Salinas and K. S. Anseth (2009). "Photodegradable hydrogels for dynamic tuning of physical and chemical properties." Science **324**(5923): 59-63.

Kraning-Rush, C. M., S. P. Carey, M. C. Lampi and C. A. Reinhart-King (2013). "Microfabricated collagen tracks facilitate single cell metastatic invasion in 3D." Integr Biol (Camb) **5**(3): 606-616.

Krapivinsky, G., S. Mochida, L. Krapivinsky, S. M. Cibulsky and D. E. Clapham (2006). "The TRPM7 ion channel functions in cholinergic synaptic vesicles and affects transmitter release." Neuron **52**(3): 485-496.

Krouskop, T. A., T. M. Wheeler, F. Kallel, B. S. Garra and T. Hall (1998). "Elastic moduli of breast and prostate tissues under compression." Ultrason Imaging **20**(4): 260-274.

Kuntz, R. M. and W. M. Saltzman (1997). "Neutrophil motility in extracellular matrix gels: mesh size and adhesion affect speed of migration." Biophys J **72**(3): 1472-1480.

Lagana, A., J. Vadnais, P. U. Le, T. N. Nguyen, R. Laprade, I. R. Nabi and J. Noel (2000). "Regulation of the formation of tumor cell pseudopodia by the Na+/H+ exchanger NHE1." Journal of Cell Science **113**(20): 3649-3662.

Lagarrigue, E., D. Ternent, S. K. Maciver, A. Fattoum, Y. Benyamin and C. Roustan (2003). "The activation of gelsolin by low pH - The calcium latch is sensitive to calcium but not pH." European Journal of Biochemistry **270**(20): 4105-4112.

Lagasse, E., H. Connors, M. Al-Dhalimy, M. Reitsma, M. Dohse, L. Osborne, X. Wang, M. Finegold, I. L. Weissman and M. Grompe (2000). "Purified hematopoietic stem cells can differentiate into hepatocytes in vivo." Nature Medicine **6**(11): 1229-1234.

Laksanasopin, T., T. W. Guo, S. Nayak, A. A. Sridhara, S. Xie, O. O. Olowookere, P. Cadinu, F. X. Meng, N. H. Chee, J. Kim, C. D. Chin, E. Munyazesa, P. Mugwaneza, A. J. Rai, V. Mugisha, A. R. Castro, D. Steinmiller, V. Linder, J. E. Justman, S. Nsanzimana and S. K. Sia (2015). "A smartphone dongle for

diagnosis of infectious diseases at the point of care." Science Translational Medicine **7**(273).

Lammermann, T., B. L. Bader, S. J. Monkley, T. Worbs, R. Wedlich-Soldner, K. Hirsch, M. Keller, R. Forster, D. R. Critchley, R. Fassler and M. Sixt (2008). "Rapid leukocyte migration by integrin-independent flowing and squeezing." Nature **453**(7191): 51-+.

Lammermann, T. and M. Sixt (2009). "Mechanical modes of 'amoeboid' cell migration." Curr Opin Cell Biol **21**(5): 636-644.

Lautscham, L. A., C. Kammerer, J. R. Lange, T. Kolb, C. Mark, A. Schilling, P. L. Strissel, R. Strick, C. Gluth, A. C. Rowat, C. Metzner and B. Fabry (2015). "Migration in Confined 3D Environments Is Determined by a Combination of Adhesiveness, Nuclear Volume, Contractility, and Cell Stiffness." Biophys J **109**(5): 900-913.

Le Berre, M., J. Aubertin and M. Piel (2012). "Fine control of nuclear confinement identifies a threshold deformation leading to lamina rupture and induction of specific genes." Integrative Biology **4**(11): 1406-1414.

Le Clainche, C. and M. F. Carlier (2008). "Regulation of actin assembly associated with protrusion and adhesion in cell migration." Physiological Reviews **88**(2): 489-513.

Lee, J., A. Ishihara, G. Oxford, B. Johnson and K. Jacobson (1999). "Regulation of cell movement is mediated by stretch-activated calcium channels." Nature **400**(6742): 382-386.

Lee, L. M. and A. P. Liu (2015). "A microfluidic pipette array for mechanophenotyping of cancer cells and mechanical gating of mechanosensitive channels." Lab Chip **15**(1): 264-273.

Lee, S. H., J. J. Moon and J. L. West (2008). "Three-dimensional micropatterning of bioactive hydrogels via two-photon laser scanning photolithography for guided 3D cell migration." Biomaterials **29**(20): 2962-2968.

Lei, K. F., C. H. Huang, R. L. Kuo, C. K. Chang, K. F. Chen, K. C. Tsao and N. M. Tsang (2015). "Paper-based enzyme-free immunoassay for rapid detection and subtyping of influenza A H1N1 and H3N2 viruses." Analytica Chimica Acta **883**: 37-44.

Li, Q., J. Wang, S. Shahani, D. D. N. Sun, B. Sharma, J. H. Elisseeff and K. W. Leong (2006). "Biodegradable and photocrosslinkable polyphosphoester hydrogel." Biomaterials **27**(7): 1027-1034.

Li, Q., C. G. Williams, D. D. Sun, J. Wang, K. Leong and J. H. Elisseeff (2004). "Photocrosslinkable polysaccharides based on chondroitin sulfate." J Biomed Mater Res A **68**(1): 28-33.

Li, Y., J. Xuan, T. Xia, X. Han, Y. J. Song, Z. Cao, X. Jiang, Y. Guo, P. Wang and L. D. Qin (2015). "Competitive Volumetric Bar-Chart Chip with Real-Time Internal Control for Point-of-Care Diagnostics." Analytical Chemistry **87**(7): 3771-3777.

Lieber, A. D., S. Yehudai-Resheff, E. L. Barnhart, J. A. Theriot and K. Keren (2013). "Membrane tension in rapidly moving cells is determined by cytoskeletal forces." Curr Biol **23**(15): 1409-1417.

Liu, Y. J., M. Le Berre, F. Lautenschlaeger, P. Maiuri, A. Callan-Jones, M. Heuze, T. Takaki, R. Voituriez and M. Piel (2015). "Confinement and Low Adhesion Induce Fast Amoeboid Migration of Slow Mesenchymal Cells." Cell **160**(4): 659-672.

Liu, Z. B., F. Huang, J. H. Du, W. L. Shu, H. T. Feng, X. P. Xu and Y. Chen (2013). "Rapid isolation of cancer cells using microfluidic deterministic lateral displacement structure." Biomicrofluidics **7**(1).

Liu, Z. B., W. Zhang, F. Huang, H. T. Feng, W. L. Shu, X. P. Xu and Y. Chen (2013). "High throughput capture of circulating tumor cells using an integrated microfluidic system." Biosensors & Bioelectronics **47**: 113-119.

Loitto, V. M., C. Huang, Y. J. Sigal and K. Jacobson (2007). "Filopodia are induced by aquaporin-9 expression." Experimental Cell Research **313**(7): 1295-1306.

Lorentzen, A., J. Bamber, A. Sadok, I. Elson-Schwab and C. J. Marshall (2011). "An ezrin-rich, rigid uropod-like structure directs movement of amoeboid blebbing cells." J Cell Sci **124**(Pt 8): 1256-1267.

Mak, M. and D. Erickson (2014). "Mechanical decision trees for investigating and modulating single-cell cancer invasion dynamics." Lab Chip **14**(5): 964-971.

Malkoch, M., R. Vestberg, N. Gupta, L. Mespouille, P. Dubois, A. F. Mason, J. L. Hedrick, Q. Liao, C. W. Frank, K. Kingsbury and C. J. Hawker (2006). "Synthesis of well-defined hydrogel networks using Click chemistry." Chemical Communications(26): 2774-2776.

Matheu, M. P., C. Beeton, A. Garcia, V. Chi, S. Rangaraju, O. Safrina, K. Monaghan, M. I. Uemura, D. Li, S. Pal, L. M. de la Maza, E. Monuki, A. Flugel, M. W. Pennington, I. Parker, K. G. Chandy and M. D. Cahalan (2008). "Imaging of

Effector Memory T Cells during a Delayed-Type Hypersensitivity Reaction and Suppression by Kv1.3 Channel Block." Immunity **29**(4): 602-614.

McHale, M. K., L. A. Setton and A. Chilkoti (2005). "Synthesis and in vitro evaluation of enzymatically cross-linked elastin-like polypeptide gels for cartilaginous tissue repair." Tissue Eng **11**(11-12): 1768-1779.

Mehlen, P. and A. Puisieux (2006). "Metastasis: a question of life or death." Nat Rev Cancer **6**(6): 449-458.

Meijering, E., O. Dzyubachyk and I. Smal (2012). "Methods for cell and particle tracking." Methods Enzymol **504**: 183-200.

Mih, J. D., A. Marinkovic, F. Liu, A. S. Sharif and D. J. Tschumperlin (2012). "Matrix stiffness reverses the effect of actomyosin tension on cell proliferation." J Cell Sci **125**(Pt 24): 5974-5983.

Monteith, G. R., N. Prevarskaya and S. J. Roberts-Thomson (2017). "The calcium-cancer signalling nexus." Nature Reviews Cancer **17**(6): 367-380.

Murphy, C. M. and F. J. O'Brien (2010). "Understanding the effect of mean pore size on cell activity in collagen-glycosaminoglycan scaffolds." Cell Adh Migr **4**(3): 377-381.

Nadler, M. J. S., M. C. Hermosura, K. Inabe, A. L. Perraud, Q. Q. Zhu, A. J. Stokes, T. Kurosaki, J. P. Kinet, R. Penner, A. M. Scharenberg and A. Fleig (2001). "LTRPC7 is a Mg center dot ATP-regulated divalent cation channel required for cell viability (vol 411, pg 590, 2001)." Nature **412**(6847): 660-660.

Nagrath, S., L. V. Sequist, S. Maheswaran, D. W. Bell, D. Irimia, L. Ulkus, M. R. Smith, E. L. Kwak, S. Digumarthy, A. Muzikansky, P. Ryan, U. J. Balis, R. G.

Tompkins, D. A. Haber and M. Toner (2007). "Isolation of rare circulating tumour cells in cancer patients by microchip technology." Nature **450**(7173): 1235-U1210.

Narumiya, S. and S. Yasuda (2006). "Rho GTPases in animal cell mitosis." Current Opinion in Cell Biology **18**(2): 199-205.

Netti, P. A., D. A. Berk, M. A. Swartz, A. J. Grodzinsky and R. K. Jain (2000). "Role of extracellular matrix assembly in interstitial transport in solid tumors." Cancer Res **60**(9): 2497-2503.

Nge, P. N., C. I. Rogers and A. T. Woolley (2013). "Advances in Microfluidic Materials, Functions, Integration, and Applications." Chemical Reviews **113**(4): 2550-2583.

On Shun Pak, Y.-N. Y., Gary R. Marple, Shravan Veerapaneni, and Howard A. Stone (2015). "Gating of a mechanosensitive channel due to cellular flows." Proc Natl Acad Sci U S A **112**(32): 9822-9827.

Ossipov, D. A. and J. Hilborn (2006). "Poly(vinyl alcohol)-based hydrogels formed by "click chemistry"." Macromolecules **39**(5): 1709-1718.

Ouadid-Ahidouch, H., I. Dhennin-Duthille, M. Gautier, H. Sevestre and A. Ahidouch (2013). "TRP channels: diagnostic markers and therapeutic targets for breast cancer?" Trends in Molecular Medicine **19**(2): 117-124.

Ozkumur, E., A. M. Shah, J. C. Ciciliano, B. L. Emmink, D. T. Miyamoto, E. Brachtel, M. Yu, P. I. Chen, B. Morgan, J. Trautwein, A. Kimura, S. Sengupta, S. L. Stott, N. M. Karabacak, T. A. Barber, J. R. Walsh, K. Smith, P. S. Spuhler, J. P. Sullivan, R. J. Lee, D. T. Ting, X. Luo, A. T. Shaw, A. Bardia, L. V. Sequist, D. N. Louis, S. Maheswaran, R. Kapur, D. A. Haber and M. Toner (2013). "Inertial

Focusing for Tumor Antigen-Dependent and -Independent Sorting of Rare Circulating Tumor Cells." Science Translational Medicine **5**(179).

Papadopoulos, M. C. and S. Saadoun (2015). "Key roles of aquaporins in tumor biology." Biochim Biophys Acta **1848**(10 Pt B): 2576-2583.

Papadopoulos, M. C., S. Saadoun and A. S. Verkman (2008). "Aquaporins and cell migration." Pflugers Archiv-European Journal of Physiology **456**(4): 693-700.

Park, T. G. and A. S. Hoffman (1992). "Synthesis and Characterization of Ph- and or Temperature-Sensitive Hydrogels." Journal of Applied Polymer Science **46**(4): 659-671.

Pathak, A. and S. Kumar (2012). "Independent regulation of tumor cell migration by matrix stiffness and confinement." Proc Natl Acad Sci U S A **109**(26): 10334-10339.

Paul, C. D., D. J. Shea, M. R. Mahoney, A. Chai, V. Laney, W. C. Hung and K. Konstantopoulos (2016). "Interplay of the physical microenvironment, contact guidance, and intracellular signaling in cell decision making." FASEB J **30**(6): 2161-2170.

Pedersen, S. F., E. K. Hoffmann and I. Novak (2013). "Cell volume regulation in epithelial physiology and cancer." Front Physiol **4**: 233.

Pelham, R. J., Jr. and Y. Wang (1997). "Cell locomotion and focal adhesions are regulated by substrate flexibility." Proc Natl Acad Sci U S A **94**(25): 13661-13665.

Petrie, R. J., A. D. Doyle and K. M. Yamada (2009). "Random versus directionally persistent cell migration." Nat Rev Mol Cell Biol **10**(8): 538-549.

Petrie, R. J., N. Gavara, R. S. Chadwick and K. M. Yamada (2012). "Nonpolarized signaling reveals two distinct modes of 3D cell migration." J Cell Biol **197**(3): 439-455.

Petrie, R. J., H. Koo and K. M. Yamada (2014). "Generation of compartmentalized pressure by a nuclear piston governs cell motility in a 3D matrix." Science **345**(6200): 1062-1065.

Petrie, R. J. and K. M. Yamada (2012). "At the leading edge of three-dimensional cell migration." Journal of Cell Science **125**(24): 5917-5926.

Plotnikov, S. V., A. M. Pasapera, B. Sabass and C. M. Waterman (2012). "Force fluctuations within focal adhesions mediate ECM-rigidity sensing to guide directed cell migration." Cell **151**(7): 1513-1527.

Pluen, A., Y. Boucher, S. Ramanujan, T. D. McKee, T. Gohongi, E. di Tomaso, E. B. Brown, Y. Izumi, R. B. Campbell, D. A. Berk and R. K. Jain (2001). "Role of tumor-host interactions in interstitial diffusion of macromolecules: Cranial vs. subcutaneous tumors." Proceedings of the National Academy of Sciences of the United States of America **98**(8): 4628-4633.

Polacheck, W. J., A. E. German, A. Mammoto, D. E. Ingber and R. D. Kamm (2014). "Mechanotransduction of fluid stresses governs 3D cell migration." Proceedings of the National Academy of Sciences of the United States of America **111**(7): 2447-2452.

Polizzotti, B. D., B. D. Fairbanks and K. S. Anseth (2008). "Three-dimensional biochemical patterning of click-based composite hydrogels via thiolene photopolymerization." Biomacromolecules **9**(4): 1084-1087.

Pollard, T. D. and G. G. Borisy (2003). "Cellular motility driven by assembly and disassembly of actin filaments (vol 112, pg 453, 2002)." Cell **113**(4): 549-549.

Prevarskaya, N., R. Skryma and Y. Shuba (2011). "Calcium in tumour metastasis: new roles for known actors." Nat Rev Cancer **11**(8): 609-618.

Provenzano, P. P., K. W. Eliceiri, J. M. Campbell, D. R. Inman, J. G. White and P. J. Keely (2006). "Collagen reorganization at the tumor-stromal interface facilitates local invasion." Bmc Medicine **4**.

Qian, B., Y. Deng, J. H. Im, R. J. Muschel, Y. Zou, J. Li, R. A. Lang and J. W. Pollard (2009). "A distinct macrophage population mediates metastatic breast cancer cell extravasation, establishment and growth." PLoS One **4**(8): e6562.

Qian, W. Y., Y. Zhang and W. Q. Chen (2015). "Capturing Cancer: Emerging Microfluidic Technologies for the Capture and Characterization of Circulating Tumor Cells." Small **11**(32): 3850-3872.

Qin, X., Z. C. Yue, B. N. Sun, W. Z. Yang, J. Xie, E. Ni, Y. Feng, R. Mahmood, Y. H. Zhang and L. X. Yue (2013). "Sphingosine and FTY720 are potent inhibitors of the transient receptor potential melastatin 7 (TRPM7) channels." British Journal of Pharmacology **168**(6): 1294-1312.

Raab, M. (2016). "ESCRT III repairs nuclear envelope ruptures during cell migration to limit DNA damage and cell death (vol 353, aah6167, 2016)." Science **353**(6307): 1507-1507.

Raman, P. S., C. D. Paul, K. M. Stroka and K. Konstantopoulos (2013). "Probing cell traction forces in confined microenvironments." Lab Chip **13**(23): 4599-4607.

Ran, F. A., P. D. Hsu, J. Wright, V. Agarwala, D. A. Scott and F. Zhang (2013). "Genome engineering using the CRISPR-Cas9 system." Nature Protocols **8**(11): 2281-2308.

Raucher, D. and M. P. Sheetz (2000). "Cell spreading and lamellipodial extension rate is regulated by membrane tension." Journal of Cell Biology **148**(1): 127-136.

Reinholt, S. J. and A. J. Baeumner (2014). "Microfluidic Isolation of Nucleic Acids." Angewandte Chemie-International Edition **53**(51): 13988-14001.

Reshkin, S. J., A. Bellizzi, V. Albarani, L. Guerra, M. Tommasino, A. Paradiso and V. Casavola (2000). "Phosphoinositide 3-kinase is involved in the tumor-specific activation of human breast cancer cell Na+/H+ exchange, motility, and invasion induced by serum deprivation." Journal of Biological Chemistry **275**(8): 5361-5369.

Rice, M. A. and K. S. Anseth (2007). "Controlling cartilaginous matrix evolution in hydrogels with degradation triggered by exogenous addition of an enzyme." Tissue Eng **13**(4): 683-691.

Ridley, A. J., M. A. Schwartz, K. Burridge, R. A. Firtel, M. H. Ginsberg, G. Borisy, J. T. Parsons and A. R. Horwitz (2003). "Cell migration: Integrating signals from front to back." Science **302**(5651): 1704-1709.

Riethdorf, S., H. Fritsche, V. Muller, T. Rau, C. Schindibeck, B. Rack, W. Janni, C. Coith, K. Beck, F. Janicke, S. Jackson, T. Gornet, M. Cristofanilli and K. Pantel (2007). "Detection of circulating tumor cells in peripheral blood of patients with metastatic breast cancer: A validation study of the CellSearch system." Clinical Cancer Research **13**(3): 920-928.

Runnels, L. W., L. X. Yue and D. E. Capham (2001). "TRP-PLIK, a bifunctional protein with kinase and ion channel activities." Science **291**(5506): 1043-1047.

Rybarczyk, P., M. Gautier, F. Hague, I. Dhennin-Duthille, D. Chatelain, J. Kerr-Conte, F. Pattou, J. M. Regimbeau, H. Sevestre and H. Ouadid-Ahidouch (2012). "Transient receptor potential melastatin-related 7 channel is overexpressed in human pancreatic ductal adenocarcinomas and regulates human pancreatic cancer cell migration." International Journal of Cancer **131**(6): E851-E861.

Sackmann, E. K., A. L. Fulton and D. J. Beebe (2014). "The present and future role of microfluidics in biomedical research." Nature **507**(7491): 181-189.

Saha, K., A. J. Keung, E. F. Irwin, Y. Li, L. Little, D. V. Schaffer and K. E. Healy (2008). "Substrate modulus directs neural stem cell behavior." Biophys J **95**(9): 4426-4438.

Sahai, E. and C. J. Marshall (2003). "Differing modes of tumour cell invasion have distinct requirements for Rho/ROCK signalling and extracellular proteolysis." Nature Cell Biology **5**(8): 711-719.

Salbreux, G., G. Charras and E. Paluch (2012). "Actin cortex mechanics and cellular morphogenesis." Trends Cell Biol **22**(10): 536-545.

Scherber, C., A. J. Aranyosi, B. Kulemann, S. P. Thayer, M. Toner, O. Iliopoulos and D. Irimia (2012). "Epithelial cell guidance by self-generated EGF gradients." Integrative Biology **4**(3): 259-269.

Schwab, A., A. Fabian, P. J. Hanley and C. Stock (2012). "Role of Ion Channels and Transporters in Cell Migration." Physiological Reviews **92**(4): 1865-1913.

Sciaccaluga, M., B. Fioretti, L. Catacuzzeno, F. Pagani, C. Bertollini, M. Rosito, M. Catalano, G. D'Alessandro, A. Santoro, G. Cantore, D. Ragozzino, E. Castigli, F. Franciolini and C. Limatola (2010). "CXCL12-induced glioblastoma cell migration requires intermediate conductance Ca2+-activated K+ channel activity." American Journal of Physiology-Cell Physiology **299**(1): C175-C184.

Seliktar, D. (2012). "Designing cell-compatible hydrogels for biomedical applications." Science **336**(6085): 1124-1128.

Shalem, O., N. E. Sanjana, E. Hartenian, X. Shi, D. A. Scott, T. S. Mikkelsen, D. Heckl, B. L. Ebert, D. E. Root, J. G. Doench and F. Zhang (2014). "Genome-Scale CRISPR-Cas9 Knockout Screening in Human Cells." Science **343**(6166): 84-87.

Sims, J. R., S. Karp and D. F. Ingber (1992). "Altering the Cellular Mechanical Force Balance Results in Integrated Changes in Cell, Cytoskeletal and Nuclear Shape." Journal of Cell Science **103**: 1215-1222.

Singh, A., S. Suri, T. Lee, J. M. Chilton, M. T. Cooke, W. Q. Chen, J. P. Fu, S. L. Stice, H. Lu, T. C. McDevitt and A. J. Garcia (2013). "Adhesion strength-based, label-free isolation of human pluripotent stem cells." Nature Methods **10**(5): 438-+.

Smith, J. P., T. B. Lannin, Y. A. Syed, S. M. Santana and B. J. Kirby (2014). "Parametric control of collision rates and capture rates in geometrically enhanced differential immunocapture (GEDI) microfluidic devices for rare cell capture." Biomedical Microdevices **16**(1): 143-151.

Song, Y. J., Y. Q. Zhang, P. E. Bernard, J. M. Reuben, N. T. Ueno, R. B. Arlinghaus, Y. L. Zu and L. D. Qin (2012). "Multiplexed volumetric bar-chart chip for point-of-care diagnostics." Nature Communications **3**.

Srivastava, J., G. Barreiro, S. Groscurth, A. R. Gingras, B. T. Goult, D. R. Critchley, M. J. S. Kelly, M. P. Jacobson and D. L. Barber (2008). "Structural model and functional significance of pH-dependent talin-actin binding for focal adhesion remodeling." Proceedings of the National Academy of Sciences of the United States of America **105**(38): 14436-14441.

Stock, C., M. Mueller, H. Kraehling, S. Mally, J. Noel, C. Eder and A. Schwab (2007). "PH nanoenvironment at the surface of single melanoma cells." Cellular Physiology and Biochemistry **20**(5): 679-686.

Stott, S. L., C. H. Hsu, D. I. Tsukrov, M. Yu, D. T. Miyamoto, B. A. Waltman, S. M. Rothenberg, A. M. Shah, M. E. Smas, G. K. Korir, F. P. Floyd, A. J. Gilman, J. B. Lord, D. Winokur, S. Springer, D. Irimia, S. Nagrath, L. V. Sequist, R. J. Lee, K. J. Isselbacher, S. Maheswaran, D. A. Haber and M. Toner (2010). "Isolation of circulating tumor cells using a microvortex-generating herringbone-chip." Proceedings of the National Academy of Sciences of the United States of America **107**(43): 18392-18397.

Stroka, K. M., H. Jiang, S. H. Chen, Z. Tong, D. Wirtz, S. X. Sun and K. Konstantopoulos (2014). "Water permeation drives tumor cell migration in confined microenvironments." Cell **157**(3): 611-623.

Sun, H. S., M. F. Jackson, L. J. Martin, K. Jansen, L. Teves, H. Cui, S. Kiyonaka, Y. Mori, M. Jones, J. P. Forder, T. E. Golde, B. A. Orser, J. F. MacDonald and M. Tymianski (2009). "Suppression of hippocampal TRPM7 protein prevents delayed neuronal death in brain ischemia." Nature Neuroscience **12**(10): 1300-U1124.

Sun, J. S., M. M. Li, C. Liu, Y. Zhang, D. B. Liu, W. W. Liu, G. Q. Hu and X. Y. Jiang (2012). "Double spiral microchannel for label-free tumor cell separation and enrichment." Lab on a Chip **12**(20): 3952-3960.

Svastova, E., W. Witarski, L. Csaderova, I. Kosik, L. Skvarkova, A. Hulikova, M. Zatovicova, M. Barathova, J. Kopacek, J. Pastorek and S. Pastorekova (2012). "Carbonic Anhydrase IX Interacts with Bicarbonate Transporters in Lamellipodia and Increases Cell Migration via Its Catalytic Domain." Journal of Biological Chemistry **287**(5): 3392-3402.

Swietach, P., J. B. Youm, N. Saegusa, C. H. Leem, K. W. Spitzer and R. D. Vaughan-Jones (2013). "Coupled Ca2+/H+ transport by cytoplasmic buffers regulates local Ca2+ and H+ ion signaling." Proceedings of the National Academy of Sciences of the United States of America **110**(22): E2064-E2073.

Thiery, J. P. and J. P. Sleeman (2006). "Complex networks orchestrate epithelial-mesenchymal transitions." Nature Reviews Molecular Cell Biology **7**(2): 131-142.

Tinevez, J. Y., U. Schulze, G. Salbreux, J. Roensch, J. F. Joanny and E. Paluch (2009). "Role of cortical tension in bleb growth." Proceedings of the National Academy of Sciences of the United States of America **106**(44): 18581-18586.

Tojkander, S., G. Gateva and P. Lappalainen (2012). "Actin stress fibers - assembly, dynamics and biological roles." Journal of Cell Science **125**(8): 1855-1864.

Tong, Z. Q., E. M. Balzer, M. R. Dallas, W. C. Hung, K. J. Stebe and K. Konstantopoulos (2012). "Chemotaxis of Cell Populations through Confined Spaces at Single-Cell Resolution." Plos One **7**(1).

Torisawa, Y. S., C. S. Spina, T. Mammoto, A. Mammoto, J. C. Weaver, T. Tat, J. J. Collins and D. E. Ingber (2014). "Bone marrow-on-a-chip replicates hematopoietic niche physiology in vitro." Nature Methods **11**(6): 663-+.

Tsai, F. C. and T. Meyer (2012). "Ca2+ Pulses Control Local Cycles of Lamellipodia Retraction and Adhesion along the Front of Migrating Cells." Current Biology **22**(9): 837-842.

Tse, J. R. and A. J. Engler (2011). "Stiffness gradients mimicking in vivo tissue variation regulate mesenchymal stem cell fate." PLoS One **6**(1): e15978.

Tung, C. K., L. Hu, A. G. Fiore, F. Ardon, D. G. Hickman, R. O. Gilbert, S. S. Suarez and M. M. Wu (2015). "Microgrooves and fluid flows provide preferential passageways for sperm over pathogen Tritrichomonas foetus." Proceedings of the National Academy of Sciences of the United States of America **112**(17): 5431-5436.

Turk, B. (2006). "Targeting proteases: successes, failures and future prospects." Nat Rev Drug Discov **5**(9): 785-799.

Ulrich, T. A., E. M. de Juan Pardo and S. Kumar (2009). "The mechanical rigidity of the extracellular matrix regulates the structure, motility, and proliferation of glioma cells." Cancer Res **69**(10): 4167-4174.

Verkman, A. S. (2005). "More than just water channels: unexpected cellular roles of aquaporins." Journal of Cell Science **118**(15): 3225-3232.

Wang, D. A., C. G. Williams, F. Yang, N. Cher, H. Lee and J. H. Elisseeff (2005). "Bioresponsive phosphoester hydrogels for bone tissue engineering." Tissue Eng **11**(1-2): 201-213.

Wang, P., F. Zhu and K. Konstantopoulos (2012). "The antagonistic actions of endogenous interleukin-1beta and 15-deoxy-Delta12,14-prostaglandin J2 regulate the temporal synthesis of matrix metalloproteinase-9 in sheared chondrocytes." J Biol Chem **287**(38): 31877-31893.

Wang, W. G., R. Eddy and J. Condeelis (2007). "The cofilin pathway in breast cancer invasion and metastasis." Nature Reviews Cancer **7**(6): 429-440.

Waning, J., J. Vriens, G. Owsianik, L. Stuwe, S. Mally, A. Fabian, C. Frippiat, B. Nilius and A. Schwab (2007). "A novel function of capsaicin-sensitive TRPV1 channels: involvement in cell migration." Cell Calcium **42**(1): 17-25.

Webb, D. J., D. H. D. Nguyen and S. L. Gonias (2000). "Extracellular signal-regulated kinase functions in the urokinase receptor-dependent pathway by which neutralization of low density lipoprotein receptor-related protein promotes fibrosarcoma cell migration and Matrigel invasion." Journal of Cell Science **113**(1): 123-134.

Wei, C., X. Wang, M. Chen, K. Ouyang, L. S. Song and H. Cheng (2009). "Calcium flickers steer cell migration." Nature **457**(7231): 901-905.

Wei, C. L., X. H. Wang, M. Chen, K. Ouyang, L. S. Song and H. P. Cheng (2009). "Calcium flickers steer cell migration." Nature **457**(7231): 901-905.

Weigelin, B., G. J. Bakker and P. Friedl (2012). "Intravital third harmonic generation microscopy of collective melanoma cell invasion: Principles of interface guidance and microvesicle dynamics." Intravital **1**(1): 32-43.

Wen, J. H., L. G. Vincent, A. Fuhrmann, Y. S. Choi, K. C. Hribar, H. Taylor-Weiner, S. Chen and A. J. Engler (2014). "Interplay of matrix stiffness and protein tethering in stem cell differentiation." Nat Mater **13**(10): 979-987.

Whitesides, G. M. (2006). "The origins and the future of microfluidics." Nature **442**(7101): 368-373.

Wirtz, D., K. Konstantopoulos and P. C. Searson (2011). "The physics of cancer: the role of physical interactions and mechanical forces in metastasis." Nat Rev Cancer **11**(7): 512-522.

Wolf, K., I. Mazo, H. Leung, K. Engelke, U. H. von Andrian, E. I. Deryugina, A. Y. Strongin, E. B. Brocker and P. Friedl (2003). "Compensation mechanism in tumor cell migration: mesenchymal-amoeboid transition after blocking of pericellular proteolysis." Journal of Cell Biology **160**(2): 267-277.

Wozniak, M. A., R. Desai, P. A. Solski, C. J. Der and P. J. Keely (2003). "ROCK-generated contractility regulates breast epithelial cell differentiation in response to the physical properties of a three-dimensional collagen matrix." J Cell Biol **163**(3): 583-595.

Wyckoff, J. B., S. E. Pinner, S. Gschmeissner, J. S. Condeelis and E. Sahai (2006). "ROCK- and myosin-dependent matrix deformation enables protease-independent tumor-cell invasion in vivo." Curr Biol **16**(15): 1515-1523.

Xu, T., P. Molnar, C. Gregory, M. Das, T. Boland and J. J. Hickman (2009). "Electrophysiological characterization of embryonic hippocampal neurons cultured in a 3D collagen hydrogel." Biomaterials **30**(26): 4377-4383.

Yamaguchi, H. and J. Condeelis (2007). "Regulation of the actin cytoskeleton in cancer cell migration and invasion." Biochim Biophys Acta **1773**(5): 642-652.

Yee, N. S., A. A. Kazi, Q. Li, Z. H. Yang, A. Berg and R. K. Yee (2015). "Aberrant over-expression of TRPM7 ion channels in pancreatic cancer: required for cancer cell invasion and implicated in tumor growth and metastasis." Biology Open **4**(4): 507-U107.

Yee, N. S., W. Q. Zhou and I. C. Liang (2011). "Transient receptor potential ion channel Trpm7 regulates exocrine pancreatic epithelial proliferation by Mg2+-sensitive Socs3a signaling in development and cancer." Disease Models & Mechanisms **4**(2): 240-U128.

Yeh, J., Y. Ling, J. M. Karp, J. Gantz, A. Chandawarkar, G. Eng, J. Blumling, 3rd, R. Langer and A. Khademhosseini (2006). "Micromolding of shape-controlled, harvestable cell-laden hydrogels." Biomaterials **27**(31): 5391-5398.

Yeo, Y., W. Geng, T. Ito, D. S. Kohane, J. A. Burdick and M. Radisic (2007). "Photocrosslinkable hydrogel for myocyte cell culture and injection." J Biomed Mater Res B Appl Biomater **81**(2): 312-322.

Yu, M., A. Bardia, B. Wittner, S. Stott, M. Smas, D. Ting, S. Isakoff, J. Cicillano, M. Wells, A. Shah, K. Concannon, M. Donaldson, L. Sequiet, E. Brachtel, D. Sgrol, J. Baseiga, S. Ramaswamy, M. Toner, D. Haber and S. Maheswaran (2013). "Circulating tumor cells in human breast cancer exhibit dynamic changes in epithelial and mesenchymal composition." Cancer Research **73**.

Zaman, M. H., L. M. Trapani, A. Siemeski, D. MacKellar, H. Gong, R. D. Kamm, A. Wells, D. A. Lauffenburger and P. Matsudaira (2006). "Migration of tumor cells

in 3D matrices is governed by matrix stiffness along with cell-matrix adhesion and proteolysis (vol 103, pg 10889, 2006)." Proceedings of the National Academy of Sciences of the United States of America **103**(37): 13897-13897.

Zhang, W. J., K. Kai, D. S. Choi, T. Iwamoto, Y. H. Nguyen, H. L. Wong, M. D. Landis, N. T. Ueno, J. Chang and L. D. Qin (2012). "Microfluidics separation reveals the stem-cell-like deformability of tumor-initiating cells." Proceedings of the National Academy of Sciences of the United States of America **109**(46): 18707-18712.

Zhang, Y. Q., W. J. Zhang and L. D. Qin (2014). "Mesenchymal-Mode Migration Assay and Antimetastatic Drug Screening with High-Throughput Microfluidic Channel Networks." Angewandte Chemie-International Edition **53**(9): 2344-2348.

Zhao, F., L. Li, L. Guan, H. Yang, C. Wu and Y. Liu (2014). "Roles for GP IIb/IIIa and alphavbeta3 integrins in MDA-MB-231 cell invasion and shear flow-induced cancer cell mechanotransduction." Cancer Lett **344**(1): 62-73.

Zheng, S. Y., H. K. Lin, B. Lu, A. Williams, R. Datar, R. J. Cote and Y. C. Tai (2011). "3D microfilter device for viable circulating tumor cell (CTC) enrichment from blood." Biomedical Microdevices **13**(1): 203-213.

CURRICULUM VITAE

Alexandros Afthinos

Johns Hopkins University
Department of Chemical and Biomolecular Engineering
Email: aafthin1@jhu.edu Phone: (410)336-3397

EDUCATION

Johns Hopkins University Baltimore, MD
Doctor of Philosophy in Chemical & Biomolecular Engineering September 2018

Johns Hopkins University Baltimore, MD
Bachelor of Science in Biomedical Engineering May 2011

HONORS/AWARDS

- Best Poster Presentation award at the 12th annual Nano-Symposium, Johns Hopkins University. **Awarded paper**: "Spatial regulation of RhoA dictates the migration mechanisms of dorsoventrally polarized cells in confinement" 2018
- Selected to consult the Training Subcommittee of the Johns Hopkins University Biomedical Scientific Workforce (consulted on challenges facing PhD students in biomedical fields; financing PhDs, grant acquisition, interpersonal relationships, coursework) 2017
- Graduated with honors 2011
- Selected by JHU BME department to present at the JHU BME Design Day 2011
- Student Activities Commission and Greek Life Leadership Award: "Greek Man of the Year 2009-2010" (excellence in leadership in academia, Greek life/fraternity, sports clubs, cultural clubs and in the broader Baltimore area) 2010
- Phi Delta Theta National Chapter honor in Community Service 2009
- Phi Delta Theta National General Head Quarters award 2009
- Member of the National Society of Collegiate Scholars 2008
- Honorary Mention in Biomedical Engineering Modeling and Design independent study 2007
- **Diploma** in classical piano (able to instruct beginner and intermediate level students) 2007

ACTIVITIES/LEADERSHIP

- **Lab administrator**, Konstantopoulos Lab, Johns Hopkins University Baltimore, MD (responsible for orders and lab finances, created a new system for bookkeeping, responsible for lab instrument technical support and purchasing of various instruments ranging from $1000-$400,000) 2012-2018

- **Lab mentor**, Konstantopoulos Lab, Chemical & Biomolecular Engineering, Johns Hopkins University — Baltimore, MD 2013-2018
  (Mentored high school students from the Baltimore Polytechnic Institute and Athens College, undergraduate, masters and PhD students from Hopkins, and oversaw research projects)

- **Teaching Assistant** for Transport Phenomena I, Johns Hopkins University — Baltimore, MD 2013-2014
  (responsible for holding class sections, lecturing when the professor was out of town, preparing homeworks, creating and grading midterms and final exams)

- Johns Hopkins University Table Tennis Club — Baltimore, MD
  President — 2008-2011

- Chesapeake Open Tournament at Johns Hopkins — Baltimore, MD
  (along with JOOLA USA created, organized and hosted a new annual table tennis open tournament in the East Cost the "Chesapeake Open" as part of the JOOLA North American Tour) — 2010

- Phi Delta Theta Maryland Delta Chapter (at Johns Hopkins University) — Baltimore, MD
  Founding Father, Executive Secretary (Fall 2009, Spring 2010) — 2009 - present

- Hellenic Students Association at Johns Hopkins University — Baltimore, MD
  President — 2010

- Johns Hopkins University Biomedical Engineering — Baltimore, MD
  Mentor in Biomedical Engineering — Fall 2009, Spring 2010

- "Hellenic Science Series" at Homewood campus — Baltimore, MD
  (created and organized a scientific lecture series) — 2010 - 2011

- The Bank of Greece summer camp — Athens, Greece
  Counselor — 2008

SHADOWING/ PHILANTHROPY/ VOLUNTEERING/ COMMUNITY SERVICE

- Shadowed Dr. Constantine G. Lyketsos at the Johns Hopkins Bayview Medical Center, Department of Psychiatry — Baltimore, MD 2011
  (Altzheimer's disease, dementia, depression)

- Shadowed Dr. Michael Marohn, Dr. Michael Schweitzer and Dr. Hien Nguyen in laparoscopic surgeries at the Johns Hopkins Bayview Medical Center — Baltimore, MD 2010

- Shadowed Dr. Jason Liau in brain surgeries and Intensive Care Unit rounds at the Johns Hopkins Hospital — Baltimore, MD 2010

- Participated in the Baltimore Rescue Mission Clinic (worked with Dr. John S. Dalton II to develop proper treatments for homeless people at the Baltimore East shelter) — Baltimore, MD 2009-2010

- Shadowed Dr. Fred Nucifora and Dr. Adam Rosenblatt at the Johns Hopkins Hospital Meyer 5 inpatient neuropsychiatry unit — Baltimore, MD 2009

- Volunteered at the Believe in Tomorrow Children's House at Johns Hopkins (interacted with parents and families of children that had been admitted at the Johns Hopkins Hospital for major surgeries, worked at the reception, gave tours to parents around the house, organized arts and crafts and other social events for families) — Baltimore, MD 2009

- Participated in American Cancer Society Relay for Life at Johns Hopkins — Baltimore, MD 2009, 2010

- Assisted in Amyotrophic Lateral Sclerosis Association awareness walk in Baltimore — Baltimore, MD 2009, 2010

- Organized Iron Phi 5K run for Amyotrophic Lateral Sclerosis awareness — Baltimore, MD 2010

- Organized and participated in "Save second base but don't forget the first" event for Amyotrophic Lateral Sclerosis and breast cancer awareness at Johns Hopkins — Baltimore, MD 2010

- Created an annual leadership tour event at Hopkins for middle school students from Baltimore Greektown and assisted the Greektown Community Development Corporation gain funds from The Abell Foundation — Baltimore, MD 2010 - 2011

- Supported the Alzheimer's Association of Greater Maryland in their annual gala fundraising event — Baltimore, MD 2010

RESEARCH/ DESIGN EXPERIENCE

- Department of Chemical & Biomolecular Engineering, Johns Hopkins University (Basic and Translational Science Research) — Baltimore, MD 2012-2018
  Ph.D. Candidate at the Konstantopoulos Lab
  (Research on breast cancer cell migration and cell motility. Invented a new in-vitro model for studying confined cell migration, with multiple other applications e.g. for the study of cell-cell interactions, cell-matrix interactions, collective migration, population dynamics, development of organs-on-a-chip. Studied breast cancer cell

migration in polydimethylsiloxane-based microfluidic devices and in 3D hydrogel-based environments, studied cell decision-making in confinement)

- Department of Plastic & Reconstructive Surgery, Baltimore, MD
  Johns Hopkins University (Clinical Research) 2011-2012
  Research Assistant at Dr. Andrew Lee's, Dr. Gerald Brandacher's Group
  (Vascularized Composite Allotransplantation lab)
  (Studies in rat peripheral nervous system regeneration using stem cells, programming of near-infrared laser for angiography—new method for imaging systemic monocytes, lymphatics and blood perfusion on random flaps)

- Department of Biomedical Engineering, Johns Hopkins University Baltimore, MD
  (Translational Research) 2008-2011
  Research Assistant at Dr. Jennifer H. Elisseeff's Research Group (JHE lab)
  (Studies in fat angiogenesis for post mastectomy applications, studies in novel hydrogel fillers for plastic surgery applications, studies in meniscus repair using hydrogels and microfibers, studies in cartilage regeneration using biomaterials and hydrogels for patients with osteoarthritis)

- JHU Biomedical Engineering Design Team 3 Baltimore, MD
  (built a portable heart rate monitor and in collaboration with 2010-2011
  Dr. Hien Nguyen designed, prototyped, marketed and licensed to
  LapSpace Medical a Laparoscopic Bowel Retractor)

- Laparoscopic Tissue Retractor (Provisional Patent) Baltimore, MD
  (Record of Invention #: C11529) 2011

- Orthopaedic Biomechanics Baltimore, MD
  (in cooperation with Dr. Ben Petre, designed and prototyped a 2009
  retrofitting exoskeleton that allows for one handed control of
  rotation, vacuum and irrigation of the arthroscope for orthopaedic surgeries)

ABSTRACTS — ORAL PRESENTATIONS

- Plastic Surgery Research Council: Ann Arbor, MI
  G.A. Brat, A. Afthinos, J. Christensen, K. Buretta, C. Gordon, D. Cooney, 2012
  W.P. Lee, G. Brandacher, J.M. Sacks. "Intensity and Time-Based Analysis for
  Prediction of Flap Necrosis Using Near-Infrared Angiography"

- Biomedical Engineering Society: Minneapolis, MN
  A. Afthinos, R. Zhao, A. Suppes, P. Mistriotis, K. Konstantopoulos. 2016
  "HEMICA-Hydrogel Encapsulated Micro-channel Array In Cancer Metastasis"

- Biomedical Engineering Society: Minneapolis, MN
  A. Afthinos, R. Zhao, K. Konstantopoulos. "The Role Of Cytoskeleton And 2016
  Ion Channels In Cell Decision-Making Under Confinement"

- American Institute of Chemical Engineers: San Francisco, CA
  A. Afthinos, R. Zhao, A. Suppes, P. Pachidis, K. Konstantopoulos. 2016
  "Hemica-Hydrogel Encapsulated Micro-channel Array In Cancer Metastasis"

- American Institute of Chemical Engineers: San Francisco, CA
  A. Afthinos, R. Zhao, K. Konstantopoulos. " The Role Of Cytoskeleton 2016
  And Ion Channels In Cell Decision-Making Under Confinement"

- Biomedical Engineering Society: Phoenix, AZ
  P. Mistriotis, E. Wisniewski, R. Law, A. Afthinos, S. Tuntithavornwat, 2017
  K. Bera, R. Zhao, K. Konstantopoulos. "Distinct Migration Mechanisms Of
  Vertically And Laterally Confined Cells"

- Biomedical Engineering Society: Phoenix, AZ
  R. Zhao, A. Afthinos, T. Zhu, K. Konstantopoulos. 2017
  "Blebbing And Protrusive Phenotypic Heterogeneity Of Aggressive Breast Cancer
  Cells Governs Their Patterns Of Decision Making"

- American Institute of Chemical Engineers: Austin, TX
  E. Wisniewski, P. Mistriotis, R. Law, A. Afthinos, S. Tuntithavornwat, 2017
  K. Bera, R. Zhao, K. Konstantopoulos. "The Mechanobiology Of Cancer Cell
  Motility Under Vertical And Lateral Confinement"

- Biomedical Engineering Society: Atlanta, GA
  P. Mistriotis, E. Wisniewski, R. Law, K. Bera, S. Tuntithavornwat, N. Perez, 2018
  A. Afthinos, R. Zhao, E. Erdogmus, C. Wain, S. X. Sun, P. Kalab, K. Konstantopoulos.
  "Feeling the Squeeze: How Motile Cells Respond to Different Types of Compression"

- American Institute of Chemical Engineers: Pittsburg, PA
  P. Mistriotis, E. Wisniewski, Y. Li, R. Law, K. Bera, S. Tuntithavornwat, 2018
  A. Afthinos, R. Zhao, S. X. Sun, P. Kalab, K. Konstantopoulos. "Perinuclear
  Actin Flow Promotes Efficient Cell Migration in Confinement"

- Biomedical Engineering Society: Atlanta, GA
  R. Zhao, A. Afthinos, K. Konstantopoulos. "Directional Cell Migration 2018
  Decision Making in 3D Confinement"

PUBLICATIONS

- A. T. Hillel, S. Unterman, Z. Nahas, B. Reid, J. M. Coburn, J. Axelman, J. J. Chae, Q. Guo, R. Trow, A. Thomas, Z. Hou, S. Lichtsteiner, D. Sutton, C. Matheson, P. Walker, N. David, S. Mori, J. M. Taube, J. H. Elisseeff, Photoactivated composite biomaterial for soft tissue restoration in rodents and in humans. Science Translational Medicine, (2011) — Acknowledgment

- S. Sengupta, A. Nagalingam, N. Muniraj, M.Y. Bonner, P. Mistriotis, A. Afthinos, P. Kuppusamy, D. Lanoue, S. Cho, P. Korangath, M. Shriver, A. Begum, V.F. Merino, C-Y. Juang, J.L. Arbiser, W. Matsui, B. Gyorffy, K. Konstantopoulos, S. Sukumar, P.A. Marignani, N.K. Saxena, D. Sharma, Activation of tumor suppressor LKB1 by honokiol abrogates cancer stem-like phenotype in breast cancer via inhibition of oncogenic Stat3. Oncogene, (2017)

- C. Pardo-Pastor, F. Rubio-Moscardo, M. Vaogel-Gonzalez, S. A. Serra, A. Afthinos, S. Mrkonjic, O. Destaing, J. F. Abenza, J. M. Fernandez-Fernandez, X. Trepat, C. Albiges-Rizo, K. Konstantopoulos, M. A. Valverde, Piezo2 channel regulates RhoA and actin cytoskeleton to promote cell mechanobiological responses. Proceedings of the National Academy of Sciences, (2018)

- P. Mistriotis, E. Winsewski, R. A. Law, K. Bera, Y. Li, S. Tuntithavornwat, N. Perez, A. Afthinos, R. Zhao, A. Surcel, E. S. Schiffhauer, D. G. Thomas, D. Robinson, P. Kalab, S. Sun, K. Konstantopoulos, Feeling the sueeze: How motile cells cope with different types of confinement. Nature Cell Biology, (2018) — Pending Submission

- A. Afthinos, A. Ozcelikkale, D. Maity, K. Bera, A. Suppes, P. Mistriotis, R. A. Law, Y. Chen, K. Konstantopoulos, HEMICA - Hydrogel Encapsulated Microchannel Array in Cancer Metastasis. Nature Biomedical Engineering (2018) — Pending Submission

- A. Afthinos*, R. Zhao*, T. Zhu, Y. Li, S. X. Sun, K. Konstantopoulos, Myosin IIA and TRPM7 channel sense hydraulic resistance and dictate decision-making. Nature Communications (2018) — Pending Submission (*equal first)

SKILLS

European Computer Driving License in Microsoft Office, iWorks, MATLAB, JAVA, SimBioSys software, BioPac software, FIJI, CatWalk, use of various mechanical instruments and drills, use of vacuum molding machines, experience in control circuits, oxygen-plasma treatment, flow cytometry, immunofluorescence, cell culture, microfabrication, etching, lift-off, electroplating, western blot, qPCR, cloning, lentivirus production, bacteria transformation, cell transfection, traction force microscopy, live-microscopy, confocal microscopy, good communication skills, diploma in synthesizer, diploma in piano, speak Greek, English and French, read ancient Greek.